Effective limits on single scalar extensions in the light of recent LHC data

Anisha,[1,5,*] Supratim Das Bakshi,[1,6,†] Shankha Banerjee,[2,‡] Anke Biekötter,[3,§] Joydeep Chakrabortty,[1,‖] Sunando Kumar Patra,[4,¶] and Michael Spannowsky[3,**]

[1]*Department of Physics, Indian Institute of Technology, Kanpur-208016, India*
[2]*CERN, Theoretical Physics Department, CH-1211 Geneva 23, Switzerland*
[3]*Institute for Particle Physics Phenomenology, Department of Physics, Durham University, Durham DH1 3LE, United Kingdom*
[4]*Department of Physics, Bangabasi Evening College, 19 Rajkumar Chakraborty Sarani, Kolkata 700009, West Bengal, India*
[5]*School of Physics & Astronomy, University of Glasgow, Glasgow G12 8QQ, United Kingdom*
[6]*CAFPE and Departamento de Física Teórica y del Cosmos, Universidad de Granada, Campus de Fuentenueva, E–18071 Granada, Spain*

(Received 26 July 2022; accepted 12 January 2023; published 21 March 2023)

In this paper, we work with 16 different single scalar particle extensions of the Standard Model. We present the sets of dimension-six effective operators and the associated Wilson coefficients as functions of model parameters after integrating out the heavy scalars up to one loop, including the heavy-light mixing, for each such scenario. Using the correspondence between the effective operators and the observables at the electroweak scale, and employing Bayesian statistics, we compute the allowed ranges of new physics parameters that are further translated and depicted in two-dimensional Wilson coefficient space in light of the latest CMS and ATLAS data up to 137 and 139 fb^{-1}, respectively. We also adjudge the status of those new physics extensions that offer similar sets of relevant effective operators. In addition, we provide a model-independent fit of 23 Standard Model effective field theory Wilson coefficients using electroweak precision observables, single- and di-Higgs data, as well as kinematic distributions of diboson production.

DOI: 10.1103/PhysRevD.107.055028

I. INTRODUCTION

Despite the successful journey of the Standard Model (SM) of particle physics, its inadequacy to explain many experimental observations and also the lack of direct evidence of new physics beyond the SM (BSM) in high-energy experiments compel us to look for indirect signatures of new physics (NP). Low-energy observables, such as the electroweak precision observables (EWPOs), the measurement of SM Higgs production and decay modes, as well as diboson production [1–78], play a crucial role in constraining the SM and leave little room for BSM physics. To understand the present status of NP under the lamp post of experimental data in terms of the non-SM parameters, we need to establish an effective connection between the BSM physics residing at a relatively high scale and observables at the electroweak scale. Effective field theories (EFTs) are considered to be elegant tools to extract indirect effects of NP from the experimental data, if any, by bridging the gap between scales.

In a bottom-up approach, the complete and independent set of effective operators for any given mass dimension is computed relying on the symmetry and particle content of the SM, leading to the most popular notion of the SM effective field theory (SMEFT) [29,31,79]. At dimension six, the commonly used bases of the SMEFT operators include the Warsaw basis[1] [29,31] and the strongly interacting light Higgs (SILH) basis [30,80]. Generally, the associated Wilson coefficients (WCs) are independent and not pertinent to any specific UV theory. Parametrizing low-energy observables in terms of these WCs and analyzing

*anisha@glasgow.ac.uk
†sdb@ugr.es
‡shankha.banerjee@cern.ch
§anke.biekoetter@durham.ac.uk
‖joydeep@iitk.ac.in
¶sunando.patra@gmail.com
**michael.spannowsky@durham.ac.uk

[1]The Warsaw basis accommodates a set of complete and nonredundant effective operators of mass dimension six.

them in global fits allows us to constrain potential NP in a (rather) model-independent way. Global analyses in the SMEFT framework have been performed for the EWPOs [81], Higgs [46,47,80,82–86], diboson [63,66,87–89], top sector [90–96], and combinations of these sectors [47,54,75,97–102]. In this work, we consider constraints from EWPOs, single- and di-Higgs data, as well as distributions from the diboson production channels.

In a top-down approach, the SMEFT lays the foundation to put different BSM scenarios on the same footing by integrating out heavy non-SM d.o.f. Each effective operator that emerges in the process is accompanied by a WC, which is a function of the model parameters and captures the footprints of NP interactions [103–119]. It is important to note that most of the phenomenologically interesting BSM scenarios do not induce the complete set of dimension-six SMEFT operators. In addition, the Wilson coefficients of effective operators computed by integrating out heavy d.o.f. from a specific NP Lagrangian are functions of model parameters and thus, unlike the model-independent SMEFT case, they are related to each other. As a result of these relations and the typically smaller number of free parameters, the SMEFT parameter space in a top-down analysis is usually much more stringently constrained compared to bottom-up analyses. Top-down SMEFT fits hence play a crucial role in pinning down the nature of BSM physics.

The primary motivation of this work is to estimate the allowed BSM parameter space for different SM extensions and perform a comparative analysis among those scenarios that are degenerate effective theories upon non-SM d.o.f. being integrated out. In our analysis, we consider 16 different single scalar extensions of the SM without extending the gauge symmetry. We embed each of the NP Lagrangians in our *Mathematica* program CoDEx [111] to perform the integration up to one loop, including the heavy-light mixing, and provide the exhaustive sets of the dimension-six effective operators in the Warsaw basis and their associated WCs as functions of model parameters.[2] The effective operators generated for these individual models can be verified using the complementary diagrammatic method introduced in Ref. [120]. We work within the Bayesian framework to draw the statistical inference and parameter estimation using the *Mathematica* package OptEx [121].

In this paper we constrain the SMEFT parameter space in both bottom-up as well as top-down approaches to provide an up-to-date map of the NP parameter space of scalar extensions of the SM. First, we perform a model-independent SMEFT fit based on the latest CMS and ATLAS data, including many distributions and simplified template cross sections. Second, we choose 16 different heavy scalars that are used frequently in the literature for different phenomenological reasons, e.g., neutrino mass generation, to explain IceCube or LHCb data, etc. [122–132]. For simplicity, we assume that the SM is extended by one single heavy scalar at a time. We compute the effective dimension-six operators and the associated WCs by performing the integration out of individual heavy fields up to one loop, including heavy-light mixing. These matching results incorporating scalar heavy-light mixing are presented in the Warsaw basis. We also provide the results in the SILH basis. The obtained results will be useful even when there are multiple heavy scalars. In that case, there will be additional contributions due to mutual interactions among the heavy fields. We further constrain the non-SM parameter space for each individual model using electroweak precision data and Higgs data. We highlight the impact of the individual data sets and their cumulative impact. This helps us to identify which data sets play a crucial role for which model while constraining the non-SM parameter space. We also pinpoint the directions in non-SM parameter space that cannot be constrained by our chosen set of data and comment on the observables necessary to constrain these models completely.

The paper is organized as follows. We provide details on the SMEFT parametrization of the used observables in Sec. II and describe the corresponding experimental inputs in Sec. III. In Sec. IV we perform a model-independent analysis including 23 WCs contributing to the EWPO, single Higgs, di-Higgs, and diboson sectors, and present the results for individual one-parameter fits as well as for a global analysis. In Sec. V we introduce the 16 single scalar extensions of the SM and reduce them to effective theories $\subset$ SMEFT. For each case, we tabulate the sets of emergent effective operators and associated WCs in the Warsaw basis as functions of the model parameters. We then employ similar fitting methodology for our two chosen NP models and display the results in terms of model parameters as well as in terms of the WCs. We discuss the renormalization group equations (RGEs) of the SMEFT operators for a specific model and capture its impact on the allowed BSM parameters and WCs in Sec. VI. We summarize our results and discuss possible future directions in Sec. VII. In Appendix B, we tabulate the computed effective operators and the WCs for the remaining 14 models adopted in this work. The workflow of this article is depicted in the flowchart shown in Fig. 1.

II. SMEFT PARAMETRIZATION

The SMEFT describes NP with higher-dimensional (in mass with dimension ≥ 5) operators consisting of only the SM fields and respecting the SM symmetries. The effective Lagrangian is given by

[2]We provide the sets of effective operators in both the Warsaw and SILH bases for all of these BSM scenarios in a *Mathematica* notebook file at https://github.com/effExTeam/Precision-Observables-and-Higgs-Signals-Effective-passageto-select-BSM.

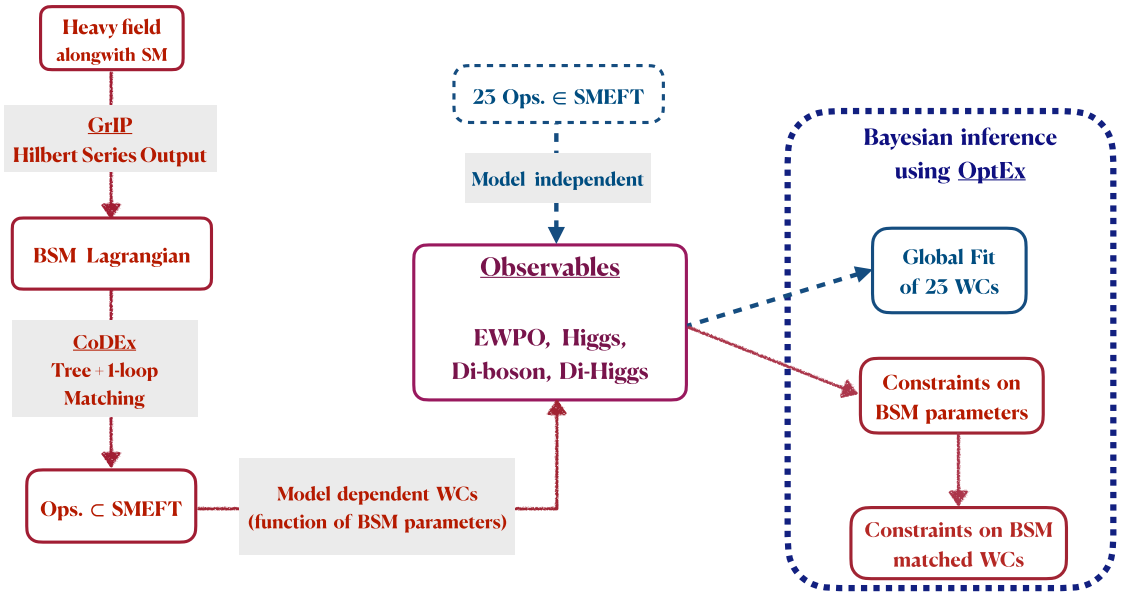

FIG. 1. Flowchart depicting the workflow of this article. Details on the observables are discussed in Sec. III. The global fit consists of 23 WCs; see Fig. 3. The constraints on the BSM parameters of specific models are discussed in Sec. V and Appendix B. We use the Hilbert series output from GrIP [133] to construct the BSM Lagrangian given the heavy field information. The BSM Lagrangians are then implemented in CoDEx [111] to compute the tree-level and one-loop-level WCs (including the heavy-light mixed WCs). We perform the statistical analysis based on Bayesian inference using the package OptEx [121].

$$\mathcal{L}_{\text{eff}} = \mathcal{L}_{\text{SM}}^{d\leq 4} + \mathcal{L}_{\text{SM}}^{\text{EFT}} = \mathcal{L}_{\text{SM}}^{d\leq 4} + \sum_{d=5,\ldots} \sum_{i} \left(\frac{\mathcal{C}_i^{(d)}}{\Lambda^{d-4}} \right) Q_i^{(d)}, \tag{2.1}$$

where $Q_i^{(d)}$ are the effective operators of mass dimension d and $\mathcal{C}_i^{(d)}$ are the accompanying WCs. The index i runs over the number of independent effective operators. At dimension six, there are 2499 independent operators in the most flavor-general case. This number reduces to 59 when assuming minimal flavor violation (MFV) [134] and real WCs. On the other hand, in a top-down approach the number of operators is determined by integrating out the heavy BSM fields. In this work, we confine ourselves to dimension-six operators in the Warsaw basis [31] and parametrize observables up to linear order in the WCs. The renormalizable part of the SM Lagrangian is given for the sake of completeness as

$$\begin{aligned}\mathcal{L}_{\text{SM}}^{d\leq 4} = & -\frac{1}{4} G^a_{\mu\nu} G^{a,\mu\nu} - \frac{1}{4} W^I_{\mu\nu} W^{I,\mu\nu} - \frac{1}{4} B_{\mu\nu} B^{\mu\nu} + |D_\mu H|^2 - \mu_H^2 |H|^2 - \frac{1}{2} \lambda_H^{\text{SM}} |H|^4 \\ & + \bar{l}_L i \not{D} l_L + \bar{q}_L i \not{D} q_L + \bar{e}_R i \not{D} e_R + \bar{u}_R i \not{D} u_R + \bar{d}_R i \not{D} d_R \\ & - \{ Y_e^{\text{SM}} H^\dagger \bar{e}_R l_L + Y_u^{\text{SM}} \tilde{H}^\dagger \bar{u}_R q_L + Y_d^{\text{SM}} H^\dagger \bar{d}_R q_L + \text{H.c.} \},\end{aligned} \tag{2.2}$$

where $B_{\mu\nu}$, $W^I_{\mu\nu}$, and $G^a_{\mu\nu}$ are the field-strength tensors of the SM gauge groups $U(1)_Y$, $SU(2)_L$, and $SU(3)_C$, respectively, with $a = 1, \ldots, 8$. The adopted conventions for the quantum numbers of the SM fields are shown in Table II. D denotes the covariant derivative, $Y^{\text{SM}}_{u,d,e}$ are the SM Yukawa couplings, and $\tilde{H} = i\sigma^2 H^*$ is the conjugate Higgs field.

Our SMEFT predictions are computed at linear order in the WCs in the electroweak $\{\alpha_{\text{EW}}, G_F, m_Z\}$ input scheme with the following input values:

$$\begin{aligned} \alpha_{\text{EW}}^{-1} &= 127.95, \qquad G_F = 1.6638 \times 10^{-5}\ \text{GeV}^{-2}, \\ m_Z &= 91.1876\ \text{GeV}, \qquad m_H = 125.09\ \text{GeV}, \\ m_t &= 173.2\ \text{GeV}. \end{aligned} \tag{2.3}$$

We generally assume MFV. However, for the dimension-six operators contributing to the Yukawa couplings, we distinguish between flavors and introduce different WCs for muons ($\mathcal{C}_{\mu H}$) and tau leptons ($\mathcal{C}_{\tau H}$), as well as the charm ($\mathcal{C}_{cH}$) and top quarks ($\mathcal{C}_{tH}$). There is of course no direct

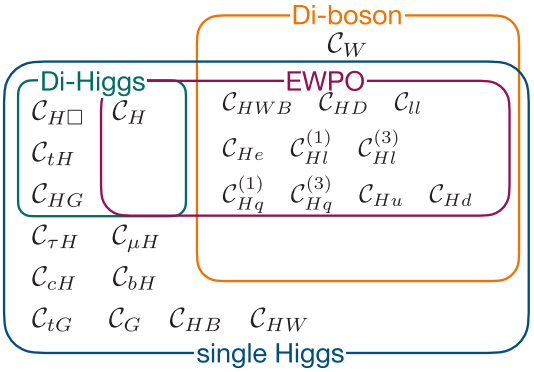

FIG. 2. Graphical summary of the considered Wilson coefficients in our model-independent analysis and the observables they contribute to.

measurement of the charm Yukawa coupling apart from the $h \to J/\psi\gamma$ searches [135] and in our analysis $\mathcal{C}_{cH}$ can be considered as a proxy for a modification of the total Higgs decay width, which can be constrained from a global fit of all Higgs signal strengths. It is important to note that with more data we will be able to explore the structure of the SMEFT operators which may not always follow MFV. The authors of Refs. [136,137] studied various such cases where the requirement for MFV is relaxed.

In total, we include 23 WCs in our model-independent analysis. A graphical summary of the WCs and the observables that they contribute to is given in Fig. 2. The corresponding operators are listed in Table XXVII in Appendix E.

A. Higgs signal strengths and simplified template cross sections

For the Higgs sector, most of the theory predictions are generated at leading order (LO) using the SMEFTsim model [138] in MadGraph 2.7.3 [139] with the default NNPDF23_NLO parton distribution functions [140]. Where available, SMEFT predictions are taken directly from fitmaker [75], which uses the same tools and settings as outlined above.

For the gluon-fusion simplified template cross section (STXS) categories, we instead use the predictions from the ATLAS combination in Ref. [10] which include matching, merging, and parton showering. LO predictions for the operator Q_G, which are not present in the ATLAS reference, are added using the SMEFT@NLO model [141]. For all other channels, we cannot use the ATLAS predictions due to different input parameter scheme choices and instead rely on the predictions at parton level generated with MadGraph. Overall, we describe our Higgs data sets in terms of the following WCs:

$$\begin{aligned}&\mathcal{C}_{H\Box}, \quad \mathcal{C}_{HW}, \quad \mathcal{C}_{HB}, \quad \mathcal{C}_{HG}, \quad \mathcal{C}_{tH}, \quad \mathcal{C}_{cH}, \quad \mathcal{C}_{bH}, \quad \mathcal{C}_{\tau H}, \quad \mathcal{C}_{\mu H}, \quad \mathcal{C}_G, \quad \mathcal{C}_{tG},\\ &\mathcal{C}_H, \quad \mathcal{C}_{HWB}, \quad \mathcal{C}_{HD}, \quad \mathcal{C}_{ll}, \quad \mathcal{C}_{Hl}^{(1)}, \quad \mathcal{C}_{Hl}^{(3)}, \quad \mathcal{C}_{He}, \quad \mathcal{C}_{Hq}^{(1)}, \quad \mathcal{C}_{Hq}^{(3)}, \quad \mathcal{C}_{Hd}, \quad \mathcal{C}_{Hu}.\end{aligned} \tag{2.4}$$

Currently, we only include $\mathcal{C}_H$ in the predictions of total Higgs signal strength measurements and not for STXS measurements. The corresponding contributions of Q_H to the predictions of different Higgs production and decay channels are taken from Refs. [142,143]. Notice that four-quark operators, which could contribute, for instance, to the $t\bar{t}h$ and th categories, are not included in our study at the moment. The inclusion of four-quark operators in global fits with top data has, however, not lead to a weakening of constraints on operators relevant for the top-Higgs sector such as $\mathcal{C}_{tH}$, $\mathcal{C}_G$, and $\mathcal{C}_{HG}$ [75,102]. We therefore assume that our approach does not overestimate the constraints on these operators.

B. Di-Higgs production cross section

The SMEFT predictions for the di-Higgs production cross section are generated using the ggHH model [144] within the POWHEG-BOX-V2 [145–147] framework which implements BSM effects in a nonlinear EFT framework including full NLO QCD corrections with massive top quarks. The Warsaw basis WCs $\mathcal{C}_i$ are related to the five anomalous couplings c_j in the ggHH model via

$$\begin{aligned}c_t &= 1 + \frac{v^2}{\Lambda^2}\mathcal{C}_{H\Box} - \frac{v^2}{\Lambda^2 y_t}\mathcal{C}_{tH},\\ c_{tt} &= \frac{v^2}{\Lambda^2}\left(\frac{1}{2}\mathcal{C}_{H\Box} - \frac{3}{4y_t}\mathcal{C}_{tH}\right),\\ c_{hhh} &= 1 + 3\frac{v^2}{\Lambda^2}\mathcal{C}_{H\Box} - \frac{v^2}{\lambda\Lambda^2}\mathcal{C}_H,\\ c_{ggh} &= 2c_{gghh} = (16\pi)^2\frac{2v^2}{\Lambda^2 g_s^2}\mathcal{C}_{HG},\end{aligned} \tag{2.5}$$

where we use Ref. [148] to translate from the SILH to the Warsaw basis. The effect of the operator Q_{tG} on the di-Higgs cross section is not taken into account. The di-Higgs cross section is thus parametrized in terms of the operators

$$\mathcal{C}_H, \quad \mathcal{C}_{H\Box}, \quad \mathcal{C}_{tH}, \quad \mathcal{C}_{HG}. \tag{2.6}$$

C. Di-boson distributions

We include distributions of WZ and WW production. As shown in Ref. [88], the k factors for the SM and the SMEFT interference in diboson distributions can be very different. The SMEFT predictions for these channels are generated

using the WZanomal and WWanomal models [88] within POWHEG-BOX-V2 which includes NLO QCD corrections [89,149,150]. We shower and hadronize our results using Pythia 8.2 [151].

For the WZ production with leptonic decays, we include the ATLAS m_T^{WZ} production distribution [152]. For the last bin of this distribution, which is an overflow bin, we cut off the SMEFT prediction at $m_T^{WZ} = 1$ TeV to ensure the validity of the EFT. We implement the cuts provided in Ref. [152] in Rivet [153] and validate the analysis by comparing our POWHEG + Pythia 8.2 SM predictions to those in the experimental reference. The SM predictions agree within 5% in each bin.

For WW production in the $e^{\pm}\nu\mu^{\mp}\nu$ final state, we include the leading lepton's p_T distribution, $p_T^{\ell_1}$, from the ATLAS study [22]. In order to consider the most sensitive bins, we take the predictions of bins 8 to 14. Similar to the WZ analysis, we utilize the cuts from the ATLAS study [22] in Rivet [153] and validate our POWHEG + Pythia 8.2 SM predictions to those in the experimental paper. The SM predictions agree within 6%.

The SMEFT predictions for the ATLAS $\Delta\phi_{jj}$ distribution in the electroweak Zjj production [21] are taken directly from fitmaker. This distribution tightly constrains anomalous triple gauge couplings induced by the operator Q_W, which is generated in several of the considered SM extensions.

For LEP WW data, we use the SM and SMEFT parametrizations as well as the theoretical uncertainties from Ref. [2] for the total and differential angular cross sections at different energies.

The diboson predictions are expressed in terms of the WCs

$$\begin{aligned} &\mathcal{C}_W, \quad \mathcal{C}_{HWB}, \quad \mathcal{C}_{HD}, \quad \mathcal{C}_{Hl}^{(1)}, \quad \mathcal{C}_{ll}, \quad \mathcal{C}_{Hl}^{(3)}, \quad \mathcal{C}_{He}, \\ &\mathcal{C}_{Hq}^{(1)}, \quad \mathcal{C}_{Hq}^{(3)}, \quad \mathcal{C}_{Hd}, \quad \mathcal{C}_{Hu}. \end{aligned} \tag{2.7}$$

D. Electroweak precision observables

We calculate the SMEFT parametrizations of the EWPOs based on Refs. [59,154,155]; see also Appendix A2 of Ref. [100] for the explicit expressions and Tables 10.4 and 10.5 of Ref. [156] for the most accurate SM predictions. The EWPO predictions are calculated in terms of the WCs

$$\begin{aligned} &\mathcal{C}_{HWB}, \quad \mathcal{C}_{HD}, \quad \mathcal{C}_{ll}, \quad \mathcal{C}_{Hl}^{(1)}, \quad \mathcal{C}_{Hl}^{(3)}, \quad \mathcal{C}_{He}, \quad \mathcal{C}_{Hq}^{(1)}, \\ &\mathcal{C}_{Hq}^{(3)}, \quad \mathcal{C}_{Hd}, \quad \mathcal{C}_{Hu}, \quad \mathcal{C}_H, \end{aligned} \tag{2.8}$$

where the contribution of $\mathcal{C}_H$ is only included in the SMEFT parametrization of m_W from Ref. [157].

III. OBSERVABLES

Our fits include data from EWPOs, LEP-WW measurements, as well as LHC data for single-Higgs, di-Higgs, diboson, and electroweak Zjj production processes.

(1) We include a total of 15 EWPOs. They consist of pseudomeasurements on the Z resonance [1], as well as a combination of the W mass measurements at LEP [158], Tevatron [159], and ATLAS [160], the LEP and Tevatron combination of the decay width of the W boson [161], and the Tevatron $\sin^2\theta_{\text{eff}}$ measurement [162]:

$$\begin{aligned} &\Gamma_Z, \quad \sigma_{\text{had}}^0, \quad R_l^0, \quad A_l, \quad A_l(\text{SLD}), \quad A_{FB}^l, \\ &R_c^0, \quad A_c, \quad A_{FB}^c, \quad R_b^0, \quad A_b, \quad A_{FB}^{0,b}, \\ &m_W, \quad \Gamma_W, \quad \sin^2\theta_{\text{eff}}^l(\text{Tev}). \end{aligned} \tag{3.1}$$

(2) We include LHC single-Higgs data from ATLAS and CMS. For LHC Run I, we incorporate the combination of ATLAS and CMS results in Ref. [3]. For ATLAS Run II, we add the STXS results from Refs. [10,11] as well as the measurements of the signal strengths in the $h \to Z\gamma$, $h \to \mu\mu$, $h \to \tau\tau$, and $h \to b\bar{b}$ [vector-boson fusion (VBF) and $t\bar{t}h$ only] decay channels. For CMS Run II, we make use of the signal-strength measurements [12–15] as well as the STXS results [16–19]. For the STXS $h \to ZZ \to 4\ell$ analysis [19] we neglect the "qqH-3j" category due to its very large uncertainty. For the $h \to WW$ channel signal-strength measurement [13] we only include the "0-jet" category and assume that the signal contribution comes from gluon fusion only (we discard the 5% contribution from the other production modes). For the CMS $t\bar{t}h$ analysis [15] we select only the most sensitive three channels for which there is one single dominant decay mode. These are the following three final states: two same-sign (SS) leptons with no hadronic τ, τ_h, ensuing from $h \to WW^*$, two SS leptons and one τ_h from $h \to \tau\tau$, and one lepton and two τ_h also from $h \to \tau\tau$. Once CMS combines the signal regions and provides the signal strength for different decay channels separately, we will be able to incorporate these into our analysis.

(3) For di-Higgs production, the total cross section signal-strength measurements in the $4b$, $2b2\tau$, and $2b2\gamma$ decay channels are taken into account [23–28]. These measurements include 36.1 fb^{-1} of data for ATLAS and up to 137 fb^{-1} for CMS. We have translated the upper limits given in the experimental references into signal-strength measurements, as listed in Table XXVI in Appendix D.

(4) We include momentum-dependent diboson distributions as well as the $\Delta\phi_{jj}$ distribution for electroweak Zjj production [21]. For WZ production with

leptonic decays, we include the ATLAS m_T^{WZ} production distribution with 36.1 fb^{-1} [152]. For $WW \to e\mu\nu\nu$ production, we include the $p_T^{\ell_1}$ distribution of the leading lepton in ATLAS [22]. We only include bins 8–14 of the distributions since we observed some discrepancies between our SM prediction and the ATLAS SM prediction in the low-$p_T^{\ell_1}$ regime. We include the measurements and correlation matrices as provided by Hepdata [163].

For LEP WW data, we consider the cross-section measurements for the process $e^+e^- \to W^+W^+ \to l\nu l\nu/l\nu qq/qqqq$ at different center-of-mass energies and angular distributions from Tables 12–15 of Ref. [2]. The actual experimental measurements are from Refs. [158,164–166].

The full list of observables included in our fits is given in Table I. To highlight the constraining power of recent analyses and compare with previous work, we split our set of observables into two sets called "2020 data set" and "this analysis" in the following. The 2020 data set is used to compare and crosscheck with Ref. [75]. The set called "this analysis" contains updated versions of some experimental analyses as well as additional data. To avoid overlap of experimental analyses, some data used in the 2020 data set has been removed from the "this analysis" set; see Table I.

TABLE I. Observables included in the fit. The rightmost column specifies which observables were part of the 2020 data set used for comparison with previous work. The observables in green are exclusively used in the 2020 data set. They are not part of our full data set as they overlap with other observables.

Observables		Number of measurements	References	2020
Electroweak precision observables				
Γ_Z, σ^0_{had}, R^0_l, A_l, A_l(SLD), A^l_{FB}, $\sin^2\theta^l_{\rm eff}$(Tev), R^0_c, A_c, A^c_{FB}, R^0_b, A_b, A^b_{FB}, m_W, Γ_W		15	Table 1 of Ref. [167]	✓
			Correlations in Ref. [1]	✓
LEP-2 *WW data*		74	Tables 12–15 of Ref. [2]	✓
Higgs data				
7 and 8 TeV Run-I data	ATLAS and CMS combination	20	Table 8 of Ref. [3]	✓
	ATLAS and CMS combination $\mu(h \to \mu\mu)$		Table 13 of Ref. [3]	✓
	ATLAS $\mu(h \to Z\gamma)$	1	Fig. 1 of Ref. [4]	✓
13 TeV ATLAS Run-II data	$\mu(h \to Z\gamma)$ at 139 fb^{-1}	1	[5]	✓
	$\mu(h \to \mu\mu)$ at 139 fb^{-1}	1	[6]	✓
	$\mu(h \to \tau\tau)$ at 139 fb^{-1}	4	Fig. 14 of Ref. [7]	
	$\mu(h \to bb)$ in VBF and ttH at 139 fb^{-1}	$1+1$	[8,9]	
	STXS Higgs combination	25	Figs. 20 and 21 of Ref. [168]	✓
	STXS $h \to \gamma\gamma/ZZ/b\bar{b}$ at 139 fb^{-1}	42	Figs. 1 and 2 of Ref. [10]	
	STXS $h \to WW$ in ggF, VBF at 139 fb^{-1}	11	Figs. 12 and 14 of Ref. [11]	
13 TeV CMS Run-II data	CMS combination at up to 137 fb^{-1}	23	Table 4 of Ref. [12]	✓
	$\mu(h \to b\bar{b})$ in Vh at 35.9/41.5 fb^{-1}	2	Entries from Table 4 of Ref. [12]	
	$\mu(h \to WW)$ in ggF at 137 fb^{-1}	1	[13]	
	$\mu(h \to \mu\mu)$ at 137 fb^{-1}	4	Fig. 11 of Ref. [14]	
	$\mu(h \to \tau\tau/WW)$ in $t\bar{t}h$ at 137 fb^{-1}	3	Fig. 14 of Ref. [15]	
	STXS $h \to WW$ at 137 fb^{-1} in Vh	4	Table 9 of Ref. [16]	
	STXS $h \to \tau\tau$ at 137 fb^{-1}	11	Figs. 11 and 12 of Ref. [17]	
	STXS $h \to \gamma\gamma$ at 137 fb^{-1}	27	Table 13 and Fig. 21 of Ref. [18]	
	STXS $h \to ZZ$ at 137 fb^{-1}	18	Table 6 and Fig. 15 of Ref. [19]	
ATLAS WZ **13 TeV** m_T^{WZ} at 36.1 fb^{-1}		6 bins	Fig. 4(c) of Ref. [20]	✓
ATLAS Zjj **13 TeV** $\Delta\phi_{jj}$ at 139 fb^{-1}		12 bins	Fig. 7(d) of Ref. [21]	✓
ATLAS WW **13 TeV** $p_T^{\ell 1}$ at 36.1 fb^{-1}		7 bins	Bins 8–14 of Fig. 7(a) of Ref. [22]	✓
Di-Higgs signal strengths: ATLAS and CMS 13 TeV data $\mu^{b\bar{b}b\bar{b}}_{HH}$, $\mu^{b\bar{b}\tau\bar{\tau}}_{HH}$, $\mu^{b\bar{b}\gamma\gamma}_{HH}$		6	[23–28]	

IV. MODEL-INDEPENDENT SMEFT: BAYESIAN ANALYSIS

The statistical analysis in this work is performed within a Bayesian framework. The priors, used in this work for free parameters, follow uniform distributions with some definite ranges. For all numerical results, samples from the unnormalized posterior distributions are used, each of which are generated from a Markov chain Monte Carlo (MCMC) process. The MCMC algorithm followed here is Metropolis-Hastings [169] and all runs come from a single long Markov chain. We make sure that all obtained samples are independent and identically distributed and the chains converge to desired quantiles. This is ensured through diagnostic checks and sequential runs following the prescriptions of Raftery and Lewis [170]. Point estimates are almost always quoted in terms of medians and fixed quantiles around them. Though not used, we keep track of all corresponding frequentist maximum likelihood estimates, which both help us to track the fit quality and are a good choice for the start of the Markov chains. As for priors, we use uniform distributions with specific (conservative) ranges for the free fit parameters. As we use the SM theoretical predictions for all observables from several sources, there are no nuisance-type parameters (e.g., SM input parameters) in this analysis with "informative" priors. Appendix C 1 contains detailed information about the priors for the free parameters here, i.e., the dimension-six SMEFT WCs.

We start the discussion of our model-independent fits by showing the results of one-parameter fits of the WCs in the upper panel of Fig. 3; see also Table XXIV for numerical results. In the figure, we contrast the results including our full data set with a reduced set based on the one used in the most recent fitmaker analysis [75]. See Table I for the exact data-set definitions. Overall, the WCs constrained through the EWPOs typically receive much stronger individual

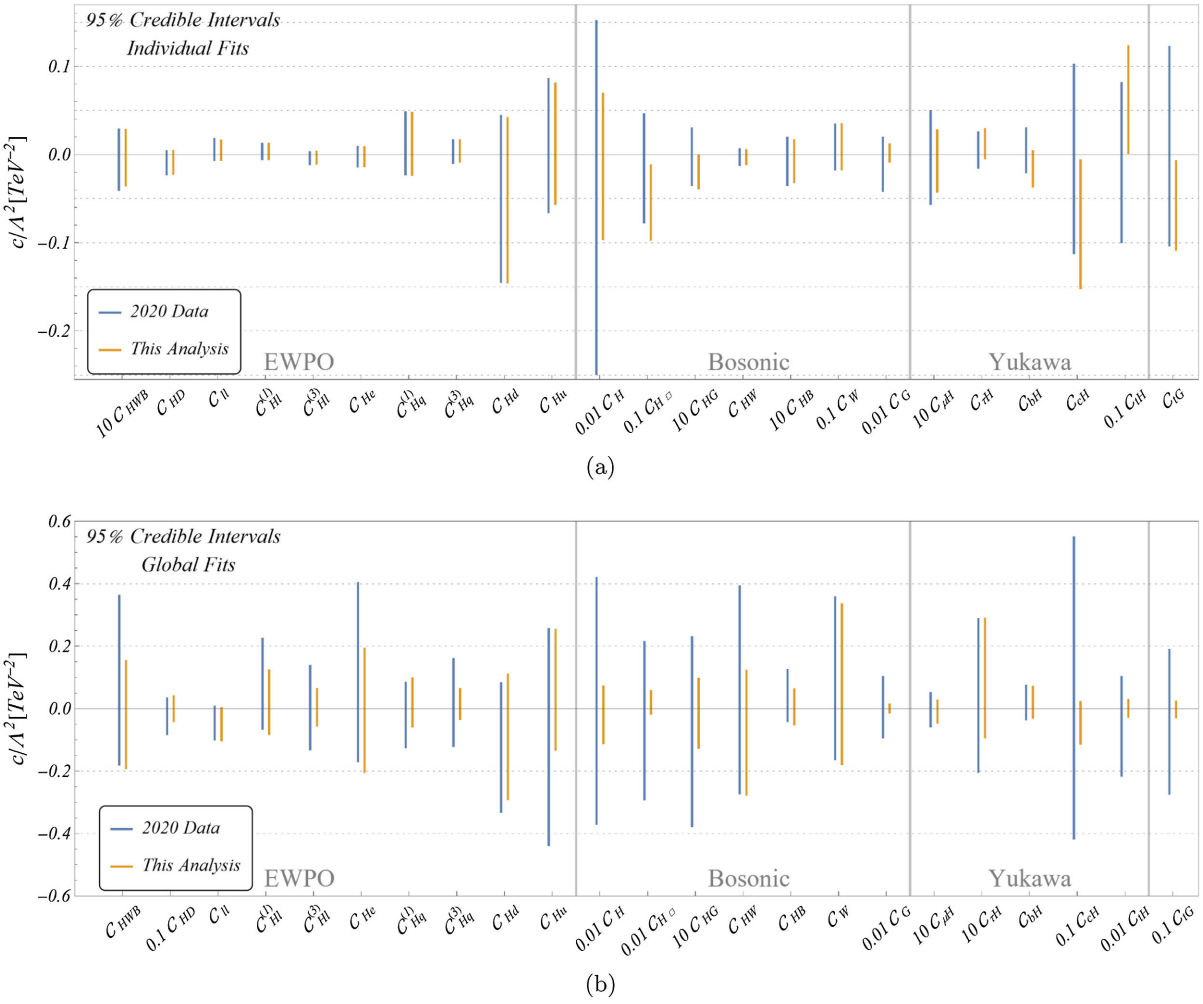

FIG. 3. Individual (top) and global (bottom) 95% credible intervals (CIs) limits on the WCs. We compare a fit involving our full data set (orange) with a reduced set containing LHC Higgs measurements up to 2020 (blue); see Table I for the data-set definitions. Note that some bounds have been scaled by factors of 10 to fit all results on the same y axis. The orange and blue lines appear in pairs in the sequence blue–orange for all the WCs.

bounds than those constrained through Higgs and diboson observables alone. The most weakly constrained WC is $\mathcal{C}_H$ which is most strongly constrained through di-Higgs production in our fit. Comparing the two fits, we find that operators constrained through EWPOs do not benefit from the addition of new data sets at the level of one-parameter fits. Several of the limits on the bosonic and Yukawa-like operators, on the other hand, are improved significantly. Deviations from the SM for some WCs, for instance, for $\mathcal{C}_{tH}$, are caused by large correlations in the CMS $h \to ZZ \to 4\ell$STXS analysis [19], specifically between the ggF 1jet ($p_T^H \in [0, 60]$ GeV), ggF 1jet ($p_T^H \in [60, 120]$ GeV),

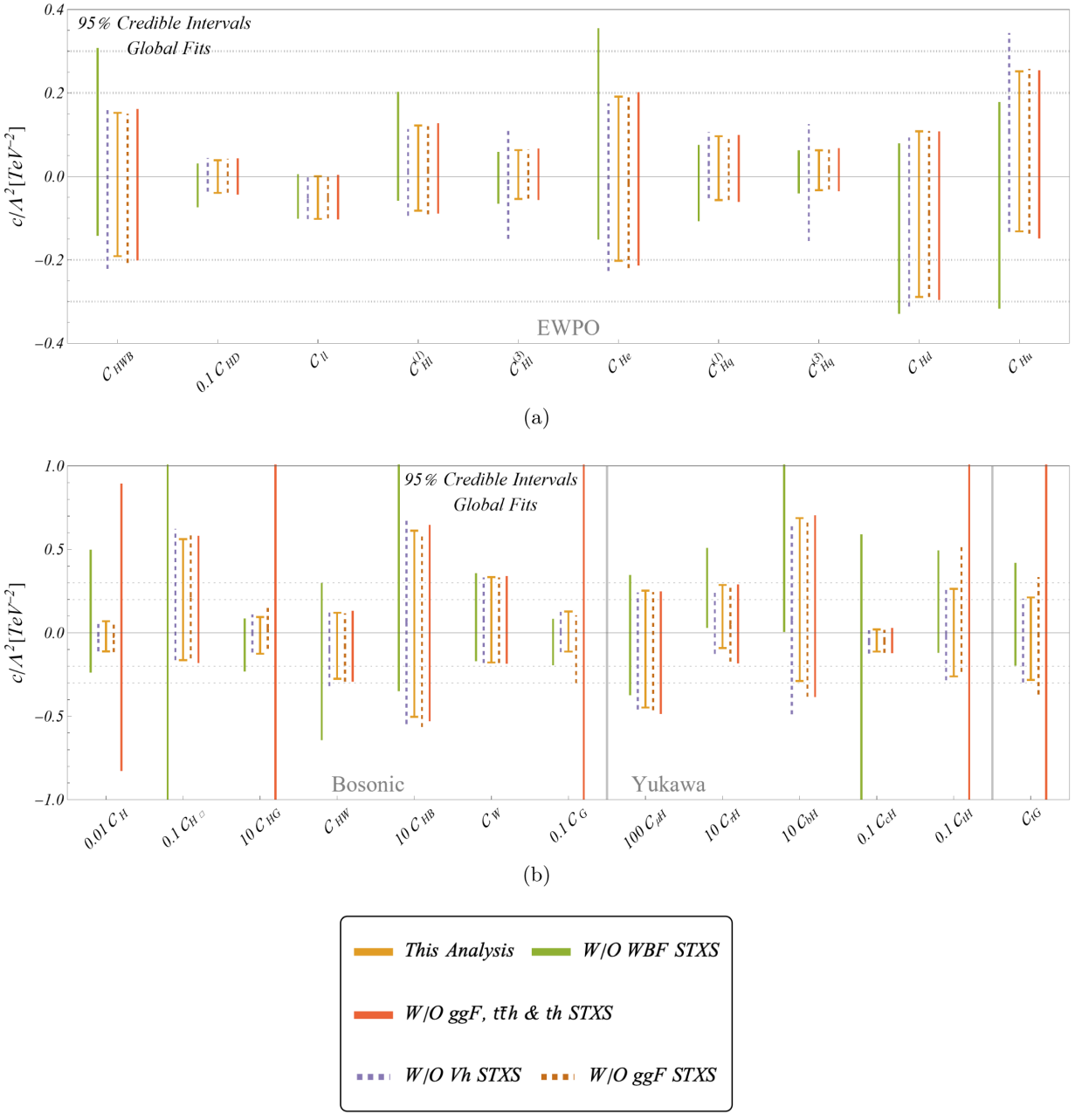

FIG. 4. Panels (a) and (b) show the 95% CI for 23 WCs in a global fit using different data sets. We contrast the corresponding intervals obtained using the full data set (orange) with data sets excluding certain sets of STXS measurements. We individually exclude STXS measurements of WBF production (green), Vh measurements (purple), ggF measurements (red dashed), and a combination of ggF with $t\bar{t}h$ and th (red solid). Note that some bounds have been scaled by factors of 10 to fit all results on the same y axis. The green, purple dashed, orange, red dashed, and red solid line constraints appear in the sequence green–purple(dashed)–orange–red(dashed)–red(solid) for all the WCs.

and qqH 2jet ($m_{jj} \in [0, 350]$ GeV, Vh veto) regions. However, in the global analysis with more d.o.f. none of these deviations persist.

In the lower panel of Fig. 3 we display the results of our global fit of 23 WCs after marginalization. Numerical results can be found in Table XXIV. To highlight the restriction power of recent STXS measurements, we again contrast our full data set with LHC data up to 2020. We have explicitly checked that the limits from this reduced data set are in good agreement with previous literature [75]. The improvements of the limits with the addition of more data is even more visible in the global fit than it was in the one-parameter fits. We find relatively mild improvement for WCs describing modified Higgs Yukawa couplings to leptons or bottom quarks. Many of the other limits, however, have significantly decreased.

Comparing the limits from one-parameter fits with the global analysis, we find that the limits of six WCs are weakened by a factor of 10 or more compared to the individual fit limits: $\mathcal{C}_{HWB}$, $\mathcal{C}_{HD}$, $\mathcal{C}_{HW}$, $\mathcal{C}_{HB}$, $\mathcal{C}_{He}$, $\mathcal{C}_{Hl}^{(1)}$. This is the result of the strong correlation of these coefficients as displayed in Table XXV. Many pairs of these WCs have absolute correlation coefficients of $\gtrsim 0.8$ as a result of their joint contribution to the shifts of SM parameters.

To gain a better understanding of the relevance of different Higgs production channels for the constraints on different WCs, in Fig. 4 we display the global fit limits on the WCs when certain STXS channels are removed from the analysis. In four additional fits, we remove the STXS channels for associated production of a Higgs with a vector boson (Vh), weak boson fusion (WBF), gluon fusion (ggF), and a combination of gluon fusion as well as top-associated production modes ($\mathrm{ggF} + t\bar{t}h + tH$). As expected, removing gluon-fusion STXS channels from the analysis only weakens the limits on $\mathcal{C}_{tG}$, $\mathcal{C}_{tH}$, $\mathcal{C}_G$, and $\mathcal{C}_{HG}$, highlighting the constraining power of ggF STXS measurements up to high transverse momenta of the Higgs. The highest-momentum STXS regions included in our analysis are $p_T^H \in [200, 300, 450]$ GeV and $p_T^H > 450$ GeV [18]. When in addition to removing the gluon-fusion STXS channels we also neglect top-associated Higgs production, the extreme weakening of the limits on $\mathcal{C}_{HG}$ and $\mathcal{C}_{tH}$ leads to looser constraints on $\mathcal{C}_H$. This is because of correlations of $\mathcal{C}_H$ with other WCs ($\mathcal{C}_{tH}$ and $\mathcal{C}_{HG}$) which are, however, irrelevant at the current level of constraints from ggF and top-associated Higgs production.

STXS measurements of Vh production mainly affect the limits of $\mathcal{C}_{Hq}^{(3)}$, $\mathcal{C}_{Hu}$, and $\mathcal{C}_{Hl}^{(3)}$. While $\mathcal{C}_{Hq}^{(3)}$ and $\mathcal{C}_{Hu}$ directly profit from Vh measurements at high p_T^V, $\mathcal{C}_{Hl}^{(3)}$ improves indirectly as it is highly correlated with $\mathcal{C}_{Hq}^{(3)}$. WBF STXS measurements influence several bosonic operators such as $\mathcal{C}_{H\Box}$ and $\mathcal{C}_{HWB}$. Other operators that do not directly contribute to WBF, for instance, $\mathcal{C}_{Hl}^{(1)}$ are affected by WBF STXS measurements through their correlation with other operators. $\mathcal{C}_{cH}$, which only appears in the parametrization of the Higgs width, is highly affected by WBF STXS data because of its correlation with $\mathcal{C}_{H\Box}$.

V. BSM SCENARIOS $\xrightarrow{\text{CoDEx}} \subset$ SMEFT: EFFECTIVE OPERATORS, WCs AND BAYESIAN ANALYSIS

In this work, we consider 16 different BSM scenarios that are extensions of the SM by single scalar representations. This choice is guided by our phenomenological interest and desire to encapsulate the features of various new physics interactions.[3] Color-singlet scalars with higher hypercharges are used to explain the origin of light neutrino masses through higher-dimensional operators. The colored leptoquark scalars are used to explain IceCube data, LHCb observations, etc. [122,127–132]. We chose BSM extensions that encapsulate the features of these heavy scalars which are frequently used in the literature. Even when the SM is extended by multiple heavy scalars, one can immediately determine which effective operators will emerge after integrating out those heavy fields. Of course, there will be additional contributions from the mutual interactions among the heavy fields. We start with the individual complete BSM Lagrangian and integrate out the heavy non-SM scalar multiplets using the automated *Mathematica*-based package CoDEx [111]. The BSM scenarios are then expressed in terms of the SM-renormalizable Lagrangian accompanied by the effective operators as given in Eq. (2.1).

We integrate out the heavy BSM fields up to one loop and tabulate the complete sets of emerging effective operators and accompanying WCs including the heavy-light mixing contribution from scalars in the loops. It is important to note that only those BSM scenarios generate heavy-light mixed WCs in which the heavy field couples to SM fields linearly [105,108,109,114,171].[4] This can be visualized by considering one-particle-irreducible one-loop diagrams where loop propagators are both heavy and light (SM) fields, but external legs are only light (SM) fields. We further suitably employ the equations of motion, Fierz identities, and integration by parts to ensure the emergence of the exhaustive lists of effective operators up to one loop.[5] The effective operators are depicted in the Warsaw basis [31]. The complete matching results can also be downloaded from our GitHub repository [172] where the reader will find the operators and the associated WCs in the SILH basis as well for all of these BSM scenarios. We require the

[3]The impact of the new physics parameters on renormalization of the SM parameters are ignored in our analysis.

[4]A detail discussion on the heavy-light effective action formulae is in Appendix A 2.

[5]In Ref. [114], the effective operators were tagged per their dominant emergence through tree (T), only heavy (HH), and heavy-light (HL) mixing.

TABLE II. SM and BSM fields and their spin and gauge quantum numbers. The BSM Lagrangians are constructed using these fields.

		SM quantum numbers		
SM field	Spin	$SU(3)_C$	$SU(2)_L$	$U(1)_Y$[a]
q_L	$\frac{1}{2}$	3	2	$\frac{1}{6}$
l_L	$\frac{1}{2}$	1	2	$-\frac{1}{2}$
u_R	$\frac{1}{2}$	3	1	$\frac{2}{3}$
d_R	$\frac{1}{2}$	3	1	$-\frac{1}{3}$
e_R	$\frac{1}{2}$	1	1	-1
H	0	1	2	$\frac{1}{2}$
$B_{\mu\nu}$	1	1	1	0
$W_{\mu\nu}$	1	1	3	0
$G_{\mu\nu}$	1	8	1	0

		SM quantum numbers			
BSM field	Spin	$SU(3)_C$	$SU(2)_L$	$U(1)_Y$	Mass
$\mathcal{S}$	0	1	1	0	$m_{\mathcal{S}}$
Δ	0	1	3	0	m_{Δ}
$\mathcal{S}_1$	0	1	1	1	$m_{\mathcal{S}_1}$
$\mathcal{S}_2$	0	1	1	2	$m_{\mathcal{S}_2}$
Δ_1	0	1	3	1	m_{Δ_1}
$\mathcal{H}_2$	0	1	2	$-\frac{1}{2}$	$m_{\mathcal{H}_2}$
Σ	0	1	4	$\frac{1}{2}$	m_{Σ}
φ_1	0	3	1	$-\frac{1}{3}$	m_{φ_1}
φ_2	0	3	1	$-\frac{4}{3}$	m_{φ_2}
Θ_1	0	3	2	$\frac{1}{6}$	m_{Θ_1}
Θ_2	0	3	2	$\frac{7}{6}$	m_{Θ_2}
Ω	0	3	3	$-\frac{1}{3}$	m_{Ω}
χ_1	0	6	3	$\frac{1}{3}$	m_{χ_1}
χ_2	0	6	1	$\frac{4}{3}$	m_{χ_2}
χ_3	0	6	1	$-\frac{2}{3}$	m_{χ_3}
χ_4	0	6	1	$\frac{1}{3}$	m_{χ_4}

[a]Hypercharge convention: $Q_{\rm em} = T_3 + \mathrm{Y}$, where $Q_{\rm em}$, T_3, and Y are the electromagnetic charge, third component of the isospin quantum number, and hypercharge, respectively.

Wilson coefficients of Warsaw basis effective operators in this analysis, because the observables are parametrized in terms of the SMEFT Warsaw basis operators to perform the global and model-specific fits. The complete SMEFT dimension-six matching results for some of the SM extensions are already available in the literature in the Warsaw basis, for example, for the real singlet scalar model [173–175] and scalar leptoquarks [176]. However, for the remaining models, to the best of our knowledge, the complete SMEFT dimension-six matching results in the Warsaw basis up to one loop including heavy-light mixing are not available yet. A tree-level matching dictionary [177], and partial results for some models including scalar heavy-light mixing (in the SILH basis) [103,106,108], are available as well.

In the following subsections, we tabulate the effective operators generated and the associated WCs in terms of the model parameters in the Warsaw basis for two representative cases: the two-Higgs-doublet model $\mathcal{H}_2$, and a scalar leptoquark Θ_1. These models encapsulate the individual features of a color singlet and a nonsinglet heavy field, respectively. The two models share the exact same set of relevant[6] effective operators apart from the additional emergence of $Q_{\rm HG}$ in the latter model; see Table IV. We tabulate the results for the rest of the adopted scenarios in Appendix B.

Here, we provide the operators at the scale where they emerge, i.e., the cutoff scale (Λ) which we take equal to the mass of heavy BSM fields (m_{hf}), in all cases that we discuss. We further assume that the mass of the heavy field $m_{hf} \gg$ the electroweak-symmetry-breaking scale. Thus, the heavy fields can be integrated out safely, validating the notion of EFT, and all of the dimension-six operators are suppressed by $1/m_{hf}^2$. Here, to start with we ignore the running of the effective operators and perform the analysis. Later, in Sec. VI, for the extra electroweak doublet scalar (EWDS) scenario, we discuss how the inclusion of the running of effective operators impacts the parameter space.

In the model-independent analysis in Sec. IV, we introduce an explicit flavor dependence for the operators of the $\psi^2\phi^3$ class with the corresponding WCs $\mathcal{Q}_{\mu H}$, $\mathcal{Q}_{\tau H}$, $\mathcal{Q}_{cH}$, $\mathcal{Q}_{bH}$, and $\mathcal{Q}_{tH}$. As we are using CoDEx results for the model-dependent part of the analysis and CoDEx does not differentiate between flavors (yet), $\mathcal{C}_{\mu H}$ and $\mathcal{C}_{cH}$ are set to be zero for the rest of the analysis and we work with operators consisting of third-generation fermions only. For the rest of the paper, the associated WCs will be denoted as $\mathcal{C}_{uH}$, $\mathcal{C}_{dH}$, and $\mathcal{C}_{eH}$. In the later subsections, we highlight the operators (in red) that do not affect our chosen set of observables and thus are absent from our analysis. The blue operators are functions of SM parameters only and thus are independent of our fit parameters. Each of the observables can be thought of as a set of effective operators which has been useful to classify different single scalar field extensions of the SM [114]. Relying on that concept, we design the methodology of our analysis to pin down the individual and mutual statuses of these BSM scenarios in this section.

In Sec. IV we obtain the constraints on the set of 23 SMEFT WCs in a model-independent manner, using the observables listed in Sec. III. In this section, we move a step ahead and connect the relevant observables expressed in terms of the SMEFT dimension-six operators and their respective WCs to the BSM model parameters. The SMEFT matching results obtained for a particular BSM scenario (mentioned above) allow us to write the WCs in terms of the respective model parameters and m_{hf}.

[6]In our analysis, the operators that are present in our chosen set of observables and are functions of BSM parameters are relevant. In the results section, we focus primarily on these operators.

Consequently, the bounds on the model parameters of specific BSM scenarios are obtained directly from the relevant experimental data.

The methodology of the statistical analysis is similar to the one discussed in the model-independent part. Fits are performed over the relevant BSM parameters while considering the best-fit values for the SM ones; see Eq. (2.3). Uniform priors within the range $\{-50, 50\}$ are chosen for these non-SM parameters and m_{hf} is chosen to be 1 TeV uniformly in this analysis. The following subsections showcase two example scenarios where the SM is extended by two scalars, $\mathcal{H}_2$ and Θ_1, based on the relations among the associated WCs of the emergent effective operators through the model parameters for individual cases.

A. Extra EW doublet scalar: $\mathcal{H}_2 \equiv (\mathbf{1}_C, \mathbf{2}_L, -\frac{1}{2}|_Y)$

This model contains an extra isospin-doublet scalar $(\mathcal{H}_2)$ which is a color singlet with hypercharge $Y = -\frac{1}{2}$. The BSM Lagrangian is given as [103,123,178–181]

$$\begin{aligned}\mathcal{L}_{\mathcal{H}_2} = \mathcal{L}_{\rm SM}^{d\leq 4} &+ |\mathcal{D}_\mu \mathcal{H}_2|^2 - m_{\mathcal{H}_2}^2 |\mathcal{H}_2|^2 - \frac{\lambda_{\mathcal{H}_2}}{4}|\mathcal{H}_2|^4 - (\eta_H |\tilde{H}|^2 + \eta_{\mathcal{H}_2}|\mathcal{H}_2|^2)(\tilde{H}^\dagger \mathcal{H}_2 + \mathcal{H}_2^\dagger \tilde{H}) \\ &- \lambda_{\mathcal{H}_2,1}|\tilde{H}|^2|\mathcal{H}_2|^2 - \lambda_{\mathcal{H}_2,2}|\tilde{H}^\dagger \mathcal{H}_2|^2 - \lambda_{\mathcal{H}_2,3}[(\tilde{H}^\dagger \mathcal{H}_2)^2 + (\mathcal{H}_2^\dagger \tilde{H})^2] \\ &- \{Y_{\mathcal{H}_2}^{(e)} \bar{l}_L \tilde{\mathcal{H}}_2 e_R + Y_{\mathcal{H}_2}^{(u)} \bar{q}_L \mathcal{H}_2 u_R + Y_{\mathcal{H}_2}^{(d)} \bar{q}_L \tilde{\mathcal{H}}_2 d_R + \text{H.c.}\}. \end{aligned} \tag{5.1}$$

Here, $m_{\mathcal{H}_2}$ is the mass of the heavy field and serves as the cutoff scale. We assume that the heavy Higgs doublet is decoupled to the SM one, and they do not mix [181]. This model contains nine BSM parameters (η_H, $\eta_{\mathcal{H}_2}$, $\lambda_{\mathcal{H}_2}$, $\lambda_{\mathcal{H}_2,1}$, $\lambda_{\mathcal{H}_2,2}$, $\lambda_{\mathcal{H}_2,3}$, $Y_{\mathcal{H}_2}^{(u)}$, $Y_{\mathcal{H}_2}^{(d)}$, $Y_{\mathcal{H}_2}^{(e)}$) and the WCs are functions of all of these parameters along with the SM ones; see Table III. We assume that the BSM Yukawas couple only to the third generation of fermions. In the decoupling limit, these Yukawas do not mix with the SM ones [181]. We further note that the WCs of the relevant operators $Q_{\rm uH}$, $Q_{\rm dH}$, $Q_{\rm eH}$, $Q_{\rm H}$, $Q_{\rm HW}$, $Q_{\rm HB}$, $Q_{\rm HWB}$, $Q_{\rm H\Box}$, and Q_{HD} contain all of the BSM parameters. In our numerical analysis, we choose to work with a Z_2-invariant ($H \to H$ and $\mathcal{H}_2 \to -\mathcal{H}_2$) BSM Lagrangian. Thus, the quartic couplings η_H, $\eta_{\mathcal{H}_2}$ and the Yukawa couplings $Y_{\mathcal{H}_2}^{(u)}$, $Y_{\mathcal{H}_2}^{(d)}$, $Y_{\mathcal{H}_2}^{(e)}$ do not appear in our analysis, where the rest of the three parameters get constrained by our chosen experimental data set. Note that, although $\lambda_{\mathcal{H}_2}$ corresponds to a Z_2-invariant term, it still cannot be constrained as it always appears in the WCs with the Z_2-violating couplings. Thus, to constrain these *unconstrained* couplings of the EWDS model, one needs to look for observables beyond the chosen ones in this work that get corrections from the following operators: $Q_{\rm le}$, $Q_{\rm qd}{}^{(1)}$, $Q_{\rm qu}{}^{(1)}$, $Q_{\rm qu}{}^{(1)}$, $Q_{\rm quqd}{}^{(1)}$, $Q_{\rm lequ}{}^{(1)}$, $Q_{\rm ledq}$ (see Table III). These additional observables will be helpful to constrain $\lambda_{\mathcal{H}_2}$ even for the Z_2-symmetric Lagrangian. We need to keep in mind that the choice of the new set of observables is guided by the structures of the unconstrained WCs of this particular model only.

1. Constraints on the model parameters

Using the relations listed in Table III, we obtain the constraints on the BSM parameters directly from the experimental data. The relevant BSM fit parameters for this model are $\lambda_{\mathcal{H}_2,1}$, $\lambda_{\mathcal{H}_2,2}$, and $\lambda_{\mathcal{H}_2,3}$ with the mass of the heavy doublet, m_{hf} (cutoff scale), set to 1 TeV. The list of the dimension-six operators colored in black and blue in Table III are replaced by the corresponding WCs in the SMEFT parametrization of the observables. The WCs for the operators in blue are functions of only SM parameters ([inputs given in Eq. (2.3)]. Those for operators in black are functions of the relevant BSM parameters and are thus relevant in constraining them. Uniform distributions within the range $\{-50, 50\}$ are chosen as priors for these BSM couplings.

Using the samples from the un-normalized posteriors, we show the correlations between various BSM parameters in Fig. 5 as high-probability contours of two-dimensional marginal posteriors. Constant-probability contours enclose the 68% (black solid, red/blue dashed) and 95% (black dot-dashed, red/blue dotted) credible regions, respectively. We also show colored regions with variable-density contour shading (black/red/blue) pointing to regions of high probability. These regions are significant to adjudge the different high-probability regions in the allowed parameter space. This is evident from the posteriors obtained from the "All" measurements fit, which contain more than one high-probability region. For instance, in Fig. 5(a) there are four different high-probability regions within the 68% credible region enclosed by the solid black constant-probability contour.

In order to demonstrate the constraining power of different data sets, in Figs. 5(a)–5(c) we show the posterior distributions of these three parameters obtained from the "All" (black), "Higgs" (red), and "EWPO" (blue) sets of experimental measurements. While the constraints from Higgs data are overall a bit stronger, EWPO data add orthogonal information, leading to significantly tightened bounds when combining the data from both sectors. In Fig. 5(a), the bound on $\lambda_{\mathcal{H}_2,1}$ from EWPOs only is very

TABLE III. Warsaw basis effective operators and the associated WCs that emerge after integrating out the heavy field $\mathcal{H}_2$: $(1,2,-\frac{1}{2})$. Operators highlighted in red do not affect our current set of observables and are thus absent from our analysis. Operators highlighted in blue are functions of SM parameters only, while the red ones do not contribute to our observables.

Dimension-six operators	Wilson coefficients
Q_{dH}	$\frac{\eta_H^2 Y_d^{SM}}{16\pi^2 m_{\mathcal{H}_2}^2} - \frac{3\eta_H\eta_{\mathcal{H}_2} Y_d^{SM}}{16\pi^2 m_{\mathcal{H}_2}^2} - \frac{\eta_H Y_{\mathcal{H}_2}^{(d)}}{m_{\mathcal{H}_2}^2} - \frac{3\eta_H\lambda_{\mathcal{H}_2} Y_{\mathcal{H}_2}^{(d)}}{32\pi^2 m_{\mathcal{H}_2}^2} + \frac{3\eta_H\lambda_{\mathcal{H}_2,1} Y_{\mathcal{H}_2}^{(d)}}{16\pi^2 m_{\mathcal{H}_2}^2} - \frac{3\eta_{\mathcal{H}_2}\lambda_{\mathcal{H}_2,1} Y_{\mathcal{H}_2}^{(d)}}{16\pi^2 m_{\mathcal{H}_2}^2} + \frac{\eta_H\lambda_{\mathcal{H}_2,2} Y_{\mathcal{H}_2}^{(d)}}{4\pi^2 m_{\mathcal{H}_2}^2} - \frac{3\eta_{\mathcal{H}_2}\lambda_{\mathcal{H}_2,2} Y_{\mathcal{H}_2}^{(d)}}{16\pi^2 m_{\mathcal{H}_2}^2} + \frac{\lambda_{\mathcal{H}_2,2}^2 Y_d^{SM}}{192\pi^2 m_{\mathcal{H}_2}^2} + \frac{5\eta_H\lambda_{\mathcal{H}_2,3} Y_{\mathcal{H}_2}^{(d)}}{8\pi^2 m_{\mathcal{H}_2}^2} + \frac{\lambda_{\mathcal{H}_2,3}^2 Y_d^{SM}}{48\pi^2 m_{\mathcal{H}_2}^2}$
Q_{eH}	$\frac{\eta_H^2 Y_e^{SM}}{16\pi^2 m_{\mathcal{H}_2}^2} - \frac{3\eta_H\eta_{\mathcal{H}_2} Y_e^{SM}}{16\pi^2 m_{\mathcal{H}_2}^2} - \frac{\eta_H Y_{\mathcal{H}_2}^{(e)}}{m_{\mathcal{H}_2}^2} - \frac{3\eta_H\lambda_{\mathcal{H}_2} Y_{\mathcal{H}_2}^{(e)}}{32\pi^2 m_{\mathcal{H}_2}^2} + \frac{3\eta_H\lambda_{\mathcal{H}_2,1} Y_{\mathcal{H}_2}^{(e)}}{16\pi^2 m_{\mathcal{H}_2}^2} - \frac{3\eta_{\mathcal{H}_2}\lambda_{\mathcal{H}_2,1} Y_{\mathcal{H}_2}^{(e)}}{16\pi^2 m_{\mathcal{H}_2}^2} + \frac{\eta_H\lambda_{\mathcal{H}_2,2} Y_{\mathcal{H}_2}^{(e)}}{4\pi^2 m_{\mathcal{H}_2}^2} - \frac{3\eta_{\mathcal{H}_2}\lambda_{\mathcal{H}_2,2} Y_{\mathcal{H}_2}^{(e)}}{16\pi^2 m_{\mathcal{H}_2}^2} + \frac{\lambda_{\mathcal{H}_2,2}^2 Y_e^{SM}}{192\pi^2 m_{\mathcal{H}_2}^2} + \frac{5\eta_H\lambda_{\mathcal{H}_2,3} Y_{\mathcal{H}_2}^{(e)}}{8\pi^2 m_{\mathcal{H}_2}^2} + \frac{\lambda_{\mathcal{H}_2,3}^2 Y_e^{SM}}{48\pi^2 m_{\mathcal{H}_2}^2}$
Q_{uH}	$\frac{\eta_H^2 Y_u^{SM}}{16\pi^2 m_{\mathcal{H}_2}^2} + \frac{3\eta_H\lambda_{\mathcal{H}_2} Y_{\mathcal{H}_2}^{(u)}}{32\pi^2 m_{\mathcal{H}_2}^2} + \frac{\eta_H Y_{\mathcal{H}_2}^{(u)}}{m_{\mathcal{H}_2}^2} - \frac{3\eta_H\eta_{\mathcal{H}_2} Y_u^{SM}}{16\pi^2 m_{\mathcal{H}_2}^2} - \frac{3\eta_H\lambda_{\mathcal{H}_2,1} Y_{\mathcal{H}_2}^{(u)}}{16\pi^2 m_{\mathcal{H}_2}^2} + \frac{3\eta_{\mathcal{H}_2}\lambda_{\mathcal{H}_2,1} Y_{\mathcal{H}_2}^{(u)}}{16\pi^2 m_{\mathcal{H}_2}^2} - \frac{\eta_H\lambda_{\mathcal{H}_2,2} Y_{\mathcal{H}_2}^{(u)}}{4\pi^2 m_{\mathcal{H}_2}^2} + \frac{3\eta_{\mathcal{H}_2}\lambda_{\mathcal{H}_2,2} Y_{\mathcal{H}_2}^{(u)}}{16\pi^2 m_{\mathcal{H}_2}^2} + \frac{\lambda_{\mathcal{H}_2,2}^2 Y_u^{SM}}{192\pi^2 m_{\mathcal{H}_2}^2} + \frac{\lambda_{\mathcal{H}_2,3}^2 Y_u^{SM}}{48\pi^2 m_{\mathcal{H}_2}^2} - \frac{5\eta_H\lambda_{\mathcal{H}_2,3} Y_{\mathcal{H}_2}^{(u)}}{8\pi^2 m_{\mathcal{H}_2}^2}$
Q_H	$\frac{3\eta_H^2\lambda_{\mathcal{H}_2}}{32\pi^2 m_{\mathcal{H}_2}^2} + \frac{17\eta_H^2\lambda_H^{SM}}{16\pi^2 m_{\mathcal{H}_2}^2} + \frac{\eta_H^2}{m_{\mathcal{H}_2}^2} - \frac{3\eta_H^2\lambda_{\mathcal{H}_2,1}}{4\pi^2 m_{\mathcal{H}_2}^2} - \frac{3\eta_H\eta_{\mathcal{H}_2}\lambda_H^{SM}}{8\pi^2 m_{\mathcal{H}_2}^2} + \frac{3\eta_H\eta_{\mathcal{H}_2}\lambda_{\mathcal{H}_2,1}}{8\pi^2 m_{\mathcal{H}_2}^2} - \frac{13\eta_H^2\lambda_{\mathcal{H}_2,2}}{16\pi^2 m_{\mathcal{H}_2}^2} + \frac{3\eta_H\eta_{\mathcal{H}_2}\lambda_{\mathcal{H}_2,2}}{8\pi^2 m_{\mathcal{H}_2}^2} - \frac{\lambda_{\mathcal{H}_2,1}^3}{48\pi^2 m_{\mathcal{H}_2}^2} + \frac{\lambda_H^{SM}\lambda_{\mathcal{H}_2,2}^2}{96\pi^2 m_{\mathcal{H}_2}^2} - \frac{\lambda_{\mathcal{H}_2,1}^2\lambda_{\mathcal{H}_2,2}}{32\pi^2 m_{\mathcal{H}_2}^2} - \frac{\lambda_{\mathcal{H}_2,1}\lambda_{\mathcal{H}_2,2}^2}{32\pi^2 m_{\mathcal{H}_2}^2} - \frac{7\eta_H^2\lambda_{\mathcal{H}_2,3}}{4\pi^2 m_{\mathcal{H}_2}^2} + \frac{\lambda_H^{SM}\lambda_{\mathcal{H}_2,3}^2}{24\pi^2 m_{\mathcal{H}_2}^2} - \frac{\lambda_{\mathcal{H}_2,2}^3}{96\pi^2 m_{\mathcal{H}_2}^2} - \frac{\lambda_{\mathcal{H}_2,1}\lambda_{\mathcal{H}_2,3}^2}{8\pi^2 m_{\mathcal{H}_2}^2} - \frac{\lambda_{\mathcal{H}_2,2}\lambda_{\mathcal{H}_2,3}^2}{8\pi^2 m_{\mathcal{H}_2}^2}$
$Q_{H\Box}$	$-\frac{g_W^4}{7680\pi^2 m_{\mathcal{H}_2}^2} - \frac{3\eta_H^2}{32\pi^2 m_{\mathcal{H}_2}^2} - \frac{\lambda_{\mathcal{H}_2,1}^2}{96\pi^2 m_{\mathcal{H}_2}^2} - \frac{\lambda_{\mathcal{H}_2,1}\lambda_{\mathcal{H}_2,2}}{96\pi^2 m_{\mathcal{H}_2}^2} + \frac{\lambda_{\mathcal{H}_2,3}^2}{48\pi^2 m_{\mathcal{H}_2}^2}$
Q_{HD}	$-\frac{g_Y^4}{1920\pi^2 m_{\mathcal{H}_2}^2} - \frac{\lambda_{\mathcal{H}_2,2}^2}{96\pi^2 m_{\mathcal{H}_2}^2} + \frac{\lambda_{\mathcal{H}_2,3}^2}{24\pi^2 m_{\mathcal{H}_2}^2}$
Q_{HB}	$\frac{g_Y^2\lambda_{\mathcal{H}_2,1}}{384\pi^2 m_{\mathcal{H}_2}^2} + \frac{g_Y^2\lambda_{\mathcal{H}_2,2}}{768\pi^2 m_{\mathcal{H}_2}^2}$
Q_{HW}	$\frac{g_W^2\lambda_{\mathcal{H}_2,1}}{384\pi^2 m_{\mathcal{H}_2}^2} + \frac{g_W^2\lambda_{\mathcal{H}_2,2}}{768\pi^2 m_{\mathcal{H}_2}^2}$
Q_{HWB}	$\frac{g_W g_Y\lambda_{\mathcal{H}_2,2}}{384\pi^2 m_{\mathcal{H}_2}^2}$

(Table continued)

TABLE III. *(Continued)*

Dimension-six operators	Wilson coefficients
$Q_{Hl}^{(1)}$	$\frac{g_Y^4}{3840\pi^2 m_{\mathcal{H}_2}^2}$
$Q_{Hq}^{(1)}$	$-\frac{g_Y^4}{11520\pi^2 m_{\mathcal{H}_2}^2}$
Q_{Hd}	$\frac{g_Y^4}{5760\pi^2 m_{\mathcal{H}_2}^2}$
Q_{He}	$\frac{g_Y^4}{1920\pi^2 m_{\mathcal{H}_2}^2}$
Q_{Hu}	$-\frac{g_Y^4}{2880\pi^2 m_{\mathcal{H}_2}^2}$
$Q_{Hl}^{(3)}$	$-\frac{g_W^4}{1920\pi^2 m_{\mathcal{H}_2}^2}$
$Q_{Hq}^{(3)}$	$-\frac{g_W^4}{1920\pi^2 m_{\mathcal{H}_2}^2}$
Q_W	$\frac{g_W^3}{5760\pi^2 m_{\mathcal{H}_2}^2}$
Q_{ll}	$-\frac{g_W^4}{7680\pi^2 m_{\mathcal{H}_2}^2} - \frac{g_Y^4}{7680\pi^2 m_{\mathcal{H}_2}^2}$
$Q_{ud}^{(1)}$	$\frac{g_Y^4}{4320\pi^2 m_{\mathcal{H}_2}^2}$
$Q_{lq}^{(3)}$	$-\frac{g_W^4}{3840\pi^2 m_{\mathcal{H}_2}^2}$
$Q_{qq}^{(3)}$	$-\frac{g_W^4}{7680\pi^2 m_{\mathcal{H}_2}^2}$
Q_{dd}	$-\frac{g_Y^4}{17280\pi^2 m_{\mathcal{H}_2}^2}$
Q_{ed}	$-\frac{g_Y^4}{2880\pi^2 m_{\mathcal{H}_2}^2}$
Q_{ee}	$-\frac{g_Y^4}{1920\pi^2 m_{\mathcal{H}_2}^2}$
Q_{eu}	$\frac{g_Y^4}{1440\pi^2 m_{\mathcal{H}_2}^2}$
Q_{uu}	$-\frac{g_Y^4}{4320\pi^2 m_{\mathcal{H}_2}^2}$
Q_{lu}	$\frac{g_Y^4}{2880\pi^2 m_{\mathcal{H}_2}^2}$
Q_{qe}	$\frac{g_Y^4}{5760\pi^2 m_{\mathcal{H}_2}^2}$
Q_{ld}	$-\frac{g_Y^4}{5760\pi^2 m_{\mathcal{H}_2}^2}$
$Q_{qq}^{(1)}$	$-\frac{g_Y^4}{69120\pi^2 m_{\mathcal{H}_2}^2}$
Q_{le}	$-\frac{g_Y^4}{1920\pi^2 m_{\mathcal{H}_2}^2} - \frac{3\lambda_{\mathcal{H}_2} Y_{\mathcal{H}_2}^{(e)\,2}}{128\pi^2 m_{\mathcal{H}_2}^2} - \frac{Y_{\mathcal{H}_2}^{(e)\,2}}{4m_{\mathcal{H}_2}^2}$
$Q_{qd}^{(1)}$	$\frac{g_Y^4}{17280\pi^2 m_{\mathcal{H}_2}^2} - \frac{3\lambda_{\mathcal{H}_2} Y_{\mathcal{H}_2}^{(d)\,2}}{128\pi^2 m_{\mathcal{H}_2}^2} - \frac{Y_{\mathcal{H}_2}^{(d)\,2}}{4m_{\mathcal{H}_2}^2}$
$Q_{qu}^{(1)}$	$-\frac{g_Y^4}{8640\pi^2 m_{\mathcal{H}_2}^2} - \frac{3\lambda_{\mathcal{H}_2} Y_{\mathcal{H}_2}^{(u)\,2}}{128\pi^2 m_{\mathcal{H}_2}^2} - \frac{Y_{\mathcal{H}_2}^{(u)\,2}}{4m_{\mathcal{H}_2}^2}$
$Q_{quqd}^{(1)}$	$-\frac{3\lambda_{\mathcal{H}_2} Y_{\mathcal{H}_2}^{(d)} Y_{\mathcal{H}_2}^{(u)}}{64\pi^2 m_{\mathcal{H}_2}^2} - \frac{Y_{\mathcal{H}_2}^{(d)} Y_{\mathcal{H}_2}^{(u)}}{2m_{\mathcal{H}_2}^2}$
$Q_{lequ}^{(1)}$	$\frac{3\lambda_{\mathcal{H}_2} Y_{\mathcal{H}_2}^{(e)} Y_{\mathcal{H}_2}^{(u)}}{64\pi^2 m_{\mathcal{H}_2}^2} + \frac{Y_{\mathcal{H}_2}^{(e)} Y_{\mathcal{H}_2}^{(u)}}{2m_{\mathcal{H}_2}^2}$
$Q_{lq}^{(1)}$	$\frac{g_Y^4}{11520\pi^2 m_{\mathcal{H}_2}^2}$
Q_{ledq}	$\frac{3\lambda_{\mathcal{H}_2} Y_{\mathcal{H}_2}^{(d)} Y_{\mathcal{H}_2}^{(e)}}{64\pi^2 m_{\mathcal{H}_2}^2} + \frac{Y_{\mathcal{H}_2}^{(d)} Y_{\mathcal{H}_2}^{(e)}}{2m_{\mathcal{H}_2}^2}$

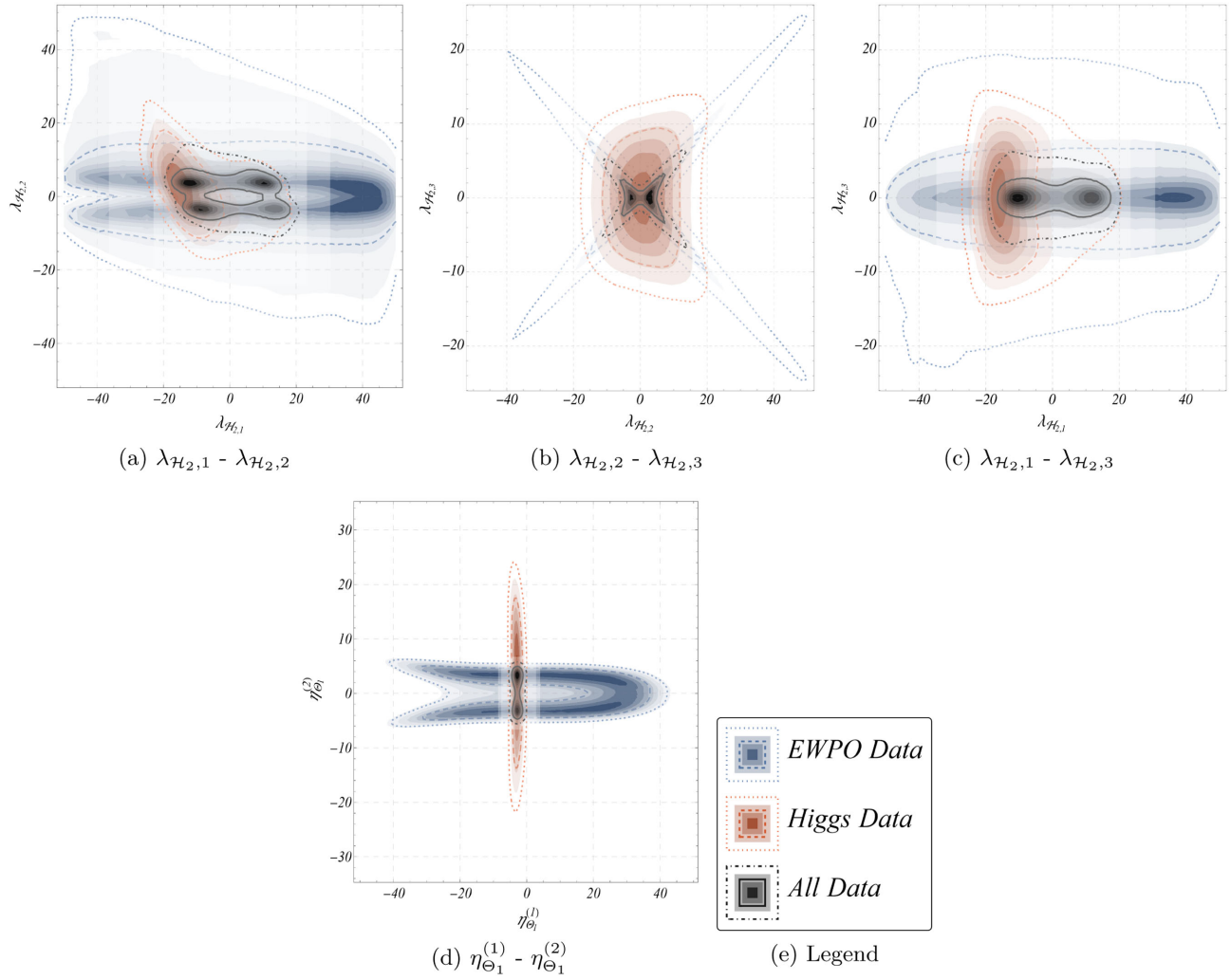

(a) $\lambda_{\mathcal{H}_2,1}$ - $\lambda_{\mathcal{H}_2,2}$ (b) $\lambda_{\mathcal{H}_2,2}$ - $\lambda_{\mathcal{H}_2,3}$ (c) $\lambda_{\mathcal{H}_2,1}$ - $\lambda_{\mathcal{H}_2,3}$

(d) $\eta^{(1)}_{\Theta_1}$ - $\eta^{(2)}_{\Theta_1}$ (e) Legend

FIG. 5. Two-dimensional marginalized posteriors among the BSM parameters for $\mathcal{H}_2$ [panels (a)–(c)] and Θ_1 [panel (d)]. The line contours represent the 68% and 95% CIs and the filled contours with changing opacity show the high-probability regions with decreasing probabilities (darker to lighter). We show the results from a fit of "EWPO" data only (blue), "Higgs" data only (red), and for "All" data (black).

relaxed compared to the others. This happens primarily because in the case of EWPOs $\lambda_{\mathcal{H}_2,1}$ gets constrained through Q_H whose contribution only appears at two loops in the SMEFT parametrization of m_W and is very small. For other data sets, on the other hand, $\lambda_{\mathcal{H}_2,1}$ gets bounded from the operators $Q_{H\Box}$, Q_{HB}, Q_{HW}, in addition to Q_H. The corresponding WCs receive strong constraints from Higgs signal strengths and in particular from di-Higgs data, as depicted by the corresponding parameter spaces.

2. Model-dependent constraints on the WCs

As mentioned at the beginning of this section, we take our model-independent analysis in Sec. IV to the next step by determining the allowed WC spaces for specific models, using their parameter posteriors and the WC-matching results obtained after integrating out the heavy BSM particle. In this case, the matched WCs are functions of BSM parameters and dependent on one another. The WC spaces obtained in this way are directed from the constraints of the relevant model parameters and thus are termed "model dependent." Using the large MCMC samples generated from the model-parameter posterior, we generate the multivariate distributions of those WCs (now functions of model parameters). We show these distributions in the WC space with the help of marginal posteriors of two WCs at a time.

For $\mathcal{H}_2$, we generate the distributions of the WCs (black) using relations (obtained after matching) from Table III expressed in terms of the parameters $\lambda_{\mathcal{H}_2,1}$, $\lambda_{\mathcal{H}_2,2}$, and $\lambda_{\mathcal{H}_2,3}$, and propagate the model-parameter posteriors. As before, we demonstrate the relative effects of the "All," "EWPO," and "Higgs" data sets separately. Instead of showing all of the possible two-dimensional marginal contour plots for the WCs, we choose to show a few sample plots in Fig. 6.

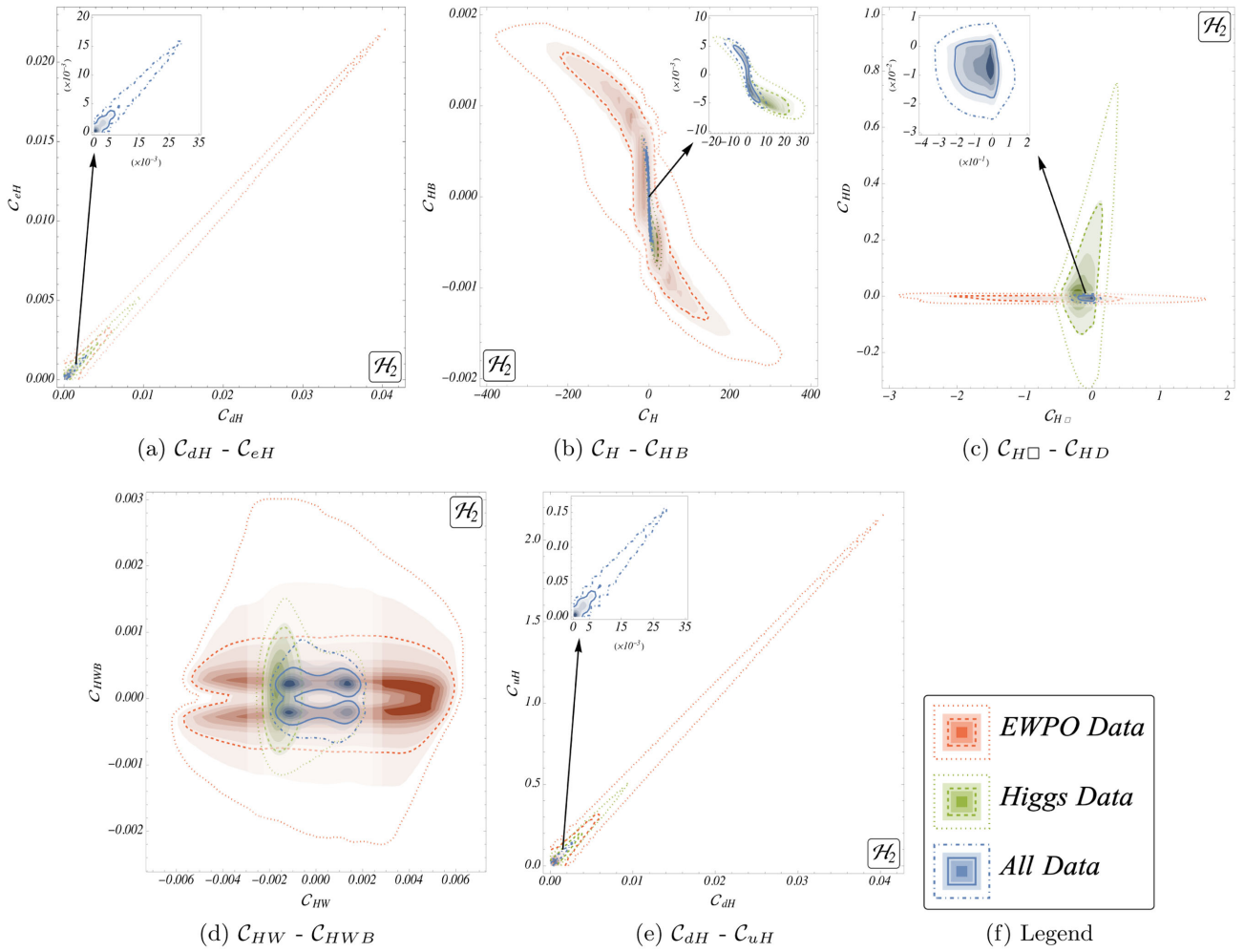

(a) $\mathcal{C}_{dH}$ - $\mathcal{C}_{eH}$ (b) $\mathcal{C}_H$ - $\mathcal{C}_{HB}$ (c) $\mathcal{C}_{H\Box}$ - $\mathcal{C}_{HD}$

(d) $\mathcal{C}_{HW}$ - $\mathcal{C}_{HWB}$ (e) $\mathcal{C}_{dH}$ - $\mathcal{C}_{uH}$ (f) Legend

FIG. 6. Two-dimensional posteriors among the relevant WCs induced by $\mathcal{H}_2$, listed in black in Table III. These regions are obtained from the parameter distributions among $\lambda_{\mathcal{H}_2,1}$, $\lambda_{\mathcal{H}_2,2}$, and $\lambda_{\mathcal{H}_2,3}$ shown in Figs. 5(a)–5(c). The line contours represent the 68% and 95% CI and the filled contours with changing opacity denote the high-probability regions with decreasing probabilities (darker to lighter). We separate the results from fitting "EWPO" data only (red), "Higgs" data only (green), and "All" data (blue).

Solid blue (dashed red/green) constant-probability contours enclose the 68% credible region and dot-dashed blue (dotted red/green) ones enclose the 95% credible region, respectively. Colored regions (blue/red/green) with variable density depict the high-probability regions. In some cases, the parameter spaces obtained for the three data sets differ from one another by one or more orders of magnitude. For instance, the bluish regions corresponding to "All" measurements are imperceptibly tiny in comparison to those corresponding to both the "EWPO" (red) and "Higgs" (green) data sets. For ease of viewing, we magnify such regions and show them as insets.

As mentioned earlier, these obtained WC spaces are related by nonlinear relations of the model parameters. This is explicitly seen from the WC expressions for $\mathcal{C}_{dH}$, $\mathcal{C}_{eH}$ and $\mathcal{C}_{uH}$ in Table III which, after taking the contributions from the relevant BSM parameters, turn out to be positive definite. As a result, the corresponding parameter spaces shown in Figs. 6(a) and 6(e) are delimited only in the positive quadrant.

B. Scalar leptoquark: $\Theta_1 \equiv (\mathbf{3}_C, \mathbf{2}_L, \frac{\mathbf{1}}{\mathbf{6}}|_Y)$

In this model, we extend the SM by a color-triplet isospin-doublet scalar (Θ_1) with hypercharge $Y = \frac{1}{6}$. We consider the BSM Lagrangian [127,128]

$$\begin{aligned}\mathcal{L}_{\Theta_1} = \mathcal{L}_{\rm SM}^{d\le 4} &+ (D_\mu \Theta_1)^\dagger (D^\mu \Theta_1) - m_{\Theta_1}^2 \Theta_1^\dagger \Theta_1 \\ &- \eta_{\Theta_1}^{(1)} H^\dagger H \Theta_1^\dagger \Theta_1 - \eta_{\Theta_1}^{(2)} (H^\dagger \sigma^i H)(\Theta_1^\dagger \sigma^i \Theta_1) \\ &- \lambda_{\Theta_1}^{(1)} (\Theta_1^\dagger \Theta_1)^2 - \lambda_{\Theta_1}^{(2)} (\Theta_1^\dagger \sigma^i \Theta_1)^2 \\ &+ \{ y_{\Theta_1} \Theta_1^\alpha \bar{d}_R^\alpha i\sigma^2 l_L + \text{H.c.} \}. \end{aligned} \tag{5.2}$$

Here, m_{Θ_1} is the mass of the heavy field, i.e., the cutoff scale appears in the WCs. This model contains five BSM parameters

TABLE IV. Warsaw basis effective operators and the associated WCs that emerge after integrating out the heavy field Θ_1: $(3,2,\frac{1}{6})$. See Table III for color coding.

Dimension-six ops.	Wilson coefficients
Q_{HB}	$\frac{g_Y^2 \eta_{\Theta_1}^{(1)}}{1152\pi^2 m_{\Theta_1}^2}$
$Q_{H\Box}$	$-\frac{g_W^4}{2560\pi^2 m_{\Theta_1}^2} - \frac{\eta_{\Theta_1}^{(1)\,2}}{32\pi^2 m_{\Theta_1}^2} + \frac{\eta_{\Theta_1}^{(2)\,2}}{512\pi^2 m_{\Theta_1}^2}$
Q_{HD}	$-\frac{g_Y^4}{5760\pi^2 m_{\Theta_1}^2} - \frac{\eta_{\Theta_1}^{(2)\,2}}{128\pi^2 m_{\Theta_1}^2}$
Q_{HG}	$\frac{g_S^2 \eta_{\Theta_1}^{(1)}}{192\pi^2 m_{\Theta_1}^2}$
Q_{HW}	$\frac{g_W^2 \eta_{\Theta_1}^{(1)}}{128\pi^2 m_{\Theta_1}^2}$
Q_{HWB}	$\frac{g_W g_Y \eta_{\Theta_1}^{(2)}}{768\pi^2 m_{\Theta_1}^2}$
Q_{uH}	$\frac{\eta_{\Theta_1}^{(2)\,2} Y_u^{\rm SM}}{256\pi^2 m_{\Theta_1}^2}$
Q_{dH}	$\frac{\eta_{\Theta_1}^{(2)\,2} Y_d^{\rm SM}}{256\pi^2 m_{\Theta_1}^2}$
Q_{eH}	$\frac{\eta_{\Theta_1}^{(2)\,2} Y_e^{\rm SM}}{256\pi^2 m_{\Theta_1}^2}$
Q_H	$-\frac{\eta_{\Theta_1}^{(1)\,3}}{16\pi^2 m_{\Theta_1}^2} - \frac{3\eta_{\Theta_1}^{(1)}\eta_{\Theta_1}^{(2)\,2}}{256\pi^2 m_{\Theta_1}^2} + \frac{\eta_{\Theta_1}^{(2)\,2}\lambda_H^{\rm SM}}{128\pi^2 m_{\Theta_1}^2}$
Q_{ll}	$-\frac{g_W^4}{2560\pi^2 m_{\Theta_1}^2} - \frac{g_Y^4}{23040\pi^2 m_{\Theta_1}^2}$
$Q_{Hl}^{(1)}$	$\frac{g_Y^4}{11520\pi^2 m_{\Theta_1}^2}$
$Q_{Hq}^{(1)}$	$-\frac{g_Y^4}{34560\pi^2 m_{\Theta_1}^2}$
$Q_{Hl}^{(3)}$	$-\frac{g_W^4}{640\pi^2 m_{\Theta_1}^2}$
$Q_{Hq}^{(3)}$	$-\frac{g_W^4}{640\pi^2 m_{\Theta_1}^2}$
Q_G	$\frac{g_S^3}{2880\pi^2 m_{\Theta_1}^2}$
Q_{Hu}	$-\frac{g_Y^4}{8640\pi^2 m_{\Theta_1}^2}$
Q_{Hd}	$\frac{g_Y^4}{17280\pi^2 m_{\Theta_1}^2}$
Q_{He}	$\frac{g_Y^4}{5760\pi^2 m_{\Theta_1}^2}$
Q_W	$\frac{g_W^3}{1920\pi^2 m_{\Theta_1}^2}$
$Q_{lq}^{(1)}$	$\frac{g_Y^4}{34560\pi^2 m_{\Theta_1}^2}$
$Q_{qd}^{(1)}$	$\frac{g_Y^4}{51840\pi^2 m_{\Theta_1}^2}$
$Q_{qq}^{(1)}$	$-\frac{g_Y^4}{207360\pi^2 m_{\Theta_1}^2}$
$Q_{qu}^{(1)}$	$-\frac{g_Y^4}{25920\pi^2 m_{\Theta_1}^2}$
$Q_{ud}^{(1)}$	$\frac{g_Y^4}{12960\pi^2 m_{\Theta_1}^2}$
$Q_{lq}^{(3)}$	$-\frac{g_W^4}{1280\pi^2 m_{\Theta_1}^2}$
$Q_{qq}^{(3)}$	$-\frac{g_W^4}{2560\pi^2 m_{\Theta_1}^2}$
Q_{dd}	$-\frac{g_Y^4}{51840\pi^2 m_{\Theta_1}^2}$
Q_{ed}	$-\frac{g_Y^4}{8640\pi^2 m_{\Theta_1}^2}$
Q_{ee}	$-\frac{g_Y^4}{5760\pi^2 m_{\Theta_1}^2}$
Q_{ld}	$-\frac{g_Y^4}{17280\pi^2 m_{\Theta_1}^2} - \frac{9y_{\Theta_1}^2(4\lambda_{\Theta_1}^{(1)}+\lambda_{\Theta_1}^{(2)})}{128\pi^2 m_{\Theta_1}^2} - \frac{y_{\Theta_1}^2}{4m_{\Theta_1}^2}$
Q_{le}	$-\frac{g_Y^4}{5760\pi^2 m_{\Theta_1}^2}$
Q_{lu}	$\frac{g_Y^4}{8640\pi^2 m_{\Theta_1}^2}$
Q_{eu}	$\frac{g_Y^4}{4320\pi^2 m_{\Theta_1}^2}$
$Q_{qu}^{(8)}$	$-\frac{g_S^4}{480\pi^2 m_{\Theta_1}^2}$
Q_{qe}	$\frac{g_Y^4}{17280\pi^2 m_{\Theta_1}^2}$
Q_{uu}	$-\frac{g_Y^4}{12960\pi^2 m_{\Theta_1}^2}$
$Q_{ud}^{(8)}$	$-\frac{g_S^4}{480\pi^2 m_{\Theta_1}^2}$
$Q_{qd}^{(8)}$	$-\frac{g_S^4}{480\pi^2 m_{\Theta_1}^2}$

($\eta_{\Theta_1}^{(1)}$, $\eta_{\Theta_1}^{(2)}$, $\lambda_{\Theta_1}^{(1)}$, $\lambda_{\Theta_1}^{(2)}$, and y_{Θ_1}) and the WCs are functions of these parameters on top of the SM ones; see Table IV. In the BSM Yukawa coupling, we assume that y_{Θ_1} couples to third-generation fermions only. As mentioned earlier, not all of the emergent operators affect our selected observables; Q_{uH}, Q_{dH}, Q_{eH}, Q_H, Q_{HW}, Q_{HB}, Q_{HWB}, Q_{HG}, $Q_{H\Box}$, and Q_{HD} are the only relevant operators for our analysis. Thus, out of these five BSM parameters, only $\eta_{\Theta_1}^{(1)}$ and $\eta_{\Theta_1}^{(2)}$ get constrained by the experimental data, while the others play no role. To constrain them, we need to add more observables that get contributions from the Q_{ld} operators; see Table IV. Note that the unconstrained operators (functions of the BSM parameters) generated in the two example models are mutually exclusive. The additional observables required for these scenarios also do not overlap. Thus, to constrain all of the BSM parameters,[7] one may have to look for some of the observables for individual models case by case.

1. Constraints on the model parameters $\eta_{\Theta_1}^{(1)}$, $\eta_{\Theta_1}^{(2)}$

With uniform priors within the range $\{-50, 50\}$ and following the same methodology as mentioned for $\mathcal{H}_2$, we show the parameter space of the two BSM couplings ($\eta_{\Theta_1}^{(1)}$

[7]The corrections to the low-energy observables including the electric dipole moments require an enhancement in the SMEFT operator list to include multiple generations of fermions (see Refs. [182,183]), which is beyond the scope of this paper. In this work, we only concern ourselves with flavor-diagonal operators. We leave the flavor off-diagonal scenario as a future project.

and $\eta^{(2)}_{\Theta_1}$) for model Θ_1 as two-dimensional marginalized posteriors in Fig. 5(d), for the same data sets as before: "EWPO" (blue), "Higgs" (red), and "All" (black). The figure shows that the "EWPO" bound on $\eta^{(1)}_{\Theta_1}$ is the most relaxed, owing to the loop-order contribution to Q_H, whereas those allowed by the "Higgs" and "All" data sets are of almost the same order and have negative limits. This is because, in addition to Q_H, there are other operators like Q_{HB}, $Q_{H\Box}$, Q_{HG}, and Q_{HW} that give relatively stronger contributions to the other two data sets. In contrast, the constraints on $\eta^{(2)}_{\Theta_1}$ are the weakest from "Higgs" data, and those from "EWPO" and "All" data have similar values. This is a consequence of the strong contribution from Q_{HWB} and Q_{HD} to "EWPO," which is also evident for "All" measurements.

2. *Model-dependent constraints on the WCs*

In the next part of the analysis, similar to the case of $\mathcal{H}_2$, distributions are generated for the ten WCs of the model Θ_1 (expressions in black in Table IV) for the three different data sets. Similar to Fig. 6, a selection of two-dimensional marginal distributions are shown in Fig. 7 for Θ_1. As already noted, these WC distributions are generated from the model-parameter posteriors (i.e., $\eta^{(1)}_{\Theta_1}$ and $\eta^{(2)}_{\Theta_1}$), using the expressions listed in Table IV. The WCs $\mathcal{C}_{eH}$, $\mathcal{C}_{dH}$, and $\mathcal{C}_{uH}$, representing Yukawa-type interactions, are functions of the squared power of $\eta^{(2)}_{\Theta_1}$. As a result, these WCs will only take positive values when determined in the Θ_1 model. This is clearly shown in the two-dimensional marginalized WC distributions in Figs. 7(a) and 7(e). The opposite behavior is visible in the WC space of $\mathcal{C}_{HD}$ in Fig. 7(c), which yields negative limits. From Fig. 5(d) it is evident that the constraints for $\eta^{(1)}_{\Theta_1}$ for the "Higgs" and "All" data sets have negative limits. This leads to the negative bounds on Q_{HW} which is a linear function of $\eta^{(1)}_{\Theta_1}$, as depicted in Fig. 7(d) for the corresponding data sets.

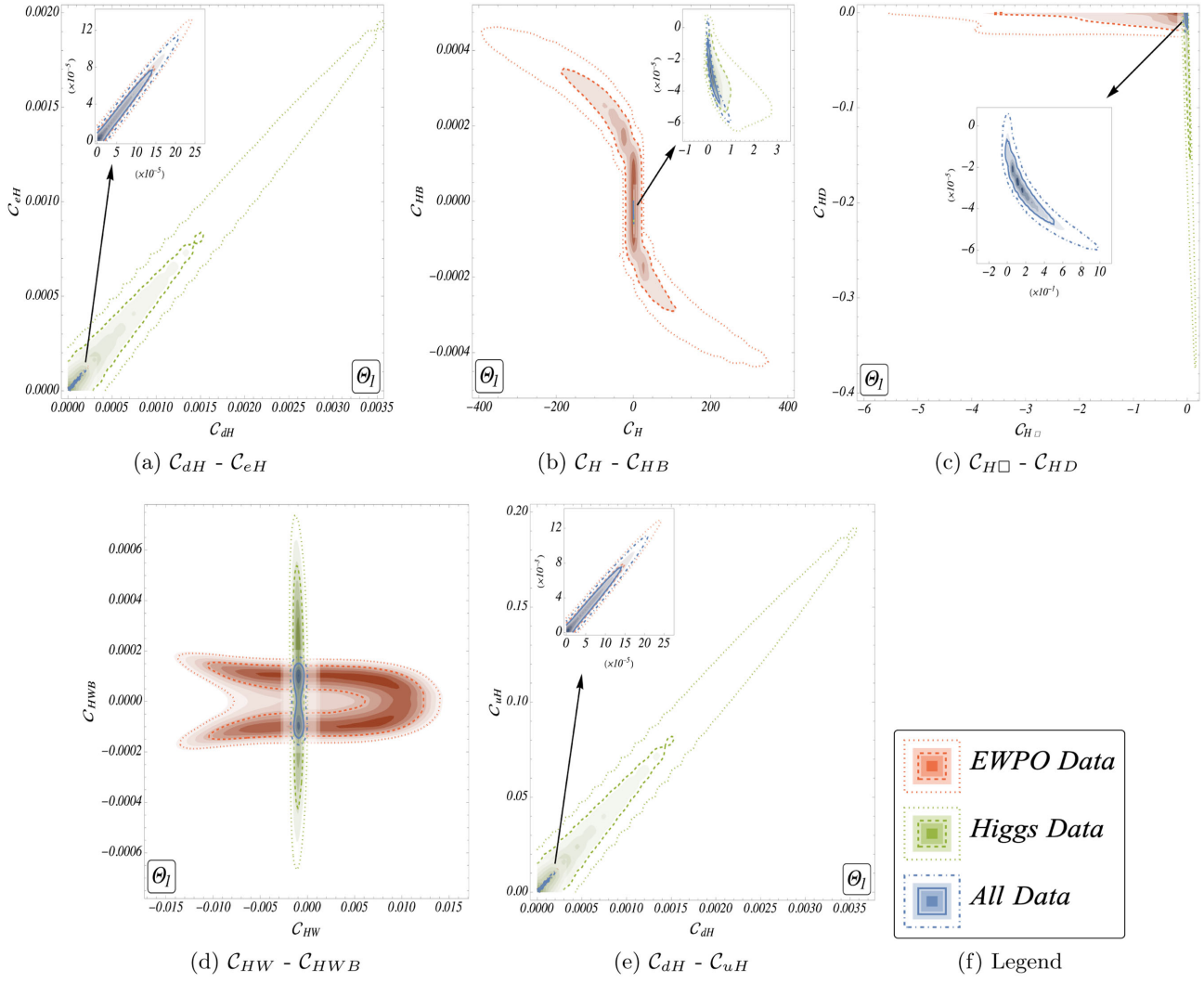

(a) $\mathcal{C}_{dH}$ - $\mathcal{C}_{eH}$ (b) $\mathcal{C}_{H}$ - $\mathcal{C}_{HB}$ (c) $\mathcal{C}_{H\Box}$ - $\mathcal{C}_{HD}$

(d) $\mathcal{C}_{HW}$ - $\mathcal{C}_{HWB}$ (e) $\mathcal{C}_{dH}$ - $\mathcal{C}_{uH}$ (f) Legend

FIG. 7. Two-dimensional WC posteriors, similar to Fig. 6, obtained from the parameter distributions of $\eta^{(1)}_{\Theta_1}$, $\eta^{(2)}_{\Theta_1}$ for Θ_1.

Order-of-magnitude variations in the size of the WC spaces between models, as shown in Figs. 6 and 7, point to the significance of the SMEFT matching expressions as well as the BSM parameter spaces in determining model-dependent WC constraints.

VI. EFFECT OF RENORMALIZATION GROUP EQUATIONS ON THE MODEL-DEPENDENT ANALYSIS

In Sec. V the SMEFT matching of the BSM theory with a heavy scalar field was performed at the high scale Λ, which was taken as the mass of the heavy scalar m_{hf}. There, we ignored the running of the SMEFT operators, which emerged at the high scale Λ, up to the electroweak scale where they were eventually mapped into the experimental observables. In this section, the operators generated by integrating out the heavy scalar doublet $\mathcal{H}_2$ at the scale Λ are evolved to the M_Z scale using the RGEs given in Refs. [184–186]. The WCs at M_Z, $\mathcal{C}_i(M_Z)$, are computed using the matching scale WCs $\mathcal{C}_i(\Lambda)$ and the SMEFT anomalous dimension matrix γ_{ij} in the leading-log approximation,

$$\frac{d\mathcal{C}_i(\mu)}{d\log\mu} = \sum_j \frac{1}{16\pi^2}\gamma_{ij}\mathcal{C}_j,$$

and, at leading order,

$$\mathcal{C}_i(M_Z) = \mathcal{C}_i(\Lambda) + \sum_j \frac{1}{16\pi^2}\gamma_{ij}\mathcal{C}_j(\Lambda)\log\left[\frac{M_Z}{\Lambda}\right]. \quad (6.1)$$

For $\mathcal{H}_2$, a total of 51 operators are generated, 14 of which are exclusively induced by the RG running, and the RG-evolved matching result is available at the Github repository. Using these RG-evolved matching relations of the WCs, the constraints on the BSM parameters $\lambda_{\mathcal{H}_2,1}$, $\lambda_{\mathcal{H}_2,2}$, and $\lambda_{\mathcal{H}_2,3}$ are obtained using "All" experimental measurements listed in Table I and the corresponding

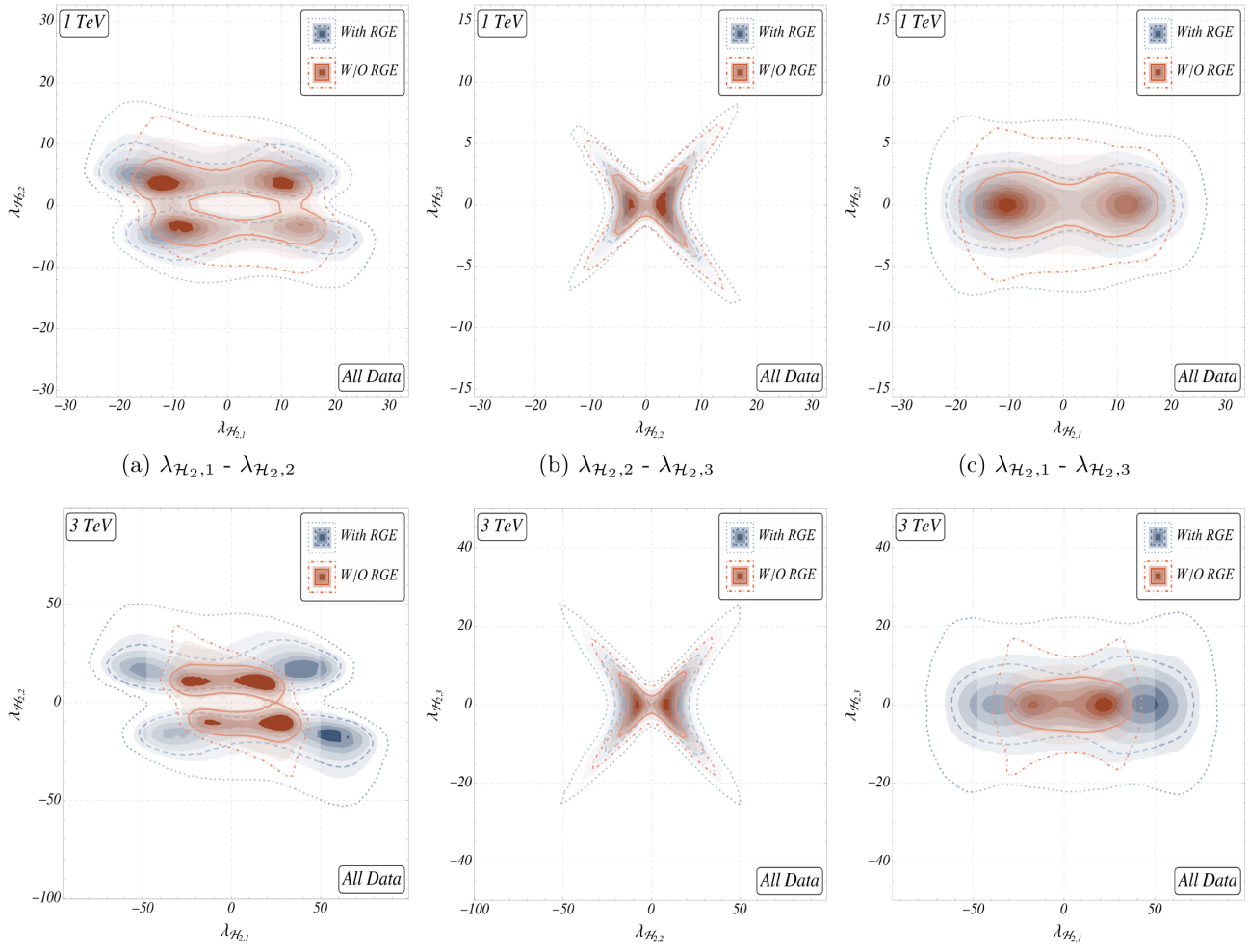

(a) $\lambda_{\mathcal{H}_2,1}$ - $\lambda_{\mathcal{H}_2,2}$ (b) $\lambda_{\mathcal{H}_2,2}$ - $\lambda_{\mathcal{H}_2,3}$ (c) $\lambda_{\mathcal{H}_2,1}$ - $\lambda_{\mathcal{H}_2,3}$

(d) $\lambda_{\mathcal{H}_2,1}$ - $\lambda_{\mathcal{H}_2,2}$ (e) $\lambda_{\mathcal{H}_2,2}$ - $\lambda_{\mathcal{H}_2,3}$ (f) $\lambda_{\mathcal{H}_2,1}$ - $\lambda_{\mathcal{H}_2,3}$

FIG. 8. (a)–(f) Two-dimensional marginalized posteriors among the BSM parameters for $\mathcal{H}_2$ for $m_{\mathcal{H}_2} = 1$ TeV (top row) and $m_{\mathcal{H}_2} = 3$ TeV (bottom row). We show the results from a fit with "All" data. The credible regions shown in blue correspond to the model parameter spaces obtained after including RG-evolved operators, while in the regions shown in red these are ignored.

two-dimensional marginalized posteriors are shown in Fig. 8 with $m_{\mathcal{H}_2}$ set to 1 TeV. In the same figure, to see the effect of RG running, we show the two-dimensional marginalized model parameter posteriors obtained neglecting RG running (these are the ones shown in black in the top row of Fig. 5). It can be seen that the obtained parameter spaces are relaxed after including the RG effects in the analysis. Further, we also study the effects on the constraints for different choices of $m_{\mathcal{H}_2}$. We observe that the constraints on the BSM parameters decrease with higher values of $m_{\mathcal{H}_2}$. We show the allowed parameter spaces for $m_{\mathcal{H}_2}$ set to 3 TeV in the bottom row of Fig. 8. On comparing the red (without RGE) and blue (with RGE) regions in the top row (with $m_{\mathcal{H}_2} = 1$ TeV) with the corresponding ones in the bottom row (with $m_{\mathcal{H}_2} = 3$ TeV), we note that the model parameter constraints decrease with an increase in $m_{\mathcal{H}_2}$.

The model-dependent WCs' credible regions obtained from the model parameter posteriors and RG-evolved matching results are shown in Fig. 9. We show two-dimensional marginalized sample plots. Similar to Fig. 8, we also show the WC regions obtained when ignoring the RG running in red. These plots show the similar trend that the allowed credible regions are comparatively enlarged when the RGE effects are included. These parameter spaces are further relaxed for higher values of $m_{\mathcal{H}_2}$.

After including the RG running of the SMEFT operators, the WC relations of 23 SMEFT operators are given as functions of the model parameters $\lambda_{\mathcal{H}_2,1}$, $\lambda_{\mathcal{H}_2,2}$, and $\lambda_{\mathcal{H}_2,3}$. Thus, using the model parameter posterior distributions in the RG-evolved matching relations, the multivariate distributions are obtained for these 23 WCs. This list includes some operators (e.g., Q_{uB}, Q_{uW}, Q_{dB}, Q_{dW}, Q_{ueB}, Q_{eW}) which are not constrained in the model-independent analysis by the experimental measurements. We show example plots of the regions of such model-dependent WCs in Fig. 10. The operators Q_{uB}, Q_{uW}, Q_{eB}, and Q_{Hud} are RGE generated, and the corresponding WCs include an extra

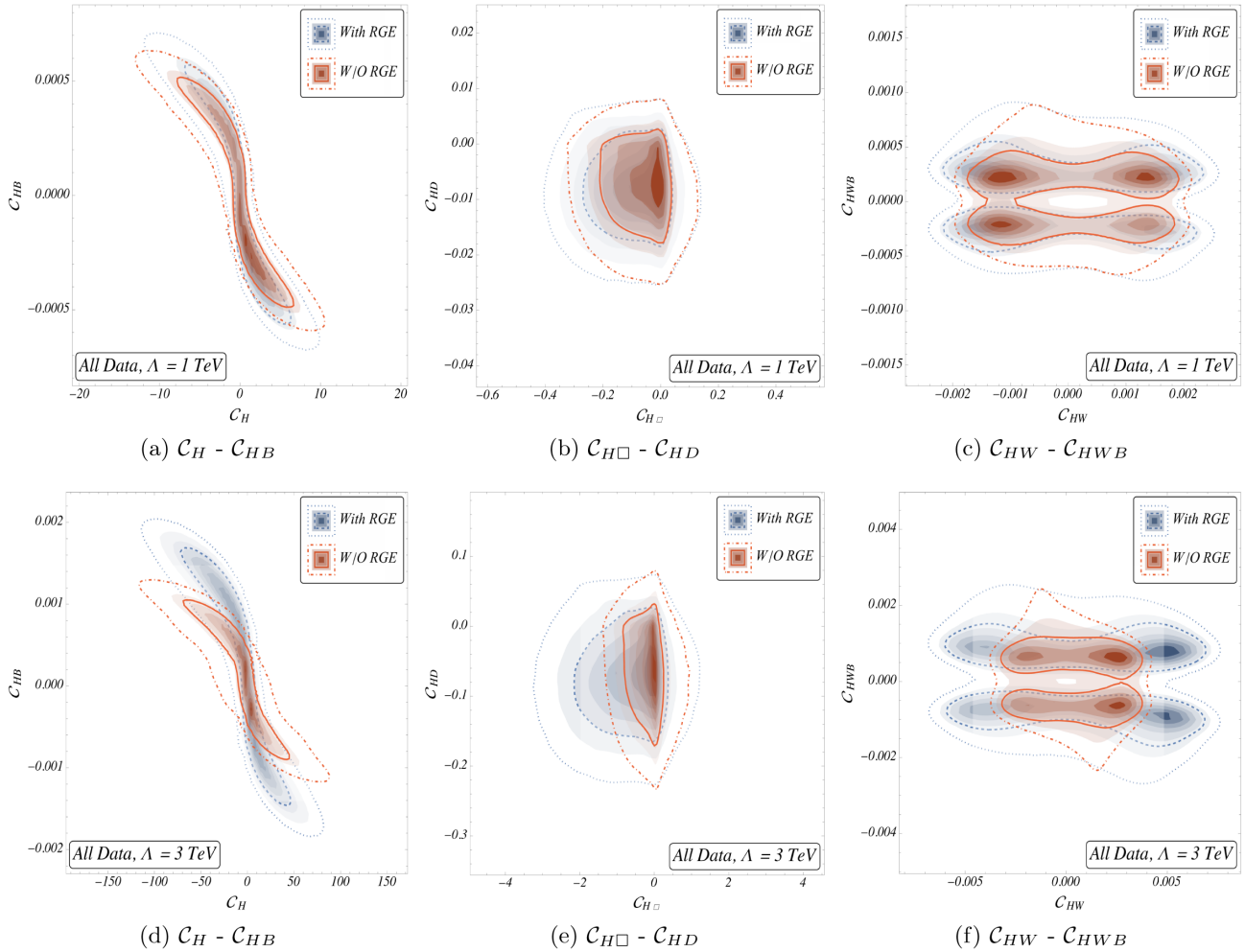

(a) $\mathcal{C}_H$ - $\mathcal{C}_{HB}$ (b) $\mathcal{C}_{H\Box}$ - $\mathcal{C}_{HD}$ (c) $\mathcal{C}_{HW}$ - $\mathcal{C}_{HWB}$

(d) $\mathcal{C}_H$ - $\mathcal{C}_{HB}$ (e) $\mathcal{C}_{H\Box}$ - $\mathcal{C}_{HD}$ (f) $\mathcal{C}_{HW}$ - $\mathcal{C}_{HWB}$

FIG. 9. Two-dimensional posteriors among the WCs induced by $\mathcal{H}_2$ for $m_{\mathcal{H}_2} = 1$ TeV [panels (a)–(c)] and $m_{\mathcal{H}_2} = 3$ TeV [panels (d)–(f)]. Similar to Fig. 8, the credible regions shown in red and blue correspond to scenarios without and with RGE, respectively.

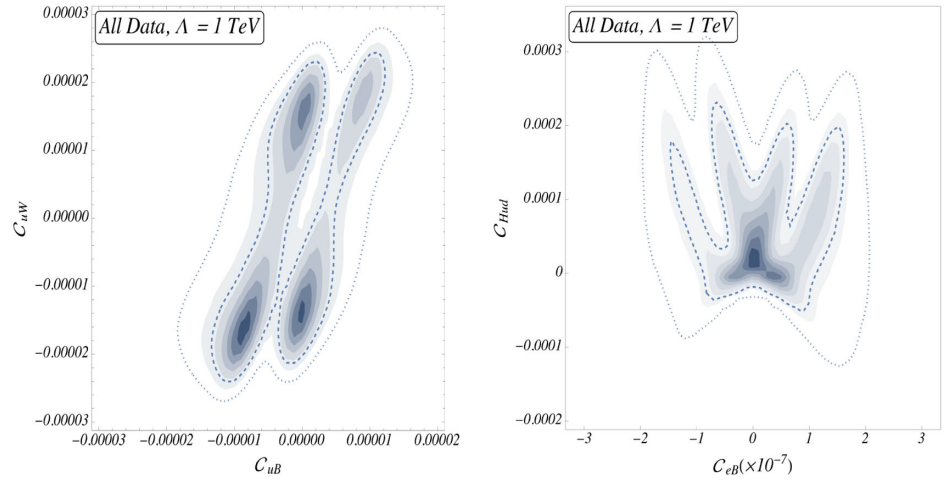

(a) $\mathcal{C}_{uB}$ - $\mathcal{C}_{uW}$ (b) $\mathcal{C}_{eB}$ - $\mathcal{C}_{Hud}$

FIG. 10. (a) and (b) Two-dimensional marginalized WCs posterior for $m_{\mathcal{H}_2}$ $(\Lambda) = 1$ TeV with RG-evolved matching results.

suppression of $1/16\pi^2$. The effect of this small factor is visible in the strictly constrained WC space.

VII. CONCLUSIONS

In this paper we analyzed and constrained potential directions of BSM physics under two themes: in a model-independent way using dimension-six SMEFT, and for 16 single-scalar-particle extensions of the SM using a similar statistical methodology and data sets.

We performed a global analysis of 23 Wilson coefficients in the Warsaw basis based on an up-to-date set of observables of the Higgs and diboson sectors plus EWPOs. Our fit includes di-Higgs measurements for the first time which improves the bounds on a modified Higgs potential through $\mathcal{C}_H$. The addition of recent data sets, and in particular STXS data up to high energies, strengthens the limits on the Wilson coefficients by up to a factor of 9 compared to previous analyses. The biggest improvements are obtained for operators describing Higgs-top and Higgs-gluon interactions as well as for $\mathcal{C}_{H\Box}$. We analyzed in detail the role of different STXS measurements in constraining the different Wilson coefficients.

Moreover, we tabulated the complete sets of dimension-six effective operators and the associated WCs in the Warsaw basis after integrating out the single heavy non-SM scalars for 16 different NP scenarios up to the one-loop level incorporating the scalar heavy-light mixing contributions from the loops. The WCs are expressed in terms of the model parameters. We employed a similar analysis strategy for each of the BSM scenarios and constrained the model parameters. We highlighted the individual impact of different observables (EWPO and Higgs data) through two-dimensional posteriors in the model-parameter and WC planes. We explicitly discussed the results for the EWDS $\mathcal{H}_2$ and a scalar leptoquark extension Θ_1. Plots for the remaining 14 models considered are available in the Supplemental material [187].[8]

We investigated the effects of RG running on the allowed space of the model parameters and the WCs for two choices of the cutoff scale (1 and 3 TeV). We performed the RG running (in the leading-log approximation) on the matching results for an extra electroweak scalar doublet model for two different cutoff scales (1 and 3 TeV). We noted that once the RG effects are taken into consideration, the allowed ranges of BSM parameters are relaxed compared to the no-RG case. We also displayed the allowed ranges of WCs associated with the radiatively generated effective operators.

Currently, the considered data set leaves some of the effective operators that arise from the single-scalar extensions studied unconstrained and therefore fails to encapsulate the impact of all NP interactions. Specifically, this concerns the WCs associated with four-fermion operators. Looking ahead, we are planning to add observables constraining four-fermion operators [182], e.g., from dilepton production, parity violation, and low-energy flavor observables, to constrain so-far unbound directions in parameter space. These would be particularly relevant for constraining leptoquark models [188].

ACKNOWLEDGMENTS

We thank Julien Baglio, Silvia Ferrario Ravasio, Stephen Jones, Ken Mimasu, and Tevong You for helpful discussions, and Ennio Salvioni, Gauthier Durieux, and Matthew McCullough for pointing out an error in a matching result of the quartet model (Σ). The work of A., S. D. B., and J. C. is supported by the Science and Engineering Research Board, Government of India, under the agreements SERB/PHY/2019501. S. D. B. is also supported in part by SRA

[8]These plots can also be downloaded from the GitHub repository [172].

(Spain) under Grant No. PID2019–106087 GB-C21/10.13039/501100011033, and by the Junta de Andaluca (Spain) under Grants No. FQM-101, A-FQM-467-UGR18, PID2021-128396NB-100, and P18-FR-4314 (FEDER). M. S. is supported by the STFC under Grant No. ST/P001246/1. A. B. gratefully acknowledges support from the Alexander-von-Humboldt foundation as a Feodor Lynen Fellow. We thank the IPPP for access to its computing cluster.

APPENDIX A: FUNCTIONAL MATCHING USING CODEX

CoDEx uses effective action formulas to compute one-loop-level WCs, which involves solving the functional "Trace—Log" of UV action derivatives. We follow the procedures in Ref. [103] (for loops with only heavy field propagators) and Refs. [106,108] for the derivation and cross-checks of heavy-light mixed one-loop effective action formulas, which CoDEx solves for each BSM. Note that there is more than one procedure to calculate the effective action formulas [103,104,107,108]. However, readers are welcome to study all of them as each method has its own advantages. It is worth mentioning that in this work we calculate matching of BSM scenarios with s single heavy scalar extension of the SM particle content, and therefore the functional traces have a relatively simple form, which is not the case in most generic scenarios assuming an arbitrary number of heavy fields with nondegenerate masses and arbitrary spins [112,189,190].

In the following, we elaborate on the implementation of effective action formulas for BSM scenarios to integrate out the heavy field up to one loop. The effective action $S_{\rm eff}[\phi]$ is defined as

$$e^{iS_{\rm eff}[\phi](\mu)} = \int \mathcal{D}\Phi e^{iS_{\rm UV}[\phi,\Phi](\mu)}, \tag{A1}$$

where Φ and ϕ are a heavy real scalar and a light field, respectively, and $S_{\rm UV}[\phi,\Phi](\mu)$ represents the UV action defined at the scale μ. In the following discussion, we set μ equal to the cutoff scale Λ, which is also the matching scale of the UV theory to the EFT. We expand the UV action around the classical configuration of the heavy field Φ_c defined by

$$\left.\frac{\delta S_{\rm UV}[\phi,\Phi]}{\delta\Phi}\right|_{\Phi_c} = 0. \tag{A2}$$

Now, $S_{\rm UV}[\phi,\Phi] \to S_{\rm UV}[\phi,\Phi_c+\eta]$ in Eq. (A1), where η represents the fluctuation field defined as $\Phi = \Phi_c + \eta$. Using Eq. (A2), we have

$$S_{\rm eff}[\phi] = S_{\rm UV}[\phi,\Phi_c] + \frac{i}{2}\mathrm{TrLog}\left[-\left.\frac{\delta^2 S_{\rm UV}[\phi,\Phi]}{\delta\Phi^2}\right|_{\Phi_c}\right] + \mathcal{O}(\eta^2). \tag{A3}$$

In Eq. (A3) we recognize the first and second terms on the rhs as the tree-level and pure heavy-loop processes in the effective action, respectively. Similarly, we can capture the contribution from the mixed heavy-light loop processes by expanding the UV action around the classical configuration of the light field(s), which we discuss in detail later in this section. One can determine the classical configuration of the heavy field by using the Euler-Lagrange equation on the UV Lagrangian $\mathcal{L}_{\rm UV}$. Then, substituting the heavy field solution back into the UV Lagrangian leads to tree-level matching. Subsequently, by imposing a mass-dimension cutoff and SM field equation of motion, Fierz identities, and integration-by-parts relations, one gets the Wilson coefficients of effective operators of a given mass dimension.

1. One-loop matching: only heavy fields as loop propagators

The functional "Trace—Log" of the action derivatives can be expanded in terms of covariant derivatives, the quadratic matrix "U," and the heavy field mass. The quadratic matrix "U" contains the interaction of heavy fields and light fields. We define

$$S_{\rm eff}^{\rm 1loop(H)}(\phi) = \frac{i}{2}\mathrm{Tr}\log\left[-\left.\frac{\delta^2 S_{\rm UV}[\phi,\Phi]}{\delta\Phi^2}\right|_{\Phi_c}\right] = ic_s \mathrm{Tr}\log\left[-P^2 + M^2 + U(\phi)\right]. \tag{A4}$$

Here M is the mass of the heavy field Φ. c_s takes the numerical values $+\frac{1}{2}$ and $+1$ for real and complex scalars, respectively. Now, by expanding the functional trace by inserting a complete set of momentum and spatial states, and applying the Baker-Campbell-Hausdorff formula [103], we get

$$S_{\rm eff}^{\rm 1loop(H)}(\phi) = ic_s \int d^4x \int \frac{d^4k}{(2\pi)^4}\mathrm{tr}\log\left[-\left(k_\mu + \tilde{G}_{\nu\mu}\frac{\partial}{\partial k_\nu}\right)^2 + M^2 + \tilde{U}(\phi)\right], \tag{A5}$$

where

$$\tilde{G}_{\nu\mu} = -\sum_{n=0}^{\infty}\frac{n+1}{(n+2)!}[P_{\alpha_1},\ldots,[P_{\alpha_n},[P_\nu,P_\mu]]]\frac{\partial^n}{\partial k_{\alpha_1}\ldots\partial k_{\alpha_n}}, \tag{A6}$$

and

$$\tilde{U} = \sum_{n=0}^{\infty}\frac{1}{n!}[P_{\alpha_1},\ldots,[P_{\alpha_n},U]]\frac{\partial^n}{\partial k_{\alpha_1}\ldots\partial k_{\alpha_n}}. \tag{A7}$$

This transformation puts all of the covariant derivatives in commutators, and thus the resulting effective operators are manifestly gauge invariant. Now, we expand the argument of "log" and replace it by an integral (on M^2),

$$S_{\rm eff}^{\rm 1loop(H)}(\phi) = -ic_s \int d^4x \int \frac{d^4k}{(2\pi)^4} \int dM^2 \mathrm{tr}\left[\Delta_F\left[1 + \Delta_F\left(\left\{k_\mu, \tilde{G}_{\nu\mu}\frac{\partial}{\partial k_\nu}\right\} + \tilde{G}_{\sigma\mu}\tilde{G}^{\sigma}_{\nu}\frac{\partial}{\partial k_\mu}\frac{\partial}{\partial k_\nu} - \tilde{U}\right)\right]\right]^{-1}, \quad \text{(A8)}$$

where $\Delta_F = \frac{1}{k^2 - M^2}$. The above equation is the master formula for gauge-invariant effective operators up to an arbitrary mass dimension. In order to truncate at dimension six, we expand the argument of "tr" and replace the momentum integrals in terms of the heavy field mass. Then, the effective action formula for loops containing only heavy field propagators up to mass-dimension six is given by

$$\begin{aligned}\mathcal{L}_{\rm 1-loop}^{(\dim-6)}[\phi] = \frac{c_s}{(4\pi)^2}\mathrm{tr}\Bigg\{ & M^2 U + \frac{1}{M^2}\left[-\frac{1}{60}(P_\mu G'_{\mu\nu})^2 - \frac{1}{90}G'_{\mu\nu}G'_{\nu\sigma}G'_{\sigma\mu} - \frac{1}{12}(P_\mu U)^2 - \frac{1}{6}U^3 - \frac{1}{12}UG'_{\mu\nu}G'_{\mu\nu}\right] \\ & + \frac{1}{M^4}\left[\frac{1}{24}U^4 + \frac{1}{12}U(P_\mu U)^2 + \frac{1}{120}(P^2U)^2 + \frac{1}{24}(U^2G'_{\mu\nu}G'_{\mu\nu}) - \frac{1}{120}[(P_\mu U),(P_\nu U)]G'_{\mu\nu}\right. \\ & \left. - \frac{1}{120}[U[U,G'_{\mu\nu}]]G'_{\mu\nu}\right] + \frac{1}{M^6}\left[-\frac{1}{60}U^5 - \frac{1}{20}U^2(P_\mu U)^2 - \frac{1}{30}(UP_\mu U)^2\right] + \frac{1}{M^8}\left[\frac{1}{120}U^6\right]\Bigg\}. \end{aligned} \quad \text{(A9)}$$

Here, $P_\mu = iD_\mu$ and $G'_{\mu\nu} = [D_\mu, D_\nu]$. It is important to note that "tr" in the above equation is the trace performed over the internal symmetry indices. Note that the loop-level WCs are renormalization scheme dependent and are defined in the $\overline{\rm MS}$ scheme.

CoDEx builds the covariant derivative operator for the heavy field from its SM quantum numbers, and constructs "U" from interactions present in the UV Lagrangian. Then, the field-strength tensors in "$G'_{\mu\nu}$" are defined from the covariant derivative. For cases where the heavy field transforms under both color and isospin groups, "U" would contain two pairs of indices, one each for the $SU(3)_C$ and $SU(2)_L$ spaces of the field multiplet. Using all of this information, the package evaluates the trace in Eq. (A9) and gets the effective Lagrangian in an off-shell basis, which is reduced to the Warsaw (or other user-defined on-shell) basis using on-shell relations.

2. One-loop matching: heavy-light loops

The mixed heavy-light contribution is derived by expanding the UV action around the classical configuration of light fields, similar to the pure heavy-loop approach. The one-loop effective action $\Delta S_{\rm eff}^{\rm 1-loop}$ is defined as

$$\Delta S_{\rm eff}^{\rm 1-loop}[\phi,\Phi_c] = \frac{i}{2}\mathrm{Tr}\log\left[-\frac{\delta^2 S_{\rm UV}[\phi,\Phi]}{\delta(\phi,\Phi)^2}\bigg|_{\Phi=\Phi_c(\phi)}\right], \quad \text{(A10)}$$

and we define

$$Q_{\rm UV}[\phi,\Phi] \equiv -\frac{\delta^2 S_{\rm UV}[\phi,\Phi]}{\delta(\phi,\Phi)^2}. \quad \text{(A11)}$$

This contains quantum corrections from both heavy and light fields. First, we block diagonalize the quadratic matrix $Q_{\rm UV}$, which is a square matrix in the field space. We define the Δ's following Eq. (A11),

$$\begin{aligned} Q_{\rm UV}[\phi,\Phi] &= \begin{pmatrix} \Delta_{\rm H} & \Delta_{\rm HL} \\ \Delta_{\rm LH} & \Delta_{\rm L} \end{pmatrix} \\ &\equiv \begin{pmatrix} -\frac{\delta^2 S_{\rm UV}[\phi,\Phi]}{\delta\Phi^2} & -\frac{\delta^2 S_{\rm UV}[\phi,\Phi]}{\delta\Phi\delta\phi} \\ -\frac{\delta^2 S_{\rm UV}[\phi,\Phi]}{\delta\phi\delta\Phi} & -\frac{\delta^2 S_{\rm UV}[\phi,\Phi]}{\delta\phi^2} \end{pmatrix}. \end{aligned} \quad \text{(A12)}$$

Then, we define

$$\begin{aligned} V &= \begin{pmatrix} \mathbb{1} & \mathbb{0} \\ -\Delta_{\rm L}^{-1}\Delta_{\rm LH} & \mathbb{1} \end{pmatrix} \\ \Rightarrow V^\dagger Q_{\rm UV} V &= \begin{pmatrix} \Delta_{\rm H} - \Delta_{\rm HL}\Delta_{\rm L}^{-1}\Delta_{\rm LH} & \mathbb{0} \\ \mathbb{0} & \Delta_{\rm L} \end{pmatrix}. \end{aligned} \quad \text{(A13)}$$

We then use the distributive property of determinants,

$$\begin{aligned} &\Delta S_{\rm eff}^{\rm 1-loop}[\phi,\Phi_c] \\ &= \left(\frac{i}{2}\mathrm{Tr}\log\left[\Delta_{\rm H} - \Delta_{\rm HL}\Delta_{\rm L}^{-1}\Delta_{\rm LH}\right] + \frac{i}{2}\mathrm{Tr}\log[\Delta_{\rm L}]\right)\bigg|_{\Phi=\Phi_c}. \end{aligned} \quad \text{(A14)}$$

Now we define the Δ's from the UV Lagrangian $S_{\rm UV}$ in terms of the kinetic and interaction terms,

$$\begin{aligned} S_{\rm UV}[\phi,\Phi] &= \int d^4x \mathcal{L}_{\rm UV}[\phi,\Phi] \\ \Rightarrow -\Delta_{\rm H} &= \frac{\delta^2 S_{\rm UV}[\phi,\Phi]}{\delta\Phi^2} = \int d^4x \frac{\delta^2 \mathcal{L}_{\rm UV}[\phi,\Phi]}{\delta\Phi^2} \\ &= \int d^4x (\mathcal{P}^2 - M^2 + U_{\rm H}), \end{aligned} \quad \text{(A15)}$$

where $\mathcal{P}_\mu \equiv i\mathcal{D}_\mu$, and M^2 is the squared mass matrix of Φ. $U_{\rm H}$ accommodates the light-field and self-interaction terms of Φ in the UV Lagrangian. Similarly,

$$-\Delta_{\rm L} = \frac{\delta^2 S_{\rm UV}[\phi,\Phi]}{\delta\phi^2} = \int d^4x \frac{\delta^2 \mathcal{L}_{\rm UV}[\phi,\Phi]}{\delta\phi^2} = \int d^4x(\mathcal{P}^2 - m^2 + U_{\rm L}), \tag{A16}$$

where m is the mass of ϕ. $U_{\rm L}$ carries the heavy-field and self-interaction terms of the light field. The off-diagonal elements of $Q_{\rm UV}$ are defined as

$$-\Delta_{\rm HL} = \frac{\delta^2 S_{\rm UV}[\phi,\Phi]}{\delta\Phi\delta\phi} = \int d^4x \frac{\delta^2 \mathcal{L}_{\rm UV}[\phi,\Phi]}{\delta\Phi\delta\phi} = \int d^4x U_{\rm HL} \tag{A17}$$

and

$$-\Delta_{\rm LH} = \frac{\delta^2 S_{\rm UV}[\phi,\Phi]}{\delta\phi\delta\Phi} = \int d^4x \frac{\delta^2 \mathcal{L}_{\rm UV}[\phi,\Phi]}{\delta\phi\delta\Phi} = \int d^4x U_{\rm LH}. \tag{A18}$$

$U_{\rm HL}$ and $U_{\rm LH}$ carry the interactions between heavy Φ and light ϕ fields. Now, we have defined the rhs of Eq. (A14) completely in terms of interactions present in the Lagrangian. Then, the next step is to extract the heavy-light mixed-loop contribution from the rhs. We proceed by implementing the matching condition of a UV theory and its EFT:

$$\Gamma_{\rm L,UV}[\phi] = \Gamma_{\rm EFT}[\phi], \tag{A19}$$

where $\Gamma_{\rm L,UV}[\phi]$ is the one-light-particle-irreducible effective action calculated in the UV theory, and $\Gamma_{\rm EFT}[\phi]$ is the one-particle-irreducible effective action calculated in the EFT. This matching condition is imposed order by order in the perturbation. At one-loop order in the UV theory,

$$\Gamma^{1-\rm loop}_{\rm L,UV}[\phi] = \Delta S^{1-\rm loop}_{\rm eff}[\phi,\Phi_c] = \frac{i}{2}\mathrm{Tr}\log[Q_{\rm UV}[\phi,\Phi]|_{\Phi=\Phi_c}], \tag{A20}$$

whereas at one-loop order in the EFT,

$$\Gamma^{1-\rm loop}_{\rm EFT}[\phi] = \int d^4x \mathcal{L}^{1-\rm loop}_{\rm EFT}[\phi] + \frac{i}{2}\mathrm{Tr}\log\left[-\frac{\delta^2 \mathcal{S}_{\rm EFT}[\phi]}{\delta\phi^2}\right], \tag{A21}$$

where

$$S_{\rm EFT}[\phi] \equiv S_{\rm UV}[\phi,\Phi_c] = S_{\rm UV}[\phi,\Phi]|_{\Phi=\Phi_c(\phi)}. \tag{A22}$$

The one-loop effective action in the EFT contains contributions from (a) one-loop generated operators contributing at tree level, and (b) tree-level operators inserted at one loop. The rhs of Eq. (A21) contains these two contributions. Substituting Eqs. (A20) and (A21) into Eq. (A19), we get

$$\begin{aligned}&\frac{i}{2}\mathrm{Tr}\log[Q_{\rm UV}[\phi,\Phi]|_{\Phi=\Phi_c}] \\ &= \int d^4x \mathcal{L}^{1-\rm loop}_{\rm EFT}[\phi] + \frac{i}{2}\mathrm{Tr}\log\left[-\frac{\delta^2 \mathcal{S}_{\rm EFT}[\phi]}{\delta\phi^2}\right] \\ &\Rightarrow \int d^4x \mathcal{L}^{1-\rm loop}_{\rm EFT}[\phi] = \frac{i}{2}\mathrm{Tr}\log[Q_{\rm UV}[\phi,\Phi]|_{\Phi=\Phi_c}] \\ &\quad - \frac{i}{2}\mathrm{Tr}\log\left[-\frac{\delta^2 \mathcal{S}_{\rm EFT}[\phi]}{\delta\phi^2}\right].\end{aligned} \tag{A23}$$

Now, we solve the second term on the rhs of Eq. (A23),

$$\begin{aligned}-\frac{\delta^2 \mathcal{S}_{\rm EFT}[\phi]}{\delta\phi^2} &= -\frac{\delta^2}{\delta\phi^2}(S_{\rm UV}[\phi,\Phi]|_{\Phi=\Phi_c}) \\ &= -\frac{\delta}{\delta\phi}\left\{\left(\frac{\delta S_{\rm UV}[\phi,\Phi]}{\delta\phi} + \frac{\delta\Phi}{\delta\phi}\frac{\delta S_{\rm UV}[\phi,\Phi]}{\delta\Phi}\right)\Big|_{\Phi=\Phi_c}\right\} \\ &= -\frac{\delta}{\delta\phi}\left(\frac{\delta S_{\rm UV}[\phi,\Phi]}{\delta\phi}\Big|_{\Phi=\Phi_c}\right) \\ &= \left(-\frac{\delta^2 S_{\rm UV}[\phi,\Phi]}{\delta\phi^2} - \frac{\delta\Phi}{\delta\phi}\frac{\delta^2 S_{\rm UV}[\phi,\Phi]}{\delta\Phi\delta\phi}\right)\Big|_{\Phi=\Phi_c} \\ &= (\Delta_{\rm L} - \Delta_{\rm LH}\hat{\Delta}^{-1}_{\rm H}\Delta_{\rm HL})|_{\Phi=\Phi_c}.\end{aligned} \tag{A24}$$

We used the definition of Φ_c in the first line to obtain the second line, and in the second line we used

$$\begin{aligned}&\frac{\delta}{\delta\phi}\left(\frac{\delta S_{\rm UV}[\phi,\Phi]}{\delta\Phi}\Big|_{\Phi=\Phi_c}\right) = 0 \\ &\Rightarrow \left(\frac{\delta^2 S_{\rm UV}[\phi,\Phi]}{\delta\phi\delta\Phi} + \frac{\delta\Phi}{\delta\phi}\frac{\delta^2 S_{\rm UV}[\phi,\Phi]}{\delta\Phi^2}\right)\Big|_{\Phi=\Phi_c} = 0 \\ &\Rightarrow \left(\frac{\delta\Phi}{\delta\phi}\Delta_{\rm H}\right)\Big|_{\Phi=\Phi_c} = (-\Delta_{\rm LH})|_{\Phi=\Phi_c} \\ &\Rightarrow \left(\frac{\delta\Phi}{\delta\phi}\right)\Big|_{\Phi=\Phi_c} = (-\Delta_{\rm LH})|_{\Phi=\Phi_c}(\Delta_{\rm H}|_{\Phi=\Phi_c})^{-1}\end{aligned} \tag{A25}$$

to arrive at the third line of Eq. (A23). The hat is put on $\Delta_{\rm H}$ to indicate that it is a local operator in the EFT. We rewrite Eq. (A23),

$$\int d^4x\mathcal{L}_{\rm EFT}^{\rm 1-loop}[\phi] = \left(\frac{i}{2}\mathrm{Tr}\log\left[\Delta_{\rm H}-\Delta_{\rm HL}\Delta_{\rm L}^{-1}\Delta_{\rm LH}\right]+\frac{i}{2}\mathrm{Tr}\log[\Delta_{\rm L}]-\frac{i}{2}\mathrm{Tr}\log\left[\Delta_{\rm L}-\Delta_{\rm LH}\hat{\Delta}_{\rm H}^{-1}\Delta_{\rm HL}\right]\right)\Big|_{\Phi=\Phi_c}$$
$$= \left(\frac{i}{2}\mathrm{Tr}\log\left[\Delta_{\rm H}-\Delta_{\rm HL}\Delta_{\rm L}^{-1}\Delta_{\rm LH}\right]+\frac{i}{2}\mathrm{Tr}\log[\Delta_{\rm L}]-\frac{i}{2}\mathrm{Tr}\log[\Delta_{\rm L}]-\frac{i}{2}\mathrm{Tr}\log\left[\mathbb{1}-\Delta_{\rm L}^{-1}\Delta_{\rm LH}\hat{\Delta}_{\rm H}^{-1}\Delta_{\rm HL}\right]\right)\Big|_{\Phi=\Phi_c}$$
$$= \left(\frac{i}{2}\mathrm{Tr}\log\left[\Delta_{\rm H}-\Delta_{\rm HL}\Delta_{\rm L}^{-1}\Delta_{\rm LH}\right]-\frac{i}{2}\mathrm{Tr}\log\left[\mathbb{1}-\Delta_{\rm L}^{-1}\Delta_{\rm LH}\hat{\Delta}_{\rm H}^{-1}\Delta_{\rm HL}\right]\right)\Big|_{\Phi=\Phi_c}. \tag{A26}$$

The contribution from loops with light propagators only ($\mathrm{Tr}\log[\Delta_{\rm L}]$) cancels while matching the UV theory to its EFT, as expected. We use Sylvester's determinant identity on the second term to further reduce it,

$$\left(\frac{i}{2}\mathrm{Tr}\log\left[\Delta_{\rm H}-\Delta_{\rm HL}\Delta_{\rm L}^{-1}\Delta_{\rm LH}\right]-\frac{i}{2}\mathrm{Tr}\log\left[\hat{\Delta}_{\rm H}-\Delta_{\rm HL}\Delta_{\rm L}^{-1}\Delta_{\rm LH}\right]+\frac{i}{2}\mathrm{Tr}\log[\hat{\Delta}_{\rm H}]\right)\Big|_{\Phi=\Phi_c} = \int d^4x\mathcal{L}_{\rm EFT}^{\rm 1-loop}[\phi]. \tag{A27}$$

Now, we have the contributions from both the heavy-light mixed loops and loops containing only heavy-field propagators. One may cross-check the rhs by substituting $\Delta_{\rm L}=\Delta_{\rm HL}=\Delta_{\rm LH}=0$ and check that we get $(\frac{i}{2}\mathrm{Tr}\log[\Delta_{\rm H}])|_{\Phi=\Phi_c}$, which contains loops with heavy-field propagators only. The next step is to expand the rhs of Eq. (A27) in terms of the covariant derivative operator, mass matrices, and the quadratic matrix U, with the goal of constructing a one-loop effective action formula. We use the key observation made in Ref. [107] that the effective action can be split into "hard" and "soft" regions, and these regions produce the IR- and UV-divergent integrals, respectively. The hard region is captured when the loop integral is calculated in the limit $M^2 \gg m^2$. So, we solve

$$\int d^4x\mathcal{L}_{\rm EFT}^{\rm 1-loop}[\phi] = \frac{i}{2}\mathrm{Tr}\log[\Delta_{\rm H}-\Delta_{\rm HL}\Delta_{\rm L}^{-1}\Delta_{\rm LH}]\big|_{\rm hard} = \frac{i}{2}\int\frac{d^dq}{(2\pi)^d}\mathrm{tr}\log[\Delta_{\rm H}-\Delta_{\rm HL}\Delta_{\rm L}^{-1}\Delta_{\rm LH}]\Big|_{\rm hard}$$
$$= \frac{i}{2}\int\frac{d^dq}{(2\pi)^d}\mathrm{tr}\log[-(P^2-2P.q+q^2)+M^2+U_{\rm H}-\Delta_{\rm HL}\Delta_{\rm L}^{-1}\Delta_{\rm LH}]\Big|_{\rm hard}$$
$$= -\frac{i}{2}\sum_{n=1}^{\infty}\frac{1}{n}\int\frac{d^dq}{(2\pi)^d}\mathrm{tr}\log[(q^2-m^2)^{-1}$$
$$\times\{-P^2+2P\cdot q+U_{\rm H}|_{P\to P-q}-\Delta_{\rm HL}\Delta_{\rm L}^{-1}\Delta_{\rm LH}|_{P\to P-q}\}]^n\Big|_{\rm hard}. \tag{A28}$$

The last equality is true up to an additive constant because we factored out (q^2-M^2) and implemented the logarithmic expansion in the last step. Here, we expand the sum and keep terms encompassing all of the dimension-six (and lower) effective operators. To reduce these further, we follow the method of covariant diagrams as in Ref. [108] to arrive at the master formulas. The master trace formulas and their corresponding integration factors are listed in Tables V–VIII. These formulas apply to two types of BSM scenarios, where the SM is extended by: (i) a single heavy field, and (ii) multiple mass-degenerate heavy fields. We compare these with that presented in Ref. [109] for mass-degenerate cases and find complete agreement.

TABLE V. Effective action formulas with only U's. See Table IX for integration factors. The formula terms listed here, similar to the pure-heavy-loop effective action, are calculated using dimensional regularization and in the $\overline{\rm MS}$ scheme. Here the matching scale is set equal to the heavy-field mass.

Factors	Formulas
$-ic_s\mathcal{I}^{11}$	$\mathrm{tr}(U_{HL}U_{LH})$
$-ic_s\mathcal{I}^{21}$	$\mathrm{tr}(U_HU_{HL}U_{LH})$
$-ic_s\mathcal{I}^{31}$	$\mathrm{tr}(U_HU_HU_{HL}U_{LH})$
$-ic_s\mathcal{I}^{41}$	$\mathrm{tr}(U_HU_HU_HU_{HL}U_{LH})$
$-ic_s\mathcal{I}^{51}$	$\mathrm{tr}(U_HU_HU_HU_HU_{HL}U_{LH})$
$-ic_s\mathcal{I}^{12}$	$\mathrm{tr}(U_{HL}U_LU_{LH})$
$-ic_s\mathcal{I}^{22}$	$\mathrm{tr}(U_HU_{HL}U_LU_{LH})$
$-ic_s\mathcal{I}^{32}$	$\mathrm{tr}(U_HU_HU_{HL}U_LU_{LH})$
$-ic_s\mathcal{I}^{42}$	$\mathrm{tr}(U_HU_HU_HU_{HL}U_LU_{LH})$

(Table continued)

TABLE V. *(Continued)*

Factors	Formulas
$-ic_s\mathcal{I}^{13}$	$\mathrm{tr}(U_{HL}U_LU_LU_{LH})$
$-ic_s\mathcal{I}^{23}$	$\mathrm{tr}(U_HU_{HL}U_LU_LU_{LH})$
$-ic_s\mathcal{I}^{33}$	$\mathrm{tr}(U_HU_HU_{HL}U_LU_LU_{LH})$
$-ic_s\mathcal{I}^{14}$	$\mathrm{tr}(U_{HL}U_LU_LU_LU_{LH})$
$-ic_s\mathcal{I}^{24}$	$\mathrm{tr}(U_HU_{HL}U_LU_LU_LU_{LH})$
$-ic_s\mathcal{I}^{15}$	$\mathrm{tr}(U_{HL}U_LU_LU_LU_LU_{LH})$
$-ic_s\frac{1}{2}\mathcal{I}^{22}$	$\mathrm{tr}(U_{HL}U_{LH}U_{HL}U_{LH})$
$-ic_s\mathcal{I}^{32}$	$\mathrm{tr}(U_HU_{HL}U_{LH}U_{HL}U_{LH})$
$-ic_s\frac{1}{2}\mathcal{I}^{42}$	$\mathrm{tr}(U_HU_{HL}U_{LH}U_HU_{HL}U_{LH})$
$-ic_s\mathcal{I}^{42}$	$\mathrm{tr}(U_HU_HU_{HL}U_{LH}U_{HL}U_{LH})$
$-ic_s\mathcal{I}^{23}$	$\mathrm{tr}(U_{HL}U_{LH}U_{HL}U_LU_{LH})$
$-ic_s\mathcal{I}^{33}$	$\mathrm{tr}(U_HU_{HL}U_{LH}U_{HL}U_LU_{LH})$
$-ic_s\mathcal{I}^{33}$	$\mathrm{tr}(U_HU_{HL}U_LU_{LH}U_{HL}U_{LH})$
$-ic_s\frac{1}{2}\mathcal{I}^{24}$	$\mathrm{tr}(U_{HL}U_LU_{LH}U_{HL}U_LU_{LH})$
$-ic_s\mathcal{I}^{24}$	$\mathrm{tr}(U_{HL}U_{LH}U_{HL}U_LU_LU_{LH})$
$-ic_s\frac{1}{3}\mathcal{I}^{33}$	$\mathrm{tr}(U_{HL}U_{LH}U_{HL}U_{LH}U_{HL}U_{LH})$

TABLE VI. Effective action formulas with two P's (Part I).

Factors	Formulas
$f^2_{PU} = -ic_s2\mathcal{I}[q^2]^{22}$	$\mathrm{tr}([\mathcal{P}_\mu, U_{HL}][\mathcal{P}^\mu, U_{LH}])$
$f^{3(H)}_{PU,a} = -ic_s2(\mathcal{I}[q^2]^{32} + \mathcal{I}[q^2]^{41})$	$\mathrm{tr}([\mathcal{P}_\mu, U_H][\mathcal{P}^\mu, U_{HL}]U_{LH})$
$f^{3(H)}_{PU,b} = -ic_s2(\mathcal{I}[q^2]^{32} + \mathcal{I}[q^2]^{41})$	$\mathrm{tr}([\mathcal{P}_\mu, U_H]U_{HL}[\mathcal{P}^\mu, U_{LH}])$
$f^{3(H)}_{PU,c} = -ic_s4\mathcal{I}[q^2]^{32}$	$\mathrm{tr}(U_H[\mathcal{P}_\mu, U_{HL}][\mathcal{P}_\mu, U_{LH}])$
$f^{3(L)}_{PU,a} = -ic_s2(\mathcal{I}[q^2]^{14} + \mathcal{I}[q^2]^{23})$	$\mathrm{tr}([\mathcal{P}_\mu, U_{HL}][\mathcal{P}^\mu, U_L]U_{LH})$
$f^{3(L)}_{PU,b} = -ic_s4\mathcal{I}[q^2]^{23}$	$\mathrm{tr}([\mathcal{P}_\mu, U_{HL}]U_L[\mathcal{P}^\mu, U_{LH}])$
$f^{3(L)}_{PU,c} = -ic_s2(\mathcal{I}[q^2]^{14} + \mathcal{I}[q^2]^{23})$	$\mathrm{tr}(U_{HL}[\mathcal{P}_\mu, U_L][\mathcal{P}^\mu, U_{LH}])$

TABLE VII. Effective action formulas with four P's.

Factors	Formulas
$f^2_{PPU,a} = -ic_s4(\mathcal{I}[q^4]^{33} + 2\mathcal{I}[q^4]^{42} + 2\mathcal{I}[q^4]^{51})$	$\mathrm{tr}(G'_{\mu\nu}G'^{\mu\nu}U_{HL}U_{LH})$
$f^2_{PPU,b} = -ic_s4(\mathcal{I}[q^4]^{33} + 2\mathcal{I}[q^4]^{24} + 2\mathcal{I}[q^4]^{15})$	$\mathrm{tr}(G'_{\mu\nu}G'^{\mu\nu}U_{LH}U_{HL})$
$f^2_{PPU,c} = -ic_s8\mathcal{I}[q^4]^{33}$	$\mathrm{tr}(G'_{\nu\mu}[\mathcal{P}^\mu, U_{HL}][\mathcal{P}^\nu, U_{LH}])$
$f^2_{PPU,d} = -ic_s8\mathcal{I}[q^4]^{33}$	$\mathrm{tr}(G'_{\nu\mu}[\mathcal{P}^\mu, U_{LH}][\mathcal{P}^\nu, U_{HL}])$
$f^2_{PPU,e} = -ic_s8\mathcal{I}[q^4]^{33}$	$\mathrm{tr}([\mathcal{P}_\mu, [\mathcal{P}_\mu, U_{HL}]][\mathcal{P}^\nu, [\mathcal{P}^\nu, U_{LH}]])$
$f^2_{PPU,f} = -ic_s4(\mathcal{I}[q^4]^{33} + \mathcal{I}[q^4]^{42})$	$\mathrm{tr}([\mathcal{P}^\mu, U_{HL}]U_{LH}[\mathcal{P}^\nu, G'_{\mu\nu}])$
$f^2_{PPU,g} = -ic_s4(\mathcal{I}[q^4]^{33} + \mathcal{I}[q^4]^{42})$	$\mathrm{tr}(U_{HL}[\mathcal{P}^\mu, U_{LH}][\mathcal{P}^\nu, G'_{\nu\mu}])$
$f^2_{PPU,h} = -ic_s4(\mathcal{I}[q^4]^{33} + \mathcal{I}[q^4]^{24})$	$\mathrm{tr}(U_{LH}[\mathcal{P}^\mu, U_{HL}][\mathcal{P}^\nu, G'_{\nu\mu}])$
$f^2_{PPU,i} = -ic_s4(\mathcal{I}[q^4]^{33} + \mathcal{I}[q^4]^{24})$	$\mathrm{tr}([\mathcal{P}^\mu, U_{LH}]U_{HL}[\mathcal{P}^\nu, G'_{\mu\nu}])$

TABLE VIII. Effective action formulas with two P's (Part II).

Factors	Formulas
$f_{PU,a}^{4(HH)} = -ic_s 2(\mathcal{I}[q^2]^{42} + 2\mathcal{I}[q^2]^{51})$	$\mathrm{tr}([\mathcal{P}_\mu, U_H][\mathcal{P}^\mu, U_H]U_{HL}U_{LH})$
$f_{PU,b}^{4(HH)} = -ic_s 4(\mathcal{I}[q^2]^{42} + \mathcal{I}[q^2]^{51})$	$\mathrm{tr}([\mathcal{P}_\mu, U_H]U_H[\mathcal{P}^\mu, U_{HL}]U_{LH})$
$f_{PU,c}^{4(HH)} = -ic_s 2(\mathcal{I}[q^2]^{42} + 2\mathcal{I}[q^2]^{51})$	$\mathrm{tr}([\mathcal{P}_\mu, U_H]U_H U_{HL}[\mathcal{P}^\mu, U_{LH}])$
$f_{PU,d}^{4(HH)} = -ic_s 4(\mathcal{I}[q^2]^{42} + \mathcal{I}[q^2]^{51})$	$\mathrm{tr}(U_H[\mathcal{P}_\mu, U_H]U_{HL}[\mathcal{P}^\mu, U_{LH}])$
$f_{PU,e}^{4(HH)} = -ic_s 6\mathcal{I}[q^2]^{42}$	$\mathrm{tr}(U_H U_H[\mathcal{P}_\mu, U_{HL}][\mathcal{P}^\mu, U_{LH}])$
$f_{PU,f}^{4(HH)} = -ic_s 2(\mathcal{I}[q^2]^{42} + 2\mathcal{I}[q^2]^{51})$	$\mathrm{tr}(U_H[\mathcal{P}_\mu, U_H][\mathcal{P}^\mu, U_{HL}]U_{LH})$
$f_{PU,a}^{4(HL)} = -ic_s 2(\mathcal{I}[q^2]^{33} + \mathcal{I}[q^2]^{42})$	$\mathrm{tr}([\mathcal{P}_\mu, U_H][\mathcal{P}^\mu, U_{HL}]U_L U_{LH})$
$f_{PU,b}^{4(HL)} = -ic_s 2(\mathcal{I}[q^2]^{33} + 2\mathcal{I}[q^2]^{42})$	$\mathrm{tr}([\mathcal{P}_\mu, U_{LH}][\mathcal{P}^\mu, U_H]U_{HL}U_L)$
$f_{PU,c}^{4(HL)} = -ic_s 2(\mathcal{I}[q^2]^{24} + 2\mathcal{I}[q^2]^{33})$	$\mathrm{tr}(U_H U_{HL}[\mathcal{P}_\mu, U_L][\mathcal{P}^\mu, U_{LH}])$
$f_{PU,d}^{4(HL)} = -ic_s 2(\mathcal{I}[q^2]^{24} + 2\mathcal{I}[q^2]^{33})$	$\mathrm{tr}(U_H[\mathcal{P}_\mu, U_{HL}][\mathcal{P}^\mu, U_L]U_{LH})$
$f_{PU,e}^{4(HL)} = -ic_s 2(\mathcal{I}[q^2]^{24} + 2\mathcal{I}[q^2]^{33} + \mathcal{I}[q^2]^{42})$	$\mathrm{tr}([\mathcal{P}_\mu, U_H]U_{HL}[\mathcal{P}^\mu, U_L]U_{LH})$
$f_{PU,f}^{4(HL)} = -ic_s 8(\mathcal{I}[q^2]^{33})$	$\mathrm{tr}(U_H[\mathcal{P}_\mu, U_{HL}]U_L[\mathcal{P}^\mu, U_{LH}])$
$f_{PU,a}^{4(LL)} = -ic_s 2(2\mathcal{I}[q^2]^{15} + \mathcal{I}[q^2]^{24})$	$\mathrm{tr}([\mathcal{P}_\mu, U_{HL}][\mathcal{P}^\mu, U_L]U_L U_{LH})$
$f_{PU,b}^{4(LL)} = -ic_s 4(\mathcal{I}[q^2]^{15} + \mathcal{I}[q^2]^{24})$	$\mathrm{tr}([\mathcal{P}_\mu, U_{HL}]U_L[\mathcal{P}^\mu, U_L]U_{LH})$
$f_{PU,c}^{4(LL)} = -ic_s 6\mathcal{I}[q^2]^{24}$	$\mathrm{tr}([\mathcal{P}_\mu, U_{HL}]U_L U_L[\mathcal{P}^\mu, U_{LH}])$
$f_{PU,d}^{4(LL)} = -ic_s 2(2\mathcal{I}[q^2]^{15} + \mathcal{I}[q^2]^{24})$	$\mathrm{tr}(U_{HL}[\mathcal{P}_\mu, U_L][\mathcal{P}^\mu, U_L]U_{LH})$
$f_{PU,e}^{4(LL)} = -ic_s 4(\mathcal{I}[q^2]^{15} + \mathcal{I}[q^2]^{24})$	$\mathrm{tr}(U_{HL}[\mathcal{P}_\mu, U_L]U_L[\mathcal{P}^\mu, U_{LH}])$
$f_{PU,f}^{4(LL)} = -ic_s 2(2\mathcal{I}[q^2]^{15} + \mathcal{I}[q^2]^{24})$	$\mathrm{tr}(U_{HL}U_L[\mathcal{P}_\mu, U_L][\mathcal{P}^\mu, U_{LH}])$
$f_{PU,a}^{4(00)} = -ic_s(\mathcal{I}[q^2]^{24} + 2\mathcal{I}[q^2]^{33} + \mathcal{I}[q^2]^{42})$	$\mathrm{tr}([\mathcal{P}_\mu, U_{HL}]U_{LH}[\mathcal{P}^\mu, U_{HL}]U_{LH})$
$f_{PU,b}^{4(00)} = -ic_s 2(\mathcal{I}[q^2]^{24} + 2\mathcal{I}[q^2]^{33})$	$\mathrm{tr}([\mathcal{P}_\mu, U_{HL}][\mathcal{P}^\mu, U_{LH}]U_{HL}U_{LH})$
$f_{PU,c}^{4(00)} = -ic_s 2(2\mathcal{I}[q^2]^{33} + \mathcal{I}[q^2]^{42})$	$\mathrm{tr}([\mathcal{P}_\mu, U_{HL}]U_{LH}U_{HL}[\mathcal{P}^\mu, U_{LH}])$
$f_{PU,d}^{4(00)} = -ic_s(\mathcal{I}[q^2]^{24} + 2\mathcal{I}[q^2]^{33} + \mathcal{I}[q^2]^{42})$	$\mathrm{tr}(U_{HL}[\mathcal{P}_\mu, U_{LH}]U_{HL}[\mathcal{P}^\mu, U_{LH}])$

TABLE IX. Table of integration factors ($\mathcal{I}$). The matching scale is equal to the heavy-field mass $\mu = M$.

$\mathcal{I}[q^{2n}]^{\alpha\beta}\vert_{n=0}$	Factor $\times \frac{i}{16\pi^2}$	$\mathcal{I}[q^{2n}]^{\alpha\beta}\vert_{n=1,2}$	Factor $\times \frac{i}{16\pi^2}$
$\mathcal{I}^{11}$	1	$\mathcal{I}[q^2]^{13}$	$\frac{3}{8M^2}$
$\mathcal{I}^{12}$	$\frac{1}{M^2}$	$\mathcal{I}[q^2]^{22}$	$-\frac{1}{4M^2}$
$\mathcal{I}^{21}$	$-\frac{1}{M^2}$	$\mathcal{I}[q^2]^{31}$	$-\frac{1}{8M^2}$
$\mathcal{I}^{13}$	$\frac{1}{M^4}$	$\mathcal{I}[q^2]^{14}$	$\frac{3}{8M^4}$
$\mathcal{I}^{22}$	$-\frac{2}{M^4}$	$\mathcal{I}[q^2]^{23}$	$-\frac{5}{8M^4}$
$\mathcal{I}^{31}$	$\frac{1}{2M^4}$	$\mathcal{I}[q^2]^{32}$	$\frac{1}{8M^4}$
$\mathcal{I}^{14}$	$\frac{1}{M^6}$	$\mathcal{I}[q^2]^{41}$	$\frac{1}{24M^4}$
$\mathcal{I}^{23}$	$-\frac{3}{M^6}$	$\mathcal{I}[q^2]^{15}$	$\frac{3}{8M^6}$
$\mathcal{I}^{32}$	$\frac{5}{2M^6}$	$\mathcal{I}[q^2]^{24}$	$-\frac{1}{M^6}$
$\mathcal{I}^{41}$	$-\frac{1}{3M^6}$	$\mathcal{I}[q^2]^{33}$	$\frac{3}{4M^6}$
$\mathcal{I}^{15}$	$\frac{1}{M^8}$	$\mathcal{I}[q^2]^{42}$	$-\frac{1}{12M^6}$
$\mathcal{I}^{24}$	$-\frac{4}{M^8}$	$\mathcal{I}[q^2]^{51}$	$-\frac{1}{48M^6}$
$\mathcal{I}^{33}$	$\frac{11}{2M^8}$	$\mathcal{I}[q^2]^{51}$	$-\frac{1}{48M^6}$
$\mathcal{I}^{42}$	$-\frac{17}{6M^8}$	$\mathcal{I}[q^4]^{15}$	$\frac{11}{144M^4}$
$\mathcal{I}^{51}$	$\frac{1}{4M^8}$	$\mathcal{I}[q^4]^{24}$	$-\frac{17}{144M^4}$
		$\mathcal{I}[q^4]^{33}$	$\frac{1}{48M^4}$
		$\mathcal{I}[q^4]^{42}$	$\frac{1}{144M^4}$
		$\mathcal{I}[q^4]^{42}$	$\frac{1}{288M^4}$

APPENDIX B: MATCHING RESULTS FOR SCALAR-EXTENDED SM SCENARIOS

1. Color-singlet heavy scalars

Here we provide exhaustive sets of effective operators and the associated WCs that emerge after integrating out the color-singlet heavy scalars up to one loop including the heavy-light mixing.

a. Real singlet: $\mathcal{S} \equiv (\mathbf{1}_C, \mathbf{1}_L, 0|_Y)$

Here we extend the SM by a real gauge singlet scalar ($\mathcal{S}$), and the modified Lagrangian involving this heavy field is written as [108,173,174,191]

$$\mathcal{L}_{\mathcal{S}} = \mathcal{L}_{\rm SM}^{d\leq 4} + \frac{1}{2}(\partial_\mu \mathcal{S})^2 - \frac{1}{2}m_{\mathcal{S}}^2\mathcal{S}^2 - c_{\mathcal{S}}|H|^2\mathcal{S} - \frac{1}{2}\kappa_{\mathcal{S}}|H|^2\mathcal{S}^2 - \frac{1}{3!}\mu_{\mathcal{S}}\mathcal{S}^3 - \frac{1}{4!}\lambda_{\mathcal{S}}\mathcal{S}^4. \tag{B1}$$

Here $m_{\mathcal{S}}$ is mass of the heavy field ($\mathcal{S}$). This model contains four BSM parameters ($c_{\mathcal{S}}$, $\kappa_{\mathcal{S}}$, $\mu_{\mathcal{S}}$, $\lambda_{\mathcal{S}}$) and the WCs are functions of these parameters along with the SM ones; see Table X.

b. Real triplet: $\boldsymbol{\Delta} \equiv (\mathbf{1}_C, \mathbf{3}_L, 0|_Y)$

In this model we extend the SM by a real color-singlet isospin-triplet scalar (Δ). The Lagrangian involving the heavy field is written as [103,109]

$$\mathcal{L}_{\Delta} = \mathcal{L}_{\rm SM}^{d\leq 4} + \frac{1}{2}(\mathcal{D}_\mu \Delta)^2 - \frac{1}{2}m_{\Delta}^2\Delta^a\Delta^a + 2\kappa_{\Delta}H^\dagger\tau^a H\Delta^a - \eta_{\Delta}|H|^2\Delta^a\Delta^a - \frac{1}{4}\lambda_{\Delta}(\Delta^a\Delta^a)^2. \tag{B2}$$

Here m_{Δ} is mass of the heavy field. This model contains three BSM parameters (κ_{Δ}, η_{Δ}, λ_{Δ}) and the WCs are functions of these parameters along with the SM ones; see Table XI.

c. Complex singlet: $\boldsymbol{\mathcal{S}_1} \equiv (\mathbf{1}_C, \mathbf{1}_L, \mathbf{1}|_Y)$

Here we extend the SM by a color-singlet isospin-singlet scalar ($\mathcal{S}_1$) with hypercharge $Y = 1$. The Lagrangian involving the heavy field is written as [192,193]

$$\mathcal{L}_{\mathcal{S}_1} = \mathcal{L}_{\rm SM}^{d\leq 4} + (D_\mu \mathcal{S}_1)^\dagger (D^\mu \mathcal{S}_1) - m_{\mathcal{S}_1}^2\mathcal{S}_1^\dagger\mathcal{S}_1 - \eta_{\mathcal{S}_1}|H|^2|\mathcal{S}_1|^2 - \lambda_{\mathcal{S}_1}|\mathcal{S}_1|^4 - \{y_{\mathcal{S}_1} l_L^T C i\sigma^2 l_L \mathcal{S}_1 + \text{H.c.}\}. \tag{B3}$$

Here $m_{\mathcal{S}_1}$ is the mass of the heavy field. This model contains three BSM parameters ($\eta_{\mathcal{S}_1}$, $\lambda_{\mathcal{S}_1}$, $y_{\mathcal{S}_1}$) and the WCs are functions of these parameters along with the SM ones; see Table XII.

TABLE X. Warsaw basis effective operators and the associated WCs that emerge after integrating out the heavy field $\mathcal{S}$: $(1, 1, 0)$. See Table III for color coding.

Dimension-six operators	Wilson coefficients
$Q_{\rm dH}$	$-\frac{3Y_d^{\rm SM}c_{\mathcal{S}}^2\kappa_{\mathcal{S}}}{64\pi^2 m_{\mathcal{S}}^4} + \frac{Y_d^{\rm SM}c_{\mathcal{S}}^3\mu_{\mathcal{S}}}{64\pi^2 m_{\mathcal{S}}^6} - \frac{9Y_d^{\rm SM}c_{\mathcal{S}}^4}{64\pi^2 m_{\mathcal{S}}^6} + \frac{29\lambda_H^{\rm SM}Y_d^{\rm SM}c_{\mathcal{S}}^2}{192\pi^2 m_{\mathcal{S}}^4}$
$Q_{\rm eH}$	$-\frac{3Y_e^{\rm SM}c_{\mathcal{S}}^2\kappa_{\mathcal{S}}}{64\pi^2 m_{\mathcal{S}}^4} + \frac{Y_e^{\rm SM}c_{\mathcal{S}}^3\mu_{\mathcal{S}}}{64\pi^2 m_{\mathcal{S}}^6} - \frac{9Y_e^{\rm SM}c_{\mathcal{S}}^4}{64\pi^2 m_{\mathcal{S}}^6} + \frac{29\lambda_H^{\rm SM}Y_e^{\rm SM}c_{\mathcal{S}}^2}{192\pi^2 m_{\mathcal{S}}^4}$
$Q_{\rm uH}$	$-\frac{3Y_u^{\rm SM}c_{\mathcal{S}}^2\kappa_{\mathcal{S}}}{64\pi^2 m_{\mathcal{S}}^4} + \frac{Y_u^{\rm SM}c_{\mathcal{S}}^3\mu_{\mathcal{S}}}{64\pi^2 m_{\mathcal{S}}^6} - \frac{9Y_u^{\rm SM}c_{\mathcal{S}}^4}{64\pi^2 m_{\mathcal{S}}^6} + \frac{29\lambda_H^{\rm SM}Y_u^{\rm SM}c_{\mathcal{S}}^2}{192\pi^2 m_{\mathcal{S}}^4}$
Q_H	$\frac{43c_{\mathcal{S}}^6}{48\pi^2 m_{\mathcal{S}}^8} - \frac{7g_W^2\lambda_H^{\rm SM}c_{\mathcal{S}}^2}{288\pi^2 m_{\mathcal{S}}^4} + \frac{41\lambda_H^{\rm SM2}c_{\mathcal{S}}^2}{48\pi^2 m_{\mathcal{S}}^4} + \frac{37c_{\mathcal{S}}^4\kappa_{\mathcal{S}}}{32\pi^2 m_{\mathcal{S}}^6} + \frac{11c_{\mathcal{S}}^2\kappa_{\mathcal{S}}^2}{32\pi^2 m_{\mathcal{S}}^4} - \frac{c_{\mathcal{S}}^2\kappa_{\mathcal{S}}}{2m_{\mathcal{S}}^4} - \frac{c_{\mathcal{S}}^2\kappa_{\mathcal{S}}\lambda_{\mathcal{S}}}{32\pi^2 m_{\mathcal{S}}^4} - \frac{c_{\mathcal{S}}^4\lambda_{\mathcal{S}}}{32\pi^2 m_{\mathcal{S}}^6} - \frac{15c_{\mathcal{S}}^5\mu_{\mathcal{S}}}{32\pi^2 m_{\mathcal{S}}^8} - \frac{5c_{\mathcal{S}}^3\kappa_{\mathcal{S}}\mu_{\mathcal{S}}}{16\pi^2 m_{\mathcal{S}}^6} - \frac{c_{\mathcal{S}}\kappa_{\mathcal{S}}^2\mu_{\mathcal{S}}}{64\pi^2 m_{\mathcal{S}}^4} + \frac{c_{\mathcal{S}}^3\mu_{\mathcal{S}}}{6m_{\mathcal{S}}^6} + \frac{c_{\mathcal{S}}^2\kappa_{\mathcal{S}}\mu_{\mathcal{S}}^2}{32\pi^2 m_{\mathcal{S}}^6} + \frac{c_{\mathcal{S}}^3\lambda_{\mathcal{S}}\mu_{\mathcal{S}}}{48\pi^2 m_{\mathcal{S}}^6} + \frac{c_{\mathcal{S}}^4\mu_{\mathcal{S}}^2}{16\pi^2 m_{\mathcal{S}}^8} - \frac{57\lambda_H^{\rm SM}c_{\mathcal{S}}^4}{32\pi^2 m_{\mathcal{S}}^6} + \frac{13\lambda_H^{\rm SM}c_{\mathcal{S}}^3\mu_{\mathcal{S}}}{32\pi^2 m_{\mathcal{S}}^6} - \frac{c_{\mathcal{S}}^3\mu_{\mathcal{S}}^3}{96\pi^2 m_{\mathcal{S}}^8} - \frac{27\lambda_H^{\rm SM}c_{\mathcal{S}}^2\kappa_{\mathcal{S}}}{32\pi^2 m_{\mathcal{S}}^4} - \frac{\kappa_{\mathcal{S}}^3}{192\pi^2 m_{\mathcal{S}}^2}$
$Q_{H\Box}$	$\frac{13c_{\mathcal{S}}^4}{192\pi^2 m_{\mathcal{S}}^6} - \frac{c_{\mathcal{S}}^2}{2m_{\mathcal{S}}^4} - \frac{7g_W^2c_{\mathcal{S}}^2}{384\pi^2 m_{\mathcal{S}}^4} + \frac{25c_{\mathcal{S}}^2\kappa_{\mathcal{S}}}{192\pi^2 m_{\mathcal{S}}^4} - \frac{c_{\mathcal{S}}^2\lambda_{\mathcal{S}}}{32\pi^2 m_{\mathcal{S}}^4} - \frac{13c_{\mathcal{S}}^3\mu_{\mathcal{S}}}{192\pi^2 m_{\mathcal{S}}^6} - \frac{\kappa_{\mathcal{S}}^2}{384\pi^2 m_{\mathcal{S}}^2} + \frac{11c_{\mathcal{S}}^2\mu_{\mathcal{S}}^2}{384\pi^2 m_{\mathcal{S}}^6} - \frac{5c_{\mathcal{S}}\kappa_{\mathcal{S}}\mu_{\mathcal{S}}}{192\pi^2 m_{\mathcal{S}}^4} - \frac{7g_Y^2c_{\mathcal{S}}^2}{1152\pi^2 m_{\mathcal{S}}^4}$
$Q_{\rm HB}$	$\frac{g_Y^2c_{\mathcal{S}}^2}{256\pi^2 m_{\mathcal{S}}^4}$
$Q_{\rm HD}$	$-\frac{7g_Y^2c_{\mathcal{S}}^2}{288\pi^2 m_{\mathcal{S}}^4}$
$Q_{\rm Hd}$	$\frac{7g_Y^2c_{\mathcal{S}}^2}{1728\pi^2 m_{\mathcal{S}}^4}$
$Q_{\rm He}$	$\frac{7g_Y^2c_{\mathcal{S}}^2}{576\pi^2 m_{\mathcal{S}}^4}$
$Q_{\rm Hu}$	$-\frac{7g_Y^2c_{\mathcal{S}}^2}{864\pi^2 m_{\mathcal{S}}^4}$
$Q_{\rm HW}$	$\frac{g_W^2c_{\mathcal{S}}^2}{256\pi^2 m_{\mathcal{S}}^4}$
$Q_{\rm HWB}$	$\frac{g_Wg_Yc_{\mathcal{S}}^2}{128\pi^2 m_{\mathcal{S}}^4}$
$Q_{\rm Hl}^{(1)}$	$\frac{7g_Y^2c_{\mathcal{S}}^2}{1152\pi^2 m_{\mathcal{S}}^4}$
$Q_{\rm Hq}^{(1)}$	$-\frac{7g_Y^2c_{\mathcal{S}}^2}{3456\pi^2 m_{\mathcal{S}}^4}$
$Q_{\rm Hl}^{(3)}$	$-\frac{7g_W^2c_{\mathcal{S}}^2}{1152\pi^2 m_{\mathcal{S}}^4}$
$Q_{\rm Hq}^{(3)}$	$-\frac{7g_W^2c_{\mathcal{S}}^2}{1152\pi^2 m_{\mathcal{S}}^4}$
$Q_{\rm lequ}^{(1)}$	$\frac{Y_e^{\rm SM}Y_u^{\rm SM}c_{\mathcal{S}}^2}{96\pi^2 m_{\mathcal{S}}^4}$
$Q_{\rm qd}^{(1)}$	$-\frac{Y_d^{\rm SM}Y_d^{\rm SM\dagger}c_{\mathcal{S}}^2}{192\pi^2 m_{\mathcal{S}}^4}$
$Q_{\rm qu}^{(1)}$	$-\frac{Y_u^{\rm SM}Y_u^{\rm SM\dagger}c_{\mathcal{S}}^2}{192\pi^2 m_{\mathcal{S}}^4}$
$Q_{\rm quqd}^{(1)}$	$-\frac{Y_d^{\rm SM}Y_u^{\rm SM}c_{\mathcal{S}}^2}{96\pi^2 m_{\mathcal{S}}^4}$
$Q_{\rm le}$	$-\frac{Y_e^{\rm SM}Y_e^{\rm SM\dagger}c_{\mathcal{S}}^2}{192\pi^2 m_{\mathcal{S}}^4}$
$Q_{\rm ledq}$	$\frac{Y_d^{\rm SM\dagger}Y_e^{\rm SM}c_{\mathcal{S}}^2}{96\pi^2 m_{\mathcal{S}}^4}$

d. Complex singlet: $\boldsymbol{\mathcal{S}_2} \equiv (\mathbf{1}_C, \mathbf{1}_L, \mathbf{2}|_Y)$

In this model we extend the SM by a color-singlet isospin-triplet scalar ($\mathcal{S}_2$) with hypercharge $Y = 2$. The Lagrangian involving the heavy field is written as [177,194]

TABLE XI. Warsaw basis effective operators and the associated WCs that emerge after integrating out the heavy field $\Delta: (1,3,0)$. See Table III for color coding.

Dimension-six ops.	Wilson coefficients
Q_{dH}	$-\frac{21\eta_\Delta\kappa_\Delta^2 Y_d^{SM}}{32\pi^2 m_\Delta^4}-\frac{21\kappa_\Delta^4 Y_d^{SM}}{64\pi^2 m_\Delta^6}+\frac{\kappa_\Delta^2 Y_d^{SM}}{m_\Delta^4}+\frac{5\kappa_\Delta^2\lambda_\Delta Y_d^{SM}}{8\pi^2 m_\Delta^4}+\frac{27\kappa_\Delta^2\lambda_H^{SM} Y_d^{SM}}{64\pi^2 m_\Delta^4}$
Q_{eH}	$-\frac{21\eta_\Delta\kappa_\Delta^2 Y_e^{SM}}{32\pi^2 m_\Delta^4}-\frac{21\kappa_\Delta^4 Y_e^{SM}}{64\pi^2 m_\Delta^6}+\frac{\kappa_\Delta^2 Y_e^{SM}}{m_\Delta^4}+\frac{5\kappa_\Delta^2\lambda_\Delta Y_e^{SM}}{8\pi^2 m_\Delta^4}+\frac{27\kappa_\Delta^2\lambda_H^{SM} Y_e^{SM}}{64\pi^2 m_\Delta^4}$
Q_{uH}	$-\frac{21\eta_\Delta\kappa_\Delta^2 Y_u^{SM}}{32\pi^2 m_\Delta^4}-\frac{21\kappa_\Delta^4 Y_u^{SM}}{64\pi^2 m_\Delta^6}+\frac{\kappa_\Delta^2 Y_u^{SM}}{m_\Delta^4}+\frac{5\kappa_\Delta^2\lambda_\Delta Y_u^{SM}}{8\pi^2 m_\Delta^4}+\frac{27\kappa_\Delta^2\lambda_H^{SM} Y_u^{SM}}{64\pi^2 m_\Delta^4}$
Q_H	$-\frac{\eta_\Delta^3}{8\pi^2 m_\Delta^2}-\frac{\eta_\Delta\kappa_\Delta^2}{m_\Delta^4}+\frac{2\kappa_\Delta^2\lambda_H^{SM}}{m_\Delta^4}+\frac{13\eta_\Delta^2\kappa_\Delta^2}{8\pi^2 m_\Delta^4}+\frac{47\eta_\Delta\kappa_\Delta^4}{16\pi^2 m_\Delta^6}+\frac{19\kappa_\Delta^6}{16\pi^2 m_\Delta^8}$ $-\frac{g_W^2\kappa_\Delta^2\lambda_H^{SM}}{288\pi^2 m_\Delta^4}-\frac{5\eta_\Delta\kappa_\Delta^2\lambda_\Delta}{8\pi^2 m_\Delta^4}-\frac{5\kappa_\Delta^4\lambda_\Delta}{16\pi^2 m_\Delta^6}-\frac{53\eta_\Delta\kappa_\Delta^2\lambda_H^{SM}}{16\pi^2 m_\Delta^4}+\frac{5\kappa_\Delta^2\lambda_\Delta\lambda_H^{SM}}{4\pi^2 m_\Delta^4}$ $-\frac{85\kappa_\Delta^4\lambda_H^{SM}}{32\pi^2 m_\Delta^6}+\frac{3\kappa_\Delta^2\lambda_H^{SM2}}{2\pi^2 m_\Delta^4}$
$Q_{H\Box}$	$-\frac{g_W^4}{3840\pi^2 m_\Delta^2}-\frac{\eta_\Delta^2}{32\pi^2 m_\Delta^2}+\frac{\kappa_\Delta^2}{2m_\Delta^4}-\frac{g_W^2\kappa_\Delta^2}{384\pi^2 m_\Delta^4}-\frac{7g_Y^2\kappa_\Delta^2}{384\pi^2 m_\Delta^4}$ $-\frac{7\eta_\Delta\kappa_\Delta^2}{32\pi^2 m_\Delta^4}+\frac{5\kappa_\Delta^2\lambda_\Delta}{16\pi^2 m_\Delta^4}+\frac{3\kappa_\Delta^2\lambda_H^{SM}}{16\pi^2 m_\Delta^4}-\frac{13\kappa_\Delta^4}{64\pi^2 m_\Delta^6}$
Q_{HD}	$-\frac{7g_Y^2\kappa_\Delta^2}{96\pi^2 m_\Delta^4}+\frac{\eta_\Delta\kappa_\Delta^2}{\pi^2 m_\Delta^4}-\frac{2\kappa_\Delta^2}{m_\Delta^4}-\frac{5\kappa_\Delta^2\lambda_\Delta}{4\pi^2 m_\Delta^4}-\frac{3\kappa_\Delta^2\lambda_H^{SM}}{16\pi^2 m_\Delta^4}-\frac{\kappa_\Delta^4}{16\pi^2 m_\Delta^6}$
Q_{HW}	$\frac{\eta_\Delta g_W^2}{96\pi^2 m_\Delta^2}+\frac{25 g_W^2\kappa_\Delta^2}{768\pi^2 m_\Delta^4}$
$Q_{Hl}^{(3)}$	$-\frac{g_W^2\kappa_\Delta^2}{1152\pi^2 m_\Delta^4}-\frac{g_W^4}{960\pi^2 m_\Delta^2}$
$Q_{Hq}^{(3)}$	$-\frac{g_W^2\kappa_\Delta^2}{1152\pi^2 m_\Delta^4}-\frac{g_W^4}{960\pi^2 m_\Delta^2}$
$Q_{Hl}^{(1)}$	$\frac{7g_Y^2\kappa_\Delta^2}{384\pi^2 m_\Delta^4}$
$Q_{Hq}^{(1)}$	$-\frac{7g_Y^2\kappa_\Delta^2}{1152\pi^2 m_\Delta^4}$
Q_{Hd}	$\frac{7g_Y^2\kappa_\Delta^2}{576\pi^2 m_\Delta^4}$
Q_{He}	$\frac{7g_Y^2\kappa_\Delta^2}{192\pi^2 m_\Delta^4}$
Q_{Hu}	$-\frac{7g_Y^2\kappa_\Delta^2}{288\pi^2 m_\Delta^4}$
Q_{HB}	$\frac{3g_Y^2\kappa_\Delta^2}{256\pi^2 m_\Delta^4}$
Q_{HWB}	$-\frac{g_W g_Y\kappa_\Delta^2}{128\pi^2 m_\Delta^4}$
Q_{ll}	$-\frac{g_W^4}{3840\pi^2 m_\Delta^2}$
Q_W	$\frac{g_W^3}{2880\pi^2 m_\Delta^2}$
$Q_{lequ}^{(1)}$	$\frac{\kappa_\Delta^2 Y_e^{SM} Y_u^{SM}}{32\pi^2 m_\Delta^4}$
$Q_{qd}^{(1)}$	$-\frac{\kappa_\Delta^2 Y_d^{SM} Y_d^{SM\dagger}}{64\pi^2 m_\Delta^4}$
$Q_{qq}^{(1)}$	$\frac{g_W^4}{3840\pi^2 m_\Delta^2}$
$Q_{qu}^{(1)}$	$-\frac{\kappa_\Delta^2 Y_u^{SM} Y_u^{SM\dagger}}{64\pi^2 m_\Delta^4}$
$Q_{quqd}^{(1)}$	$-\frac{\kappa_\Delta^2 Y_d^{SM} Y_u^{SM}}{32\pi^2 m_\Delta^4}$
$Q_{lq}^{(3)}$	$-\frac{g_W^4}{1920\pi^2 m_\Delta^2}$
$Q_{qq}^{(3)}$	$-\frac{g_W^4}{3840\pi^2 m_\Delta^2}$
Q_{le}	$-\frac{\kappa_\Delta^2 Y_e^{SM} Y_e^{SM\dagger}}{64\pi^2 m_\Delta^4}$
Q_{ledq}	$\frac{\kappa_\Delta^2 Y_d^{SM\dagger} Y_e^{SM}}{32\pi^2 m_\Delta^4}$

TABLE XII. Warsaw basis effective operators and the associated WCs that emerge after integrating out the heavy field $\mathcal{S}_1: (1,1,1)$. See Table III for color coding.

Dimension-six ops.	Wilson coefficients
Q_H	$\frac{\eta_{\mathcal{S}_1}^3}{96\pi^2 m_{\mathcal{S}_1}^2}$
Q_{HB}	$-\frac{\eta_{\mathcal{S}_1} g_Y^2}{192\pi^2 m_{\mathcal{S}_1}^2}$
$Q_{H\Box}$	$-\frac{\eta_{\mathcal{S}_1}^2}{192\pi^2 m_{\mathcal{S}_1}^2}$
Q_{ll}	$-\frac{g_Y^4}{3840\pi^2 m_{\mathcal{S}_1}^2}+\frac{y_{\mathcal{S}_1}^2}{4m_{\mathcal{S}_1}^2}-\frac{y_{\mathcal{S}_1}^2\lambda_{\mathcal{S}_1}}{16\pi^2 m_{\mathcal{S}_1}^2}$
$Q_{Hl}^{(1)}$	$\frac{g_Y^4}{1920\pi^2 m_{\mathcal{S}_1}^2}$
$Q_{Hq}^{(1)}$	$-\frac{g_Y^4}{5760\pi^2 m_{\mathcal{S}_1}^2}$
Q_{HD}	$-\frac{g_Y^4}{960\pi^2 m_{\mathcal{S}_1}^2}$
Q_{Hd}	$\frac{g_Y^4}{2880\pi^2 m_{\mathcal{S}_1}^2}$
Q_{He}	$\frac{g_Y^4}{960\pi^2 m_{\mathcal{S}_1}^2}$
Q_{Hu}	$-\frac{g_Y^4}{1440\pi^2 m_{\mathcal{S}_1}^2}$
$Q_{lq}^{(1)}$	$\frac{g_Y^4}{5760\pi^2 m_{\mathcal{S}_1}^2}$
$Q_{qd}^{(1)}$	$\frac{g_Y^4}{8640\pi^2 m_{\mathcal{S}_1}^2}$
Q_{ed}	$-\frac{g_Y^4}{1440\pi^2 m_{\mathcal{S}_1}^2}$
Q_{ee}	$-\frac{g_Y^4}{960\pi^2 m_{\mathcal{S}_1}^2}$
Q_{eu}	$\frac{g_Y^4}{720\pi^2 m_{\mathcal{S}_1}^2}$
Q_{ld}	$-\frac{g_Y^4}{2880\pi^2 m_{\mathcal{S}_1}^2}$
Q_{le}	$-\frac{g_Y^4}{960\pi^2 m_{\mathcal{S}_1}^2}$
Q_{lu}	$\frac{g_Y^4}{1440\pi^2 m_{\mathcal{S}_1}^2}$
Q_{qe}	$\frac{g_Y^4}{2880\pi^2 m_{\mathcal{S}_1}^2}$
Q_{uu}	$-\frac{g_Y^4}{2160\pi^2 m_{\mathcal{S}_1}^2}$
Q_{dd}	$-\frac{g_Y^4}{8640\pi^2 m_{\mathcal{S}_1}^2}$
$Q_{qu}^{(1)}$	$-\frac{g_Y^4}{4320\pi^2 m_{\mathcal{S}_1}^2}$
$Q_{qq}^{(1)}$	$-\frac{g_Y^4}{34560\pi^2 m_{\mathcal{S}_1}^2}$
$Q_{ud}^{(1)}$	$\frac{g_Y^4}{2160\pi^2 m_{\mathcal{S}_1}^2}$

$$\mathcal{L}_{\mathcal{S}_2}=\mathcal{L}_{SM}^{d\le 4}+(D_\mu\mathcal{S}_2)^\dagger(D^\mu\mathcal{S}_2)-m_{\mathcal{S}_2}^2\mathcal{S}_2^\dagger\mathcal{S}_2-\eta_{\mathcal{S}_2}|H|^2|\mathcal{S}_2|^2 -\lambda_{\mathcal{S}_2}|\mathcal{S}_2|^4-\{y_{\mathcal{S}_2}e_R^T C e_R\mathcal{S}_2+\text{H.c.}\}. \tag{B4}$$

Here $m_{\mathcal{S}_2}$ is the mass of the heavy field. This model contains three BSM parameters ($\eta_{\mathcal{S}_2}$, $\lambda_{\mathcal{S}_2}$, $y_{\mathcal{S}_2}$) and the WCs are

TABLE XIII. Warsaw basis effective operators and the associated WCs that emerge after integrating out the heavy field $\mathcal{S}_2$: $(1,1,2)$. See Table III for color coding.

Dimension-six operators	Wilson coefficients
Q_H	$\frac{\eta_{S_2}^3}{96\pi^2 m_{S_2}^2}$
Q_{HB}	$-\frac{\eta_{S_2} g_Y^2}{48\pi^2 m_{S_2}^2}$
$Q_{H\Box}$	$-\frac{\eta_{S_2}^2}{192\pi^2 m_{S_2}^2}$
$Q_{Hl}^{(1)}$	$\frac{g_Y^4}{480\pi^2 m_{S_2}^2}$
$Q_{Hq}^{(1)}$	$-\frac{g_Y^4}{1440\pi^2 m_{S_2}^2}$
Q_{HD}	$-\frac{g_Y^4}{240\pi^2 m_{S_2}^2}$
Q_{Hd}	$\frac{g_Y^4}{720\pi^2 m_{S_2}^2}$
Q_{He}	$\frac{g_Y^4}{240\pi^2 m_{S_2}^2}$
Q_{Hu}	$-\frac{g_Y^4}{360\pi^2 m_{S_2}^2}$
Q_{ll}	$-\frac{g_Y^4}{960\pi^2 m_{S_2}^2}$
Q_{ld}	$-\frac{g_Y^4}{720\pi^2 m_{S_2}^2}$
Q_{le}	$-\frac{g_Y^4}{240\pi^2 m_{S_2}^2}$
Q_{lu}	$\frac{g_Y^4}{360\pi^2 m_{S_2}^2}$
$Q_{lq}^{(1)}$	$\frac{g_Y^4}{1440\pi^2 m_{S_2}^2}$
$Q_{qd}^{(1)}$	$\frac{g_Y^4}{2160\pi^2 m_{S_2}^2}$
$Q_{qq}^{(1)}$	$-\frac{g_Y^4}{8640\pi^2 m_{S_2}^2}$
$Q_{qu}^{(1)}$	$-\frac{g_Y^4}{1080\pi^2 m_{S_2}^2}$
$Q_{ud}^{(1)}$	$\frac{g_Y^4}{540\pi^2 m_{S_2}^2}$
Q_{dd}	$-\frac{g_Y^4}{2160\pi^2 m_{S_2}^2}$
Q_{ed}	$-\frac{g_Y^4}{360\pi^2 m_{S_2}^2}$
Q_{eu}	$\frac{g_Y^4}{180\pi^2 m_{S_2}^2}$
Q_{uu}	$-\frac{g_Y^4}{540\pi^2 m_{S_2}^2}$
Q_{qe}	$\frac{g_Y^4}{720\pi^2 m_{S_2}^2}$
Q_{ee}	$-\frac{g_Y^4}{240\pi^2 m_{S_2}^2} - \frac{\lambda_{S_2} y_{S_2}^2}{16\pi^2 m_{S_2}^2} + \frac{y_{S_2}^2}{4 m_{S_2}^2}$

functions of these parameters along with the SM ones; see Table XIII.

e. Complex triplet: $\Delta_1 \equiv (\mathbf{1}_C, \mathbf{3}_L, \mathbf{1}|_Y)$

Here we extend the SM by a color-singlet isospin-triplet scalar (Δ_1) with hypercharge $Y = 1$. This model is also known as a "type-II seesaw." The Lagrangian involving the heavy field is written as [124]

$$\mathcal{L}_{\Delta_1} = \mathcal{L}_{\rm SM}^{d\le 4} + \mathrm{Tr}[(D_\mu \Delta_1)^\dagger (D^\mu \Delta_1)] - m_{\Delta_1}^2 \mathrm{Tr}[\Delta_1^\dagger \Delta_1] - \mathcal{L}_Y - V(H, \Delta_1), \tag{B5}$$

where

$$V(H,\Delta_1) = \lambda_{\Delta_1,1}(H^\dagger H)\mathrm{Tr}[\Delta_1^\dagger \Delta_1] + \lambda_{\Delta_1,2}(\mathrm{Tr}[\Delta_1^\dagger \Delta_1])^2 + \lambda_{\Delta_1,3}\mathrm{Tr}[(\Delta_1^\dagger \Delta_1)^2] + \lambda_{\Delta_1,4}\mathrm{Tr}[H^\dagger \Delta_1 \Delta_1{}^\dagger H] + [\mu_{\Delta_1}(H^T i\sigma^2 \Delta_1^\dagger H) + \mathrm{H.c.}], \tag{B6}$$

$$\text{and,} \qquad \mathcal{L}_Y = y_{\Delta_1} l_L^T C i\sigma^2 \Delta_1 l_L + \mathrm{H.c.} \tag{B7}$$

Here m_{Δ_1} is the mass of the heavy field. This model contains six BSM parameters ($\lambda_{\Delta_1,1}$, $\lambda_{\Delta_1,2}$, $\lambda_{\Delta_1,3}$, $\lambda_{\Delta_1,4}$, μ_{Δ_1}, y_{Δ_1}) and the WCs are functions of these parameters along with the SM ones; see Table XIV.

f. Complex quartet: $\Sigma \equiv (\mathbf{1}_C, \mathbf{4}_L, \frac{\mathbf{1}}{\mathbf{2}}|_Y)$

Here we extend the SM by a color-singlet isospin-quartet scalar (Σ) with hypercharge $Y = \frac{1}{2}$. The Lagrangian involving the heavy field is written as [125,126,191]

$$\mathcal{L}_\Sigma = \mathcal{L}_{\rm SM}^{d\le 4} + (D_\mu \Sigma)^\dagger (D^\mu \Sigma) - m_\Sigma^2 \Sigma^\dagger \Sigma - \mu_\Sigma[(\Sigma^\dagger H)^2 + \mathrm{H.c.}] - \kappa_\Sigma[\Sigma^\dagger B_\Sigma + \mathrm{H.c.}] - \zeta_\Sigma^{(1)}(H^\dagger H)(\Sigma^\dagger \Sigma) - \zeta_\Sigma^{(2)}(H^\dagger \tau^I H)(\Sigma^\dagger T_4^I \Sigma) - \lambda_\Sigma^{(1)}(\Sigma^\dagger \Sigma)^2 - \lambda_\Sigma^{(2)}(\Sigma^\dagger T_4^I \Sigma)^2. \tag{B8}$$

Here m_Σ is the mass of the heavy field. The T_4^I's are the $SU(2)$ generators in four-dimensional representation, and $B_\Sigma = (H_1^2 \tilde{H}_1, \frac{1}{\sqrt{3}} H_1^2 \tilde{H}_2 + \frac{2}{\sqrt{3}} H_1 H_2 \tilde{H}_1, \frac{1}{\sqrt{3}} H_2^2 \tilde{H}_1 + \frac{2}{\sqrt{3}} H_1 H_2 \tilde{H}_2, H_2^2 \tilde{H}_2)^T$. This model contains six BSM parameters (κ_Σ, μ_Σ, $\zeta_\Sigma^{(1)}$, $\zeta_\Sigma^{(2)}$, $\lambda_\Sigma^{(1)}$, $\lambda_\Sigma^{(2)}$) and the WCs are functions of these parameters along with the SM ones; see Table XV.

2. Color-nonsinglet heavy-scalar leptoquarks

Here we provide exhaustive sets of effective operators and the associated WCs that emerge after integrating out the heavy color nonsinglet heavy scalars up to one loop.

a. Complex color triplet, isospin singlet: $\varphi_1 \equiv (\mathbf{3}_C, \mathbf{1}_L, -\frac{\mathbf{1}}{\mathbf{3}}|_Y)$

In this model we extend the SM by a color-triplet isospin-singlet scalar (φ_1) with hypercharge $Y = -\frac{1}{3}$. The Lagrangian involving the heavy field is written as [129,130]

TABLE XIV. Warsaw basis effective operators and the associated WCs that emerge after integrating out the heavy field $\Delta_1: (1,3,1)$. See Table III for color coding.

Dimension-six operators	Wilson coefficients
Q_{uH}	$\frac{3\mu_{\Delta_1}^2 \lambda_H^{SM} Y_u^{SM}}{2\pi^2 m_{\Delta_1}^4} - \frac{37\mu_{\Delta_1}^4 Y_u^{SM}}{6\pi^2 m_{\Delta_1}^6} + \frac{2\mu_{\Delta_1}^2 Y_u^{SM}}{m_{\Delta_1}^4} - \frac{5\mu_{\Delta_1}^2 \lambda_{\Delta_1,1} Y_u^{SM}}{8\pi^2 m_{\Delta_1}^4} - \frac{37\mu_{\Delta_1}^2 \lambda_{\Delta_1,4} Y_u^{SM}}{48\pi^2 m_{\Delta_1}^4} + \frac{\lambda_{\Delta_1,4}{}^2 Y_u^{SM}}{48\pi^2 m_{\Delta_1}^2}$
Q_{dH}	$\frac{3\mu_{\Delta_1}^2 \lambda_H^{SM} Y_d^{SM}}{2\pi^2 m_{\Delta_1}^4} - \frac{37\mu_{\Delta_1}^4 Y_d^{SM}}{6\pi^2 m_{\Delta_1}^6} + \frac{2\mu_{\Delta_1}^2 Y_d^{SM}}{m_{\Delta_1}^4} - \frac{5\mu_{\Delta_1}^2 \lambda_{\Delta_1,1} Y_d^{SM}}{8\pi^2 m_{\Delta_1}^4} - \frac{37\mu_{\Delta_1}^2 \lambda_{\Delta_1,4} Y_d^{SM}}{48\pi^2 m_{\Delta_1}^4} + \frac{\lambda_{\Delta_1,4}{}^2 Y_d^{SM}}{48\pi^2 m_{\Delta_1}^2}$
Q_{eH}	$\frac{3\mu_{\Delta_1}^2 \lambda_H^{SM} Y_e^{SM}}{2\pi^2 m_{\Delta_1}^4} - \frac{37\mu_{\Delta_1}^4 Y_e^{SM}}{6\pi^2 m_{\Delta_1}^6} + \frac{2\mu_{\Delta_1}^2 Y_e^{SM}}{m_{\Delta_1}^4} - \frac{5\mu_{\Delta_1}^2 \lambda_{\Delta_1,1} Y_e^{SM}}{8\pi^2 m_{\Delta_1}^4} - \frac{37\mu_{\Delta_1}^2 \lambda_{\Delta_1,4} Y_e^{SM}}{48\pi^2 m_{\Delta_1}^4} + \frac{\lambda_{\Delta_1,4}{}^2 Y_e^{SM}}{48\pi^2 m_{\Delta_1}^2}$
Q_H	$\frac{4\mu_{\Delta_1}^2 \lambda_H^{SM}}{m_{\Delta_1}^4} - \frac{4\mu_{\Delta_1}^2 \lambda_{\Delta_1,1}}{m_{\Delta_1}^4} - \frac{4\mu_{\Delta_1}^2 \lambda_{\Delta_1,4}}{m_{\Delta_1}{}^4} - \frac{g_W^2 \mu_{\Delta_1}^2 \lambda_H^{SM}}{72\pi^2 m_{\Delta_1}^4} - \frac{130\mu_{\Delta_1}^4 \lambda_H^{SM}}{3\pi^2 m_{\Delta_1}^6} + \frac{74\mu_{\Delta_1}^6}{\pi^2 m_{\Delta_1}^8} + \frac{45\mu_{\Delta_1}^2 \lambda_H^{SM2}}{8\pi^2 m_{\Delta_1}^4} - \frac{37\mu_{\Delta_1}^2 \lambda_H^{SM} \lambda_{\Delta_1,1}}{4\pi^2 m_{\Delta_1}^4} + \frac{48\mu_{\Delta_1}^4 \lambda_{\Delta_1,1}}{\pi^2 m_{\Delta_1}^6} + \frac{13\mu_{\Delta_1}^2 \lambda_{\Delta_1,1}{}^2}{2\pi^2 m_{\Delta_1}^4} - \frac{20\mu_{\Delta_1}^4 \lambda_{\Delta_1,2}}{\pi^2 m_{\Delta_1}^6} - \frac{16\mu_{\Delta_1}^2 \lambda_{\Delta_1,1} \lambda_{\Delta_1,2}}{\pi^2 m_{\Delta_1}^4} - \frac{12\mu_{\Delta_1}^2 \lambda_{\Delta_1,1} \lambda_{\Delta_1,3}}{\pi^2 m_{\Delta_1}^4} - \frac{20\mu_{\Delta_1}^4 \lambda_{\Delta_1,3}}{\pi^2 m_{\Delta_1}^6} - \frac{\lambda_{\Delta_1,1}{}^3}{4\pi^2 m_{\Delta_1}^2} + \frac{25\mu_{\Delta_1}^2 \lambda_{\Delta_1,1} \lambda_{\Delta_1,4}}{2\pi^2 m_{\Delta_1}^4} + \frac{97\mu_{\Delta_1}^4 \lambda_{\Delta_1,4}}{2\pi^2 m_{\Delta_1}^6} - \frac{229\mu_{\Delta_1}^2 \lambda_H^{SM} \lambda_{\Delta_1,4}}{24\pi^2 m_{\Delta_1}^4} + \frac{39\mu_{\Delta_1}^2 \lambda_{\Delta_1,4}{}^2}{8\pi^2 m_{\Delta_1}^4} + \frac{\lambda_H^{SM} \lambda_{\Delta_1,4}{}^2}{24\pi^2 m_{\Delta_1}^2} - \frac{3\lambda_{\Delta_1,1}{}^2 \lambda_{\Delta_1,4}}{8\pi^2 m_{\Delta_1}^2} - \frac{5\lambda_{\Delta_1,1} \lambda_{\Delta_1,4}{}^2}{16\pi^2 m_{\Delta_1}^2} - \frac{3\lambda_{\Delta_1,4}{}^3}{32\pi^2 m_{\Delta_1}^2}$
$Q_{H\Box}$	$-\frac{g_W^2 \mu_{\Delta_1}^2}{96\pi^2 m_{\Delta_1}^4} - \frac{g_W^4}{1920\pi^2 m_{\Delta_1}^2} + \frac{2\mu_{\Delta_1}^2}{m_{\Delta_1}^4} + \frac{11 g_Y^2 \mu_{\Delta_1}^2}{96\pi^2 m_{\Delta_1}^4} + \frac{21\mu_{\Delta_1}^2 \lambda_H^{SM}}{32\pi^2 m_{\Delta_1}{}^4} - \frac{41\mu_{\Delta_1}^4}{12\pi^2 m_{\Delta_1}^6} + \frac{\mu_{\Delta_1}^2 \lambda_{\Delta_1,1}}{8\pi^2 m_{\Delta_1}^4} - \frac{\mu_{\Delta_1}^2 \lambda_{\Delta_1,4}}{48\pi^2 m_{\Delta_1}^4} - \frac{\lambda_{\Delta_1,1}{}^2}{16\pi^2 m_{\Delta_1}^2} + \frac{\lambda_{\Delta_1,4}{}^2}{192\pi^2 m_{\Delta_1}^2} - \frac{\lambda_{\Delta_1,1} \lambda_{\Delta_1,4}}{16\pi^2 m_{\Delta_1}^2}$
Q_{HD}	$\frac{11 g_Y^2 \mu_{\Delta_1}^2}{24\pi^2 m_{\Delta_1}^4} - \frac{g_Y^4}{320\pi^2 m_{\Delta_1}^2} + \frac{4\mu_{\Delta_1}^2}{m_{\Delta_1}^4} + \frac{3\mu_{\Delta_1}^2 \lambda_H^{SM}}{8\pi^2 m_{\Delta_1}^4} + \frac{\mu_{\Delta_1}^2 \lambda_{\Delta_1,4}}{6\pi^2 m_{\Delta_1}^4} - \frac{8\mu_{\Delta_1}^4}{3\pi^2 m_{\Delta_1}^6} - \frac{\lambda_{\Delta_1,4}{}^2}{24\pi^2 m_{\Delta_1}^2}$
Q_{HB}	$\frac{11 g_Y^2 \mu_{\Delta_1}^2}{64\pi^2 m_{\Delta_1}^4} + \frac{g_Y^2 \lambda_{\Delta_1,1}}{32\pi^2 m_{\Delta_1}^2} + \frac{g_Y^2 \lambda_{\Delta_1,4}}{64\pi^2 m_{\Delta_1}^2}$
Q_{HW}	$\frac{25 g_W^2 \mu_{\Delta_1}^2}{192\pi^2 m_{\Delta_1}^4} + \frac{g_W^2 \lambda_{\Delta_1,1}}{48\pi^2 m_{\Delta_1}^2} + \frac{g_W^2 \lambda_{\Delta_1,4}}{96\pi^2 m_{\Delta_1}^2}$
Q_{HWB}	$-\frac{13 g_W g_Y \mu_{\Delta_1}^2}{96\pi^2 m_{\Delta_1}^4} - \frac{g_W g_Y \lambda_{\Delta_1,4}}{48\pi^2 m_{\Delta_1}^2}$
Q_{ll}	$-\frac{g_W^4}{1920\pi^2 m_{\Delta_1}^2} - \frac{g_Y^4}{1280\pi^2 m_{\Delta_1}^2} + \frac{y_{\Delta_1}^2}{2m_{\Delta_1}^2} + \frac{\lambda_{\Delta_1,2} y_{\Delta_1}^2}{\pi^2 m_{\Delta_1}^2} + \frac{3\lambda_{\Delta_1,3} y_{\Delta_1}^2}{4\pi^2 m_{\Delta_1}^2}$

(Table continued)

TABLE XIV. *(Continued)*

Dimension-six operators	Wilson coefficients
$Q_{Hq}{}^{(1)}$	$\frac{11 g_Y^2 \mu_{\Delta_1}^2}{288\pi^2 m_{\Delta_1}^4} - \frac{g_Y^4}{1920\pi^2 m_{\Delta_1}^2}$
Q_{Hd}	$\frac{g_Y^4}{960\pi^2 m_{\Delta_1}^2} - \frac{11 g_Y^2 \mu_{\Delta_1}^2}{144\pi^2 m_{\Delta_1}^4}$
Q_{He}	$\frac{g_Y^4}{320\pi^2 m_{\Delta_1}^2} - \frac{11 g_Y^2 \mu_{\Delta_1}^2}{48\pi^2 m_{\Delta_1}^4}$
Q_{Hu}	$\frac{11 g_Y^2 \mu_{\Delta_1}^2}{72\pi^2 m_{\Delta_1}^4} - \frac{g_Y^4}{480\pi^2 m_{\Delta_1}^2}$
$Q_{Hl}{}^{(3)}$	$-\frac{g_W^2 \mu_{\Delta_1}^2}{288\pi^2 m_{\Delta_1}^4} - \frac{g_W^4}{480\pi^2 m_{\Delta_1}^2}$
$Q_{Hq}{}^{(3)}$	$-\frac{g_W^2 \mu_{\Delta_1}^2}{288\pi^2 m_{\Delta_1}^4} - \frac{g_W^4}{480\pi^2 m_{\Delta_1}^2}$
$Q_{Hl}{}^{(1)}$	$\frac{g_Y^4}{640\pi^2 m_{\Delta_1}^2} - \frac{11 g_Y^2 \mu_{\Delta_1}^2}{96\pi^2 m_{\Delta_1}^4}$
Q_W	$\frac{g_W^3}{1440\pi^2 m_{\Delta_1}^2}$
Q_{le}	$-\frac{g_Y^4}{320\pi^2 m_{\Delta_1}^2} - \frac{\mu_{\Delta_1}^2 Y_e^{SM} Y_e^{SM\dagger}}{16\pi^2 m_{\Delta_1}^4}$
$Q_{qu}{}^{(1)}$	$-\frac{g_Y^4}{1440\pi^2 m_{\Delta_1}^2} - \frac{\mu_{\Delta_1}^2 Y_u^{SM} Y_u^{SM\dagger}}{16\pi^2 m_{\Delta_1}^4}$
$Q_{qd}{}^{(1)}$	$\frac{g_Y^4}{2880\pi^2 m_{\Delta_1}^2} - \frac{\mu_{\Delta_1}^2 Y_d^{SM} Y_d^{SM\dagger}}{16\pi^2 m_{\Delta_1}^4}$
$Q_{lq}{}^{(1)}$	$\frac{g_Y^4}{1920\pi^2 m_{\Delta_1}^2}$
$Q_{qq}{}^{(1)}$	$-\frac{g_Y^4}{11520\pi^2 m_{\Delta_1}^2}$
$Q_{quqd}{}^{(1)}$	$-\frac{\mu_{\Delta_1}^2 Y_d^{SM} Y_u^{SM}}{8\pi^2 m_{\Delta_1}^4}$
Q_{ld}	$-\frac{g_Y^4}{960\pi^2 m_{\Delta_1}^2}$
Q_{ledq}	$\frac{\mu_{\Delta_1}^2 Y_d^{SM\dagger} Y_e^{SM}}{8\pi^2 m_{\Delta_1}^4}$
Q_{ed}	$-\frac{g_Y^4}{480\pi^2 m_{\Delta_1}^2}$
Q_{lu}	$\frac{g_Y^4}{480\pi^2 m_{\Delta_1}^2}$
Q_{qe}	$\frac{g_Y^4}{960\pi^2 m_{\Delta_1}^2}$
Q_{uu}	$-\frac{g_Y^4}{720\pi^2 m_{\Delta_1}^2}$
Q_{ee}	$-\frac{g_Y^4}{320\pi^2 m_{\Delta_1}^2}$
Q_{eu}	$\frac{g_Y^4}{240\pi^2 m_{\Delta_1}^2}$
$Q_{lequ}{}^{(1)}$	$\frac{\mu_{\Delta_1}^2 Y_e^{SM} Y_u^{SM}}{8\pi^2 m_{\Delta_1}^4}$
$Q_{ud}{}^{(1)}$	$\frac{g_Y^4}{720\pi^2 m_{\Delta_1}^2}$
$Q_{lq}{}^{(3)}$	$-\frac{g_W^4}{960\pi^2 m_{\Delta_1}^2}$
$Q_{qq}{}^{(3)}$	$-\frac{g_W^4}{1920\pi^2 m_{\Delta_1}^2}$
Q_{dd}	$-\frac{g_Y^4}{2880\pi^2 m_{\Delta_1}^2}$

TABLE XV. Warsaw basis effective operators and the associated WCs that emerge after integrating out the heavy field Σ: $(1,4,\frac{1}{2})$. See Table III for color coding.

Dimension-six operators	Wilson coefficients
Q_{HW}	$-\frac{5g_W^2\zeta_\Sigma^{(1)}}{192\pi^2 m_\Sigma^2}$
Q_{HB}	$-\frac{g_Y^2\zeta_\Sigma^{(1)}}{192\pi^2 m_\Sigma^2}$
Q_{HWB}	$-\frac{5g_W g_Y\zeta_\Sigma^{(2)}}{384\pi^2 m_\Sigma^2}$
Q_H	$\frac{\zeta_\Sigma^{(1)3}}{24\pi^2 m_\Sigma^2}+\frac{5\zeta_\Sigma^{(1)}\zeta_\Sigma^{(2)2}}{128\pi^2 m_\Sigma^2}+\frac{5\zeta_\Sigma^{(2)2}\lambda_H^{\rm SM}}{192\pi^2 m_\Sigma^2}+\frac{5\mu_\Sigma^2\zeta_\Sigma^{(1)}}{36\pi^2 m_\Sigma^2}+\frac{5\mu_\Sigma^2\zeta_\Sigma^{(2)}}{144\pi^2 m_\Sigma^2}+\frac{5\mu_\Sigma^2\lambda_H^{\rm SM}}{108\pi^2 m_\Sigma^2}+\frac{\kappa_\Sigma^2}{3m_\Sigma^2}-\frac{5\kappa_\Sigma^2\lambda_{\Sigma_1}}{24\pi^2 m_\Sigma^2}-\frac{5\kappa_\Sigma^2\lambda_{\Sigma_2}}{32\pi^2 m_\Sigma^2}$
Q_{HD}	$-\frac{g_Y^4}{960\pi^2 m_\Sigma^2}+\frac{5\mu_\Sigma^2}{108\pi^2 m_\Sigma^2}-\frac{5\zeta_\Sigma^{(2)2}}{192\pi^2 m_\Sigma^2}$
Q_{uH}	$\frac{5\mu_\Sigma^2 Y_u^{\rm SM}}{216\pi^2 m_\Sigma^2}+\frac{5\zeta_\Sigma^{(2)2}Y_u^{\rm SM}}{384\pi^2 m_\Sigma^2}$
Q_{dH}	$\frac{5\mu_\Sigma^2 Y_d^{\rm SM}}{216\pi^2 m_\Sigma^2}+\frac{5\zeta_\Sigma^{(2)2}Y_d^{\rm SM}}{384\pi^2 m_\Sigma^2}$
Q_{eH}	$\frac{5\mu_\Sigma^2 Y_e^{\rm SM}}{216\pi^2 m_\Sigma^2}+\frac{5\zeta_\Sigma^{(2)2}Y_e^{\rm SM}}{384\pi^2 m_\Sigma^2}$
$Q_{H\Box}$	$-\frac{g_W^4}{768\pi^2 m_\Sigma^2}-\frac{\zeta_\Sigma^{(1)2}}{48\pi^2 m_\Sigma{}^2}+\frac{5\zeta_\Sigma^{(2)2}}{768\pi^2 m_\Sigma{}^2}+\frac{5\mu_\Sigma^2}{216\pi^2 m_\Sigma^2}+\frac{\kappa_\Sigma^2}{8\pi^2 m_\Sigma^2}$
$Q_{Hl}^{(1)}$	$\frac{g_Y^4}{1920\pi^2 m_\Sigma^2}$
$Q_{Hq}^{(1)}$	$-\frac{g_Y^4}{5760\pi^2 m_\Sigma^2}$
$Q_{Hl}^{(3)}$	$-\frac{g_W^4}{192\pi^2 m_\Sigma^2}$
$Q_{Hq}^{(3)}$	$-\frac{g_W^4}{192\pi^2 m_\Sigma^2}$
Q_{Hd}	$\frac{g_Y^4}{2880\pi^2 m_\Sigma^2}$
Q_{He}	$\frac{g_Y^4}{960\pi^2 m_\Sigma^2}$
Q_{Hu}	$-\frac{g_Y^4}{1440\pi^2 m_\Sigma^2}$
Q_W	$\frac{g_W^3}{576\pi^2 m_\Sigma^2}$
Q_{ll}	$-\frac{g_W^4}{768\pi^2 m_\Sigma^2}-\frac{g_Y^4}{3840\pi^2 m_\Sigma^2}$
Q_{eu}	$\frac{g_Y^4}{720\pi^2 m_\Sigma^2}$
$Q_{lq}^{(1)}$	$\frac{g_Y^4}{5760\pi^2 m_\Sigma^2}$
$Q_{qq}^{(1)}$	$-\frac{g_Y^4}{34560\pi^2 m_\Sigma^2}$
Q_{le}	$-\frac{g_Y^4}{960\pi^2 m_\Sigma^2}$
Q_{lu}	$\frac{g_Y^4}{1440\pi^2 m_\Sigma^2}$
Q_{qe}	$\frac{g_Y^4}{2880\pi^2 m_\Sigma^2}$
Q_{uu}	$-\frac{g_Y^4}{2160\pi^2 m_\Sigma^2}$
Q_{ld}	$-\frac{g_Y^4}{2880\pi^2 m_\Sigma^2}$
$Q_{qd}^{(1)}$	$\frac{g_Y^4}{8640\pi^2 m_\Sigma^2}$
$Q_{qu}^{(1)}$	$-\frac{g_Y^4}{4320\pi^2 m_\Sigma^2}$
$Q_{ud}^{(1)}$	$\frac{g_Y^4}{2160\pi^2 m_\Sigma^2}$
$Q_{lq}^{(3)}$	$-\frac{g_W^4}{384\pi^2 m_\Sigma^2}$
$Q_{qq}^{(3)}$	$-\frac{g_W^4}{768\pi^2 m_\Sigma^2}$
Q_{dd}	$-\frac{g_Y^4}{8640\pi^2 m_\Sigma^2}$
Q_{ed}	$-\frac{g_Y^4}{1440\pi^2 m_\Sigma^2}$
Q_{ee}	$-\frac{g_Y^4}{960\pi^2 m_\Sigma^2}$

$$\mathcal{L}_{\varphi_1} = \mathcal{L}_{\rm SM}^{d\le 4} + (D_\mu\varphi_1)^\dagger(D^\mu\varphi_1) - m_{\varphi_1}^2\varphi_1^\dagger\varphi_1 - \eta_{\varphi_1}H^\dagger H\varphi_1^\dagger\varphi_1 - \lambda_{\varphi_1}(\varphi_1^\dagger\varphi_1)^2 + \{y_{\varphi_1}^{(i)}\varphi_1^{\alpha\dagger}q_L^{\alpha T}Ci\sigma^2 l_L + y_{\varphi_1}^{(ii)}\varphi_1^{\alpha\dagger}u_R^{\alpha T}Ce_R + \text{H.c.}\}. \tag{B9}$$

Here m_{φ_1} is the mass of the heavy field. This model contains four BSM parameters (η_{φ_1}, λ_{φ_1}, $y_{\varphi_1}^{(i)}$, $y_{\varphi_1}^{(ii)}$) and the WCs are functions of these parameters along with the SM ones; see Table XVI.

b. Complex color triplet, isospin singlet: $\varphi_2 \equiv (\mathbf{3}_C,\mathbf{1}_L,-\frac{4}{3}|_Y)$

The heavy field (φ_2) in this model is a scalar leptoquark, similar to the model discussed above, but with a different hypercharge $Y=-\frac{4}{3}$. Consider the BSM Lagrangian [128,131]

$$\mathcal{L}_{\varphi_2} = \mathcal{L}_{\rm SM}^{d\le 4} + (D_\mu\varphi_2)^\dagger(D^\mu\varphi_2) - m_{\varphi_2}^2\varphi_2^\dagger\varphi_2 - \eta_{\varphi_2}H^\dagger H\varphi_2^\dagger\varphi_2 - \lambda_{\varphi_2}(\varphi_2^\dagger\varphi_2)^2 + \{y_{\varphi_2}\varphi_2^{\alpha\dagger}d_R^{\alpha T}Ce_R + \text{H.c.}\}. \tag{B10}$$

Here m_{φ_2} is the mass of the heavy field. This model contains three BSM parameters (η_{φ_2}, λ_{φ_2}, y_{φ_2}) and the WCs are functions of these parameters along with the SM ones; see Table XVII.

c. Complex color triplet, isospin doublet: $\Theta_2 \equiv (\mathbf{3}_C,\mathbf{2}_L,\frac{7}{6}|_Y)$

The heavy field (Θ_2) in this model is a scalar leptoquark, similar to the model discussed above, but with a different hypercharge $Y=\frac{7}{6}$. The Lagrangian involving the heavy field is written as [127,128,131]

TABLE XVI. Warsaw basis effective operators and the associated WCs that emerge after integrating out the heavy field φ_1: $(3,1,-\frac{1}{3})$. See Table III for color coding.

Dimension-six operators	Wilson coefficients
Q_H	$-\frac{\eta_{\varphi_1}^3}{32\pi^2 m_{\varphi_1}^2}$
Q_{HB}	$\frac{\eta_{\varphi_1} g_Y^2}{576\pi^2 m_{\varphi_1}^2}$
Q_{HG}	$\frac{g_S^2 \eta_{\varphi_1}}{384\pi^2 m_{\varphi_1}^2}$
$Q_{H\Box}$	$-\frac{\eta_{\varphi_1}^2}{64\pi^2 m_{\varphi_1}^2}$
$Q_{Hl}^{(1)}$	$\frac{g_Y^4}{5760\pi^2 m_{\varphi_1}^2}$
$Q_{Hq}^{(1)}$	$-\frac{g_Y^4}{17280\pi^2 m_{\varphi_1}^2}$
Q_G	$\frac{g_S^3}{5760\pi^2 m_{\varphi_1}^2}$
Q_{HD}	$-\frac{g_Y^4}{2880\pi^2 m_{\varphi_1}^2}$
Q_{Hu}	$-\frac{g_Y^4}{4320\pi^2 m_{\varphi_1}^2}$
Q_{Hd}	$\frac{g_Y^4}{8640\pi^2 m_{\varphi_1}^2}$
Q_{He}	$\frac{g_Y^4}{2880\pi^2 m_{\varphi_1}^2}$
Q_{ll}	$-\frac{g_Y^4}{11520\pi^2 m_{\varphi_1}^2}$
Q_{ld}	$-\frac{g_Y^4}{8640\pi^2 m_{\varphi_1}^2}$
Q_{le}	$-\frac{g_Y^4}{2880\pi^2 m_{\varphi_1}^2}$
Q_{lu}	$\frac{g_Y^4}{4320\pi^2 m_{\varphi_1}^2}$
Q_{qe}	$\frac{g_Y^4}{8640\pi^2 m_{\varphi_1}^2}$
Q_{ed}	$-\frac{g_Y^4}{4320\pi^2 m_{\varphi_1}^2}$
Q_{ee}	$-\frac{g_Y^4}{2880\pi^2 m_{\varphi_1}^2}$
$Q_{lq}^{(1)}$	$\frac{g_Y^4}{17280\pi^2 m_{\varphi_1}^2}$
$Q_{qq}^{(1)}$	$-\frac{g_Y^4}{103680\pi^2 m_{\varphi_1}^2}$
$Q_{ud}^{(1)}$	$\frac{g_Y^4}{6480\pi^2 m_{\varphi_1}^2}$
$Q_{ud}^{(8)}$	$-\frac{g_S^4}{960\pi^2 m_{\varphi_1}^2}$
$Q_{qu}^{(8)}$	$-\frac{g_S^4}{960\pi^2 m_{\varphi_1}^2}$
$Q_{qd}^{(8)}$	$-\frac{g_S^4}{960\pi^2 m_{\varphi_1}^2}$
$Q_{qu}^{(1)}$	$-\frac{g_Y^4}{12960\pi^2 m_{\varphi_1}^2}$
$Q_{qd}^{(1)}$	$\frac{g_Y^4}{25920\pi^2 m_{\varphi_1}^2}$
$Q_{lq}^{(3)}$	$-\frac{3\lambda_{\varphi_1} y_{\varphi_1}^{(i)\,2}}{16\pi^2 m_{\varphi_1}^2} - \frac{3 y_{\varphi_1}^{(i)\,2}}{8 m_{\varphi_1}^2}$
Q_{dd}	$-\frac{g_Y^4}{25920\pi^2 m_{\varphi_1}^2}$
Q_{eu}	$\frac{g_Y^4}{2160\pi^2 m_{\varphi_1}^2} + \frac{3\lambda_{\varphi_1} y_{\varphi_1}^{(ii)\,2}}{8\pi^2 m_{\varphi_1}^2} + \frac{3 y_{\varphi_1}^{(ii)\,2}}{4 m_{\varphi_1}^2}$
Q_{uu}	$-\frac{g_Y^4}{6480\pi^2 m_{\varphi_1}^2}$

TABLE XVII. Warsaw basis effective operators and the associated WCs that emerge after integrating out the heavy field φ_2: $(3,1,-\frac{4}{3})$. See Table III for color coding.

Dimension-six operators	Wilson coefficients
Q_H	$-\frac{\eta_{\varphi_2}^3}{32\pi^2 m_{\varphi_2}^2}$
Q_{HB}	$\frac{\eta_{\varphi_2} g_Y^2}{36\pi^2 m_{\varphi_2}^2}$
$Q_{H\Box}$	$-\frac{\eta_{\varphi_2}^2}{64\pi^2 m_{\varphi_2}^2}$
Q_{HG}	$\frac{g_S^2 \eta_{\varphi_2}}{384\pi^2 m_{\varphi_2}^2}$
$Q_{Hq}^{(1)}$	$-\frac{g_Y^4}{1080\pi^2 m_{\varphi_2}^2}$
Q_{HD}	$-\frac{g_Y^4}{180\pi^2 m_{\varphi_2}^2}$
Q_{Hd}	$\frac{g_Y^4}{540\pi^2 m_{\varphi_2}^2}$
Q_{He}	$\frac{g_Y^4}{180\pi^2 m_{\varphi_2}^2}$
$Q_{Hl}^{(1)}$	$\frac{g_Y^4}{360\pi^2 m_{\varphi_2}^2}$
Q_G	$\frac{g_S^3}{5760\pi^2 m_{\varphi_2}^2}$
Q_{Hu}	$-\frac{g_Y^4}{270\pi^2 m_{\varphi_2}^2}$
Q_{ll}	$-\frac{g_Y^4}{720\pi^2 m_{\varphi_2}^2}$
Q_{ee}	$-\frac{g_Y^4}{180\pi^2 m_{\varphi_2}^2}$
Q_{eu}	$\frac{g_Y^4}{135\pi^2 m_{\varphi_2}^2}$
$Q_{lq}^{(1)}$	$\frac{g_Y^4}{1080\pi^2 m_{\varphi_2}^2}$
$Q_{qq}^{(1)}$	$-\frac{g_Y^4}{6480\pi^2 m_{\varphi_2}^2}$
$Q_{qd}^{(1)}$	$\frac{g_Y^4}{1620\pi^2 m_{\varphi_2}^2}$
$Q_{qu}^{(1)}$	$-\frac{g_Y^4}{810\pi^2 m_{\varphi_2}^2}$
Q_{dd}	$-\frac{g_Y^4}{1620\pi^2 m_{\varphi_2}^2}$
Q_{ed}	$-\frac{g_Y^4}{270\pi^2 m_{\varphi_2}^2} + \frac{3\lambda_{\varphi_2} y_{\varphi_2}^2}{8\pi^2 m_{\varphi_2}^2} + \frac{3 y_{\varphi_2}^2}{4 m_{\varphi_2}^2}$
Q_{uu}	$-\frac{g_Y^4}{405\pi^2 m_{\varphi_2}^2}$
$Q_{qd}^{(8)}$	$-\frac{g_S^4}{960\pi^2 m_{\varphi_2}^2}$
$Q_{qu}^{(8)}$	$-\frac{g_S^4}{960\pi^2 m_{\varphi_2}^2}$
Q_{ld}	$-\frac{g_Y^4}{540\pi^2 m_{\varphi_2}^2}$
Q_{le}	$-\frac{g_Y^4}{180\pi^2 m_{\varphi_2}^2}$
Q_{lu}	$\frac{g_Y^4}{270\pi^2 m_{\varphi_2}^2}$
Q_{qe}	$\frac{g_Y^4}{540\pi^2 m_{\varphi_2}^2}$
$Q_{ud}^{(1)}$	$\frac{g_Y^4}{405\pi^2 m_{\varphi_2}^2}$
$Q_{ud}^{(8)}$	$-\frac{g_S^4}{960\pi^2 m_{\varphi_2}^2}$

TABLE XVIII. Warsaw basis effective operators and the associated WCs that emerge after integrating out the heavy field Θ_2: $(3,2,\frac{7}{6})$. See Table III for color coding.

Dimension-six operators	Wilson coefficients
Q_{dH}	$\frac{\eta_{\Theta_2}^{(2)2} Y_d^{SM}}{256\pi^2 m_{\Theta_2}^2}$
Q_{eH}	$\frac{\eta_{\Theta_2}^{(2)2} Y_e^{SM}}{256\pi^2 m_{\Theta_2}^2}$
Q_H	$-\frac{\eta_{\Theta_2}^{(1)3}}{16\pi^2 m_{\Theta_2}^2} - \frac{3\eta_{\Theta_2}^{(1)}\eta_{\Theta_2}^{(2)2}}{256\pi^2 m_{\Theta_2}^2} + \frac{\eta_{\Theta_2}^{(2)2}\lambda_H^{SM}}{128\pi^2 m_{\Theta_2}^2}$
Q_{HB}	$\frac{49 g_Y^2 \eta_{\Theta_2}^{(1)}}{1152\pi^2 m_{\Theta_2}^2}$
$Q_{H\Box}$	$-\frac{g_W^4}{2560\pi^2 m_{\Theta_2}^2} - \frac{\eta_{\Theta_2}^{(1)2}}{32\pi^2 m_{\Theta_2}^2} + \frac{\eta_{\Theta_2}^{(2)2}}{512\pi^2 m_{\Theta_2}^2}$
Q_{HD}	$-\frac{49 g_Y^4}{5760\pi^2 m_{\Theta_2}^2} - \frac{\eta_{\Theta_2}^{(2)2}}{128\pi^2 m_{\Theta_2}^2}$
Q_{HG}	$\frac{g_S^2 \eta_{\Theta_2}^{(1)}}{192\pi^2 m_{\Theta_2}^2}$
Q_{HW}	$\frac{g_W^2 \eta_{\Theta_2}^{(1)}}{128\pi^2 m_{\Theta_2}^2}$
Q_{HWB}	$\frac{7 g_W g_Y \eta_{\Theta_2}^{(2)}}{768\pi^2 m_{\Theta_2}^2}$
Q_G	$\frac{g_S^3}{2880\pi^2 m_{\Theta_2}^2}$
Q_{Hu}	$-\frac{49 g_Y^4}{8640\pi^2 m_{\Theta_2}^2}$
Q_{Hd}	$\frac{49 g_Y^4}{17280\pi^2 m_{\Theta_2}^2}$
Q_{He}	$\frac{49 g_Y^4}{5760\pi^2 m_{\Theta_2}^2}$
$Q_{Hl}^{(1)}$	$\frac{49 g_Y^4}{11520\pi^2 m_{\Theta_2}^2}$
$Q_{Hq}^{(1)}$	$-\frac{49 g_Y^4}{34560\pi^2 m_{\Theta_2}^2}$
$Q_{Hl}^{(3)}$	$-\frac{g_W^4}{640\pi^2 m_{\Theta_2}^2}$
$Q_{Hq}^{(3)}$	$-\frac{g_W^4}{640\pi^2 m_{\Theta_2}^2}$
Q_{ll}	$-\frac{g_W^4}{2560\pi^2 m_{\Theta_2}^2} - \frac{49 g_Y^4}{23040\pi^2 m_{\Theta_2}^2}$
Q_{ld}	$-\frac{49 g_Y^4}{17280\pi^2 m_{\Theta_2}^2}$
Q_{qe}	$\frac{49 g_Y^4}{17280\pi^2 m_{\Theta_2}^2} - \frac{9(4\lambda_{\Theta_2}^{(1)}+\lambda_{\Theta_2}^{(2)}) y_{\Theta_2}^{(1)2}}{128\pi^2 m_{\Theta_2}^2} - \frac{y_{\Theta_2}^{(1)2}}{4 m_{\Theta_2}^2}$
Q_{le}	$-\frac{49 g_Y^4}{5760\pi^2 m_{\Theta_2}^2}$
Q_{lu}	$\frac{49 g_Y^4}{8640\pi^2 m_{\Theta_2}^2} - \frac{9(4\lambda_{\Theta_2}^{(1)}+\lambda_{\Theta_2}^{(2)}) y_{\Theta_2}^{(2)2}}{128\pi^2 m_{\Theta_2}^2} - \frac{y_{\Theta_2}^{(2)2}}{4 m_{\Theta_2}^2}$
Q_{uH}	$\frac{\eta_{\Theta_2}^{(2)2} Y_u^{SM}}{256\pi^2 m_{\Theta_2}^2}$
Q_{uu}	$-\frac{49 g_Y^4}{12960\pi^2 m_{\Theta_2}^2}$
Q_W	$\frac{g_W^3}{1920\pi^2 m_{\Theta_2}^2}$
$Q_{qd}^{(8)}$	$-\frac{g_S^4}{480\pi^2 m_{\Theta_2}^2}$
$Q_{qu}^{(8)}$	$-\frac{g_S^4}{480\pi^2 m_{\Theta_2}^2}$
$Q_{lq}^{(1)}$	$\frac{49 g_Y^4}{34560\pi^2 m_{\Theta_2}^2}$
$Q_{qd}^{(1)}$	$\frac{49 g_Y^4}{51840\pi^2 m_{\Theta_2}^2}$
$Q_{qq}^{(1)}$	$-\frac{49 g_Y^4}{207360\pi^2 m_{\Theta_2}^2}$
$Q_{qu}^{(1)}$	$-\frac{49 g_Y^4}{25920\pi^2 m_{\Theta_2}^2}$
$Q_{ud}^{(1)}$	$\frac{49 g_Y^4}{12960\pi^2 m_{\Theta_2}^2}$
$Q_{lq}^{(3)}$	$-\frac{g_W^4}{1280\pi^2 m_{\Theta_2}^2}$
$Q_{qq}^{(3)}$	$-\frac{g_W^4}{2560\pi^2 m_{\Theta_2}^2}$
Q_{dd}	$-\frac{49 g_Y^4}{51840\pi^2 m_{\Theta_2}^2}$
Q_{ed}	$-\frac{49 g_Y^4}{8640\pi^2 m_{\Theta_2}^2}$
Q_{ee}	$-\frac{49 g_Y^4}{5760\pi^2 m_{\Theta_2}^2}$
Q_{eu}	$\frac{49 g_Y^4}{4320\pi^2 m_{\Theta_2}^2}$
$Q_{ud}^{(8)}$	$-\frac{g_S^4}{480\pi^2 m_{\Theta_2}^2}$

$$\mathcal{L}_{\Theta_2} = \mathcal{L}_{SM}^{d\le 4} + (D_\mu \Theta_2)^\dagger (D^\mu \Theta_2) - m_{\Theta_2}^2 \Theta_2^\dagger \Theta_2 - \eta_{\Theta_2}^{(1)} H^\dagger H \Theta_2^\dagger \Theta_2 - \eta_{\Theta_2}^{(2)} (H^\dagger \sigma^i H)(\Theta_2^\dagger \sigma^i \Theta_2) - \lambda_{\Theta_2}^{(1)} (\Theta_2^\dagger \Theta_2)^2 - \lambda_{\Theta_2}^{(2)} (\Theta_2^\dagger \sigma^i \Theta_2)^2 + \{ y_{\Theta_2}^{(1)} \Theta_2^\alpha \bar{q}_L^\alpha e_R + y_{\Theta_2}^{(2)} \Theta_2^\alpha \bar{u}_R^\alpha l_L + \text{H.c.} \}. \quad \text{(B11)}$$

Here m_{Θ_2} is the mass of the heavy field. This model contains six BSM parameters $(\eta_{\Theta_2}^{(1)}, \eta_{\Theta_2}^{(2)}, \lambda_{\Theta_2}^{(1)}, \lambda_{\Theta_2}^{(2)}, y_{\Theta_2}^{(1)}, y_{\Theta_2}^{(2)})$ and the WCs are functions of these parameters along with the SM ones; see Table XVIII.

d. Complex color triplet, isospin triplet: $\Omega \equiv (\mathbf{3}_C, \mathbf{3}_L, -\frac{1}{3}|_Y)$

In this model we extend the SM by a color-triplet isospin-triplet scalar (Ω) with hypercharge $Y = -\frac{1}{3}$. The Lagrangian involving the heavy field is written as [127,128]

$$\mathcal{L}_\Omega = \mathcal{L}_{SM}^{d\le 4} + (D_\mu \Omega)^\dagger (D^\mu \Omega) - m_\Omega^2 \Omega^\dagger \Omega - \eta_\Omega^{(1)} H^\dagger H \Omega^\dagger \Omega - \eta_\Omega^{(2)} (H^\dagger \sigma^i H)(\Omega^\dagger T_{adj}^i \Omega) - \lambda_\Omega^{(1)} (\Omega^\dagger \Omega)^2 - \lambda_\Omega^{(2)} (\Omega^\dagger T_{adj}^i \Omega)^2 - \lambda_\Omega^{(3)} (\Omega^\dagger \lambda^A \Omega)^2 + \{ y_\Omega \Omega^\alpha q_L^{\alpha T} C l_L + \text{H.c.} \}. \quad \text{(B12)}$$

Here the λ^A's are the $SU(3)_C$ generators, and m_Ω is the mass of the heavy field. This model contains six BSM

TABLE XIX. Warsaw basis effective operators and the associated WCs that emerge after integrating out the heavy field Ω: $(3,3,-\frac{1}{3})$. See Table III for color coding.

Dimension-six operators	Wilson coefficients
Q_{dH}	$\frac{\eta_\Omega^{(2)2} Y_d^{SM}}{64\pi^2 m_\Omega^2}$
Q_{eH}	$\frac{\eta_\Omega^{(2)2} Y_e^{SM}}{64\pi^2 m_\Omega^2}$
Q_H	$-\frac{3\eta_\Omega^{(1)3}}{32\pi^2 m_\Omega^2} - \frac{3\eta_\Omega^{(1)}\eta_\Omega^{(2)2}}{64\pi^2 m_\Omega^2} + \frac{\eta_\Omega^{(2)2}\lambda_H^{SM}}{32\pi^2 m_\Omega^2}$
Q_{HB}	$\frac{g_Y^2 \eta_\Omega^{(1)}}{192\pi^2 m_\Omega^2}$
$Q_{H\Box}$	$-\frac{g_W^4}{640\pi^2 m_\Omega^2} - \frac{3\eta_\Omega^{(1)2}}{64\pi^2 m_\Omega^2} + \frac{\eta_\Omega^{(2)2}}{128\pi^2 m_\Omega^2}$
Q_{HD}	$-\frac{g_Y^4}{960\pi^2 m_\Omega^2} - \frac{\eta_\Omega^{(2)2}}{32\pi^2 m_\Omega^2}$
Q_{HG}	$\frac{g_S^2 \eta_\Omega^{(1)}}{128\pi^2 m_\Omega^2}$
Q_{HW}	$\frac{g_W^2 \eta_\Omega^{(1)}}{32\pi^2 m_\Omega^2}$
Q_{HWB}	$\frac{g_W g_Y \eta_\Omega^{(2)}}{96\pi^2 m_\Omega^2}$
Q_{uH}	$\frac{\eta_\Omega^{(2)2} Y_u^{SM}}{64\pi^2 m_\Omega^2}$
$Q_{Hl}^{(1)}$	$\frac{g_Y^4}{1920\pi^2 m_\Omega^2}$
$Q_{Hq}^{(1)}$	$-\frac{g_Y^4}{5760\pi^2 m_\Omega^2}$
$Q_{Hl}^{(3)}$	$-\frac{g_W^4}{160\pi^2 m_\Omega^2}$
$Q_{Hq}^{(3)}$	$-\frac{g_W^4}{160\pi^2 m_\Omega^2}$
Q_{ll}	$-\frac{g_W^4}{640\pi^2 m_\Omega^2} - \frac{g_Y^4}{3840\pi^2 m_\Omega^2}$
Q_{Hu}	$-\frac{g_Y^4}{1440\pi^2 m_\Omega^2}$
Q_{Hd}	$\frac{g_Y^4}{2880\pi^2 m_\Omega^2}$
Q_{He}	$\frac{g_Y^4}{960\pi^2 m_\Omega^2}$
Q_W	$\frac{g_W^3}{480\pi^2 m_\Omega^2}$
Q_G	$\frac{g_S^3}{1920\pi^2 m_\Omega^2}$
$Q_{lq}^{(3)}$	$-\frac{g_W^4}{320\pi^2 m_\Omega^2} + \frac{(15\lambda_\Omega^{(1)}+3\lambda_\Omega^{(2)}+2\lambda_\Omega^{(3)})y_\Omega^2}{32\pi^2 m_\Omega^2} + \frac{3y_\Omega^2}{8m_\Omega^2}$
$Q_{qq}^{(3)}$	$-\frac{g_W^4}{640\pi^2 m_\Omega^2}$
Q_{dd}	$-\frac{g_Y^4}{8640\pi^2 m_\Omega^2}$
Q_{ed}	$-\frac{g_Y^4}{1440\pi^2 m_\Omega^2}$
Q_{ee}	$-\frac{g_Y^4}{960\pi^2 m_\Omega^2}$
Q_{eu}	$\frac{g_Y^4}{720\pi^2 m_\Omega^2}$
$Q_{ud}^{(8)}$	$-\frac{g_S^4}{320\pi^2 m_\Omega^2}$
$Q_{lq}^{(1)}$	$\frac{(15\lambda_\Omega^{(1)}+3\lambda_\Omega^{(2)}+2\lambda_\Omega^{(3)})y_\Omega^2}{8\pi^2 m_\Omega^2} + \frac{3y_\Omega^2}{2m_\Omega^2} + \frac{g_Y^4}{5760\pi^2 m_\Omega^2}$
$Q_{qd}^{(1)}$	$\frac{g_Y^4}{8640\pi^2 m_\Omega^2}$
$Q_{qq}^{(1)}$	$-\frac{g_Y^4}{34560\pi^2 m_\Omega^2}$
$Q_{qu}^{(1)}$	$-\frac{g_Y^4}{4320\pi^2 m_\Omega^2}$
$Q_{ud}^{(1)}$	$\frac{g_Y^4}{2160\pi^2 m_\Omega^2}$
Q_{ld}	$-\frac{g_Y^4}{2880\pi^2 m_\Omega^2}$
Q_{le}	$-\frac{g_Y^4}{960\pi^2 m_\Omega^2}$
Q_{lu}	$\frac{g_Y^4}{1440\pi^2 m_\Omega^2}$
Q_{qe}	$\frac{g_Y^4}{2880\pi^2 m_\Omega^2}$
Q_{uu}	$-\frac{g_Y^4}{2160\pi^2 m_\Omega^2}$
$Q_{qu}^{(8)}$	$-\frac{g_S^4}{320\pi^2 m_\Omega^2}$
$Q_{qd}^{(8)}$	$-\frac{g_S^4}{320\pi^2 m_\Omega^2}$

parameters ($\eta_\Omega^{(1)}$, $\eta_\Omega^{(2)}$, $\lambda_\Omega^{(1)}$, $\lambda_\Omega^{(2)}$, $\lambda_\Omega^{(3)}$, y_Ω) and the WCs are functions of these parameters along with the SM ones; see Table XIX.

e. Complex color sextet, isospin triplet: $\chi_1 \equiv (\mathbf{6}_C, \mathbf{3}_L, \frac{1}{3}|_Y)$

In this model we extend the SM by a color-sextet isospin-triplet scalar (χ_1) with hypercharge $Y = \frac{1}{3}$. The Lagrangian involving the heavy field is written as [132,177]

$$\begin{aligned}\mathcal{L}_{\chi_1} = \mathcal{L}_{SM}^{d\leq 4} &+ \mathrm{Tr}[(D_\mu \chi_1)^\dagger (D^\mu \chi_1)] - m_{\chi_1}^2 \mathrm{Tr}[\chi_1^\dagger \chi_1] \\ &- \eta_{\chi_1}^{(1)} H^\dagger H \mathrm{Tr}[\chi_1^\dagger \chi_1] - \eta_{\chi_1}^{(2)} (H^\dagger \sigma^i H)\mathrm{Tr}[(\chi_1^\dagger \sigma^i \chi_1)] \\ &- \lambda_{\chi_1}^{(1)} (\mathrm{Tr}[\chi_1^\dagger \chi_1])^2 - \lambda_{\chi_1}^{(2)} \mathrm{Tr}[(\chi_1^\dagger \chi_1)^2] \\ &- \{ y_{\chi_1} (q_L^{\{A|})^T C (\chi_1^{AB,I})^\dagger i\sigma^2 q_L^{|B\}} + \mathrm{H.c.}\}. \end{aligned} \tag{B13}$$

Here m_{χ_1} is the mass of the heavy field. This model contains five BSM parameters ($\eta_{\chi_1}^{(1)}$, $\eta_{\chi_1}^{(2)}$, $\lambda_{\chi_1}^{(1)}$, $\lambda_{\chi_1}^{(2)}$, y_{χ_1}) and the WCs are functions of these parameters along with the SM ones; see Table XX.

f. Complex color sextet, isospin singlet: $\chi_2 \equiv (\mathbf{6}_C, \mathbf{1}_L, \frac{4}{3}|_Y)$

Here we extend the SM by a color-sextet isospin-singlet scalar (χ_2) with hypercharge $Y = \frac{4}{3}$. The Lagrangian involving the heavy field is written as [132,177]

$$\begin{aligned}\mathcal{L}_{\chi_2} = \mathcal{L}_{SM}^{d\leq 4} &+ (D_\mu \chi_2)^\dagger (D^\mu \chi_2) - m_{\chi_2}^2 \chi_2^\dagger \chi_2 \\ &- \eta_{\chi_2} H^\dagger H \chi_2^\dagger \chi_2 - \lambda_{\chi_2} (\chi_2^\dagger \chi_2)^2 \\ &- \{ y_{\chi_2} (u_R^{\{A|})^T C (\chi_2^{AB})^\dagger u_R^{|B\}} + \mathrm{H.c.}\}. \end{aligned} \tag{B14}$$

TABLE XX. Warsaw basis effective operators and the associated WCs that emerge after integrating out the heavy field χ_1: $(6,3,\frac{1}{3})$. See Table III for color coding.

Dimension-six operators	Wilson coefficients
Q_H	$-\frac{\eta_{\chi_1}^{(1)3}}{16\pi^2 m_{\chi_1}^2}-\frac{3\eta_{\chi_1}^{(1)}\eta_{\chi_1}^{(2)2}}{64\pi^2 m_{\chi_1}^2}+\frac{\eta_{\chi_1}^{(2)2}\lambda_H^{\rm SM}}{16\pi^2 m_{\chi_1}^2}$
$Q_{H\Box}$	$-\frac{g_W^4}{320\pi^2 m_{\chi_1}^2}-\frac{\eta_{\chi_1}^{(1)2}}{32\pi^2 m_{\chi_1}^2}+\frac{\eta_{\chi_1}^{(2)2}}{64\pi^2 m_{\chi_1}^2}$
Q_{HD}	$-\frac{g_Y^4}{480\pi^2 m_{\chi_1}^2}-\frac{\eta_{\chi_1}^{(2)2}}{16\pi^2 m_{\chi_1}^2}$
Q_{eH}	$\frac{\eta_{\chi_1}^{(2)2}Y_e^{\rm SM}}{32\pi^2 m_{\chi_1}^2}$
Q_{uH}	$\frac{\eta_{\chi_1}^{(2)2}Y_u^{\rm SM}}{32\pi^2 m_{\chi_1}^2}$
Q_{dH}	$\frac{\eta_{\chi_1}^{(2)2}Y_d^{\rm SM}}{32\pi^2 m_{\chi_1}^2}$
Q_{HG}	$\frac{g_S^2\eta_{\chi_1}^{(1)}}{192\pi^2 m_{\chi_1}^2}$
Q_{HW}	$\frac{\eta_{\chi_1}^{(1)}g_W^2}{32\pi^2 m_{\chi_1}^2}$
Q_{HWB}	$\frac{\eta_{\chi_1}^{(2)}g_W g_Y}{48\pi^2 m_{\chi_1}^2}$
Q_{HB}	$\frac{\eta_{\chi_1}^{(1)}g_Y^2}{288\pi^2 m_{\chi_1}^2}$
Q_{Hd}	$\frac{g_Y^4}{1440\pi^2 m_{\chi_1}^2}$
Q_{He}	$\frac{g_Y^4}{480\pi^2 m_{\chi_1}^2}$
$Q_{Hl}^{(1)}$	$\frac{g_Y^4}{960\pi^2 m_{\chi_1}^2}$
$Q_{Hq}^{(1)}$	$-\frac{g_Y^4}{2880\pi^2 m_{\chi_1}^2}$
$Q_{Hl}^{(3)}$	$-\frac{g_W^4}{80\pi^2 m_{\chi_1}^2}$
$Q_{Hq}^{(3)}$	$-\frac{g_W^4}{80\pi^2 m_{\chi_1}^2}$
Q_{ll}	$-\frac{g_W^4}{320\pi^2 m_{\chi_1}^2}-\frac{g_Y^4}{1920\pi^2 m_{\chi_1}^2}$
Q_{Hu}	$-\frac{g_Y^4}{720\pi^2 m_{\chi_1}^2}$
Q_G	$\frac{g_S^3}{960\pi^2 m_{\chi_1}^2}$
Q_W	$\frac{g_W^3}{240\pi^2 m_{\chi_1}^2}$
$Q_{lq}^{(1)}$	$\frac{g_Y^4}{2880\pi^2 m_{\chi_1}^2}$
$Q_{qd}^{(1)}$	$\frac{g_Y^4}{4320\pi^2 m_{\chi_1}^2}$
$Q_{qq}^{(1)}$	$-\frac{g_Y^4}{17280\pi^2 m_{\chi_1}^2}+\frac{3y_{\chi_1}^2}{m_{\chi_1}^2}+\frac{(12\lambda_{\chi_1}^{(1)}+3\lambda_{\chi_1}^{(2)})y_{\chi_1}^2}{2\pi^2 m_{\chi_1}^2}$
$Q_{qu}^{(1)}$	$-\frac{g_Y^4}{2160\pi^2 m_{\chi_1}^2}$
Q_{dd}	$-\frac{g_Y^4}{4320\pi^2 m_{\chi_1}^2}$
Q_{uu}	$-\frac{g_Y^4}{1080\pi^2 m_{\chi_1}^2}$
$Q_{ud}^{(1)}$	$\frac{g_Y^4}{1080\pi^2 m_{\chi_1}^2}$
$Q_{lq}^{(3)}$	$-\frac{g_W^4}{160\pi^2 m_{\chi_1}^2}$
$Q_{qq}^{(3)}$	$-\frac{g_W^4}{320\pi^2 m_{\chi_1}^2}+\frac{3y_{\chi_1}^2}{4m_{\chi_1}^2}+\frac{(12\lambda_{\chi_1}^{(1)}+3\lambda_{\chi_1}^{(2)})y_{\chi_1}^2}{8\pi^2 m_{\chi_1}^2}$
Q_{qe}	$\frac{g_Y^4}{1440\pi^2 m_{\chi_1}^2}$
Q_{ed}	$-\frac{g_Y^4}{720\pi^2 m_{\chi_1}^2}$
Q_{ee}	$-\frac{g_Y^4}{480\pi^2 m_{\chi_1}^2}$
Q_{eu}	$\frac{g_Y^4}{360\pi^2 m_{\chi_1}^2}$
Q_{ld}	$-\frac{g_Y^4}{1440\pi^2 m_{\chi_1}^2}$
Q_{le}	$-\frac{g_Y^4}{480\pi^2 m_{\chi_1}^2}$
Q_{lu}	$\frac{g_Y^4}{720\pi^2 m_{\chi_1}^2}$
$Q_{qu}^{(8)}$	$-\frac{g_S^4}{160\pi^2 m_{\chi_1}^2}$
$Q_{qd}^{(8)}$	$-\frac{g_S^4}{160\pi^2 m_{\chi_1}^2}$
$Q_{ud}^{(8)}$	$-\frac{g_S^4}{160\pi^2 m_{\chi_1}^2}$

Here m_{χ_2} is the mass of the heavy field. This model contains three BSM parameters $(\eta_{\chi_2}, \lambda_{\chi_2}, y_{\chi_2})$ and the WCs are functions of these parameters along with the SM ones; see Table XXI.

g. Complex color sextet, isospin singlet: $\chi_3 \equiv (\mathbf{6_C}, \mathbf{1_L}, -\frac{2}{3}|_Y)$

Here we extend the SM by a color-sextet isospin-singlet scalar (χ_3) with hypercharge $Y=-\frac{2}{3}$. The Lagrangian involving the heavy field is written as [132,177]

$$\begin{aligned}\mathcal{L}_{\chi_3} &= \mathcal{L}_{\rm SM}^{d\le 4} + (D_\mu\chi_3)^\dagger(D^\mu\chi_3) - m_{\chi_3}^2\chi_3^\dagger\chi_3 \\ &\quad - \eta_{\chi_3}H^\dagger H\chi_3^\dagger\chi_3 - \lambda_{\chi_3}(\chi_3^\dagger\chi_3)^2 \\ &\quad - \{y_{\chi_3}(d_R^{\{A|})^T C(\chi_3^{AB})^\dagger d_R^{|B\}} + \text{H.c.}\}. \end{aligned} \tag{B15}$$

Here m_{χ_3} is the mass of the heavy field. This model contains three BSM parameters $(\eta_{\chi_3}, \lambda_{\chi_3}, y_{\chi_3})$ and the WCs are functions of these parameters along with the SM ones; see Table XXII.

h. Complex color sextet, isospin singlet: $\chi_4 \equiv (\mathbf{6_C}, \mathbf{1_L}, \frac{1}{3}|_Y)$

Here we extend the SM by a color-sextet isospin-singlet scalar (χ_4) with hypercharge $Y=\frac{1}{3}$. The Lagrangian involving the heavy field is written as [132,177]

TABLE XXI. Warsaw basis effective operators and the associated WCs that emerge after integrating out the heavy field χ_2: $(6,1,\frac{4}{3})$. See Table III for color coding.

Dimension-six operators	Wilson coefficients
Q_H	$-\frac{\eta_{\chi_2}^3}{16\pi^2 m_{\chi_2}^2}$
Q_{HB}	$\frac{\eta_{\chi_2} g_Y^2}{18\pi^2 m_{\chi_2}^2}$
$Q_{H\Box}$	$-\frac{\eta_{\chi_2}^2}{32\pi^2 m_{\chi_2}^2}$
Q_{HG}	$\frac{g_S^2 \eta_{\chi_2}}{192\pi^2 m_{\chi_2}^2}$
Q_{HD}	$-\frac{g_Y^4}{90\pi^2 m_{\chi_2}^2}$
Q_{Hd}	$\frac{g_Y^4}{270\pi^2 m_{\chi_2}^2}$
Q_{He}	$\frac{g_Y^4}{90\pi^2 m_{\chi_2}^2}$
Q_{Hu}	$-\frac{g_Y^4}{135\pi^2 m_{\chi_2}^2}$
Q_{ll}	$-\frac{g_Y^4}{360\pi^2 m_{\chi_2}^2}$
$Q_{Hl}^{(1)}$	$\frac{g_Y^4}{180\pi^2 m_{\chi_2}^2}$
$Q_{Hq}^{(1)}$	$-\frac{g_Y^4}{540\pi^2 m_{\chi_2}^2}$
Q_G	$\frac{g_S^3}{2880\pi^2 m_{\chi_2}^2}$
$Q_{ud}^{(8)}$	$-\frac{g_S^4}{480\pi^2 m_{\chi_2}^2}$
$Q_{qu}^{(8)}$	$-\frac{g_S^4}{480\pi^2 m_{\chi_2}^2}$
$Q_{qd}^{(8)}$	$-\frac{g_S^4}{480\pi^2 m_{\chi_2}^2}$
$Q_{lq}^{(1)}$	$\frac{g_Y^4}{540\pi^2 m_{\chi_2}^2}$
$Q_{qd}^{(1)}$	$\frac{g_Y^4}{810\pi^2 m_{\chi_2}^2}$
$Q_{qq}^{(1)}$	$-\frac{g_Y^4}{3240\pi^2 m_{\chi_2}^2}$
$Q_{qu}^{(1)}$	$-\frac{g_Y^4}{405\pi^2 m_{\chi_2}^2}$
$Q_{ud}^{(1)}$	$\frac{2g_Y^4}{405\pi^2 m_{\chi_2}^2}$
Q_{dd}	$-\frac{g_Y^4}{810\pi^2 m_{\chi_2}^2}$
Q_{ed}	$-\frac{g_Y^4}{135\pi^2 m_{\chi_2}^2}$
Q_{ee}	$-\frac{g_Y^4}{90\pi^2 m_{\chi_2}^2}$
Q_{eu}	$\frac{2g_Y^4}{135\pi^2 m_{\chi_2}^2}$
Q_{ld}	$-\frac{g_Y^4}{270\pi^2 m_{\chi_2}^2}$
Q_{le}	$-\frac{g_Y^4}{90\pi^2 m_{\chi_2}^2}$
Q_{lu}	$\frac{g_Y^4}{135\pi^2 m_{\chi_2}^2}$
Q_{qe}	$\frac{g_Y^4}{270\pi^2 m_{\chi_2}^2}$
Q_{uu}	$-\frac{2g_Y^4}{405\pi^2 m_{\chi_2}^2}$
	$+\frac{3y_{\chi_2}^2}{2m_{\chi_2}^2}+\frac{3\lambda_{\chi_2} y_{\chi_2}^2}{8\pi^2 m_{\chi_2}^2}$

TABLE XXII. Warsaw basis effective operators and the associated WCs that emerge after integrating out the heavy field χ_3: $(6,1,-\frac{2}{3})$. See Table III for color coding.

Dimension-six operators	Wilson coefficients
Q_H	$-\frac{\eta_{\chi_3}^3}{16\pi^2 m_{\chi_3}^2}$
Q_{HB}	$\frac{\eta_{\chi_3} g_Y^2}{72\pi^2 m_{\chi_3}^2}$
Q_{HG}	$\frac{g_S^2 \eta_{\chi_3}}{192\pi^2 m_{\chi_3}^2}$
$Q_{H\Box}$	$-\frac{\eta_{\chi_3}^2}{32\pi^2 m_{\chi_3}^2}$
Q_{HD}	$-\frac{g_Y^4}{360\pi^2 m_{\chi_3}^2}$
$Q_{Hl}^{(1)}$	$\frac{g_Y^4}{720\pi^2 m_{\chi_3}^2}$
$Q_{Hq}^{(1)}$	$-\frac{g_Y^4}{2160\pi^2 m_{\chi_3}^2}$
Q_G	$\frac{g_S^3}{2880\pi^2 m_{\chi_3}^2}$
Q_{Hd}	$\frac{g_Y^4}{1080\pi^2 m_{\chi_3}^2}$
Q_{He}	$\frac{g_Y^4}{360\pi^2 m_{\chi_3}^2}$
Q_{Hu}	$-\frac{g_Y^4}{540\pi^2 m_{\chi_3}^2}$
Q_{ll}	$-\frac{g_Y^4}{1440\pi^2 m_{\chi_3}^2}$
$Q_{qu}^{(8)}$	$-\frac{g_S^4}{480\pi^2 m_{\chi_3}^2}$
$Q_{qd}^{(8)}$	$-\frac{g_S^4}{480\pi^2 m_{\chi_3}^2}$
$Q_{ud}^{(8)}$	$-\frac{g_S^4}{480\pi^2 m_{\chi_3}^2}$
$Q_{lq}^{(1)}$	$\frac{g_Y^4}{2160\pi^2 m_{\chi_3}^2}$
$Q_{qd}^{(1)}$	$\frac{g_Y^4}{3240\pi^2 m_{\chi_3}^2}$
$Q_{qq}^{(1)}$	$-\frac{g_Y^4}{12960\pi^2 m_{\chi_3}^2}$
$Q_{qu}^{(1)}$	$-\frac{g_Y^4}{1620\pi^2 m_{\chi_3}^2}$
$Q_{ud}^{(1)}$	$\frac{g_Y^4}{810\pi^2 m_{\chi_3}^2}$
Q_{dd}	$-\frac{g_Y^4}{3240\pi^2 m_{\chi_3}^2}$
	$+\frac{3y_{\chi_3}^2}{2m_{\chi_3}^2}+\frac{3\lambda_{\chi_3} y_{\chi_3}^2}{8\pi^2 m_{\chi_3}^2}$
Q_{ed}	$-\frac{g_Y^4}{540\pi^2 m_{\chi_3}^2}$
Q_{ee}	$-\frac{g_Y^4}{360\pi^2 m_{\chi_3}^2}$
Q_{eu}	$\frac{g_Y^4}{270\pi^2 m_{\chi_3}^2}$
Q_{ld}	$-\frac{g_Y^4}{1080\pi^2 m_{\chi_3}^2}$
Q_{le}	$-\frac{g_Y^4}{360\pi^2 m_{\chi_3}^2}$
Q_{lu}	$\frac{g_Y^4}{540\pi^2 m_{\chi_3}^2}$
Q_{qe}	$\frac{g_Y^4}{1080\pi^2 m_{\chi_3}^2}$
Q_{uu}	$-\frac{g_Y^4}{810\pi^2 m_{\chi_3}^2}$

TABLE XXIII. Warsaw basis effective operators and the associated WCs that emerge after integrating out the heavy field χ_4: $(6, 1, \frac{1}{3})$. See Table III for color coding.

Dimension-six operators	Wilson coefficients
$\mathcal{Q}_H$	$-\frac{\eta_{\chi_4}^3}{16\pi^2 m_{\chi_4}^2}$
$\mathcal{Q}_{HB}$	$\frac{\eta_{\chi_4} g_Y^2}{288\pi^2 m_{\chi_4}^2}$
$\mathcal{Q}_{H\Box}$	$-\frac{\eta_{\chi_4}^2}{32\pi^2 m_{\chi_4}^2}$
$\mathcal{Q}_{HG}$	$\frac{g_S^2 \eta_{\chi_4}}{192\pi^2 m_{\chi_4}^2}$
$\mathcal{Q}_{HD}$	$-\frac{g_Y^4}{1440\pi^2 m_{\chi_4}^2}$
$\mathcal{Q}_G$	$\frac{g_S^3}{2880\pi^2 m_{\chi_4}^2}$
$\mathcal{Q}_{Hd}$	$\frac{g_Y^4}{4320\pi^2 m_{\chi_4}^2}$
$\mathcal{Q}_{He}$	$\frac{g_Y^4}{1440\pi^2 m_{\chi_4}^2}$
$\mathcal{Q}_{Hu}$	$-\frac{g_Y^4}{2160\pi^2 m_{\chi_4}^2}$
$\mathcal{Q}_{Hl}^{(1)}$	$\frac{g_Y^4}{2880\pi^2 m_{\chi_4}^2}$
$\mathcal{Q}_{Hq}^{(1)}$	$-\frac{g_Y^4}{8640\pi^2 m_{\chi_4}^2}$
$\mathcal{Q}_{ll}$	$-\frac{g_Y^4}{5760\pi^2 m_{\chi_4}^2}$
$\mathcal{Q}_{ld}$	$-\frac{g_Y^4}{4320\pi^2 m_{\chi_4}^2}$
$\mathcal{Q}_{le}$	$-\frac{g_Y^4}{1440\pi^2 m_{\chi_4}^2}$
$\mathcal{Q}_{lu}$	$\frac{g_Y^4}{2160\pi^2 m_{\chi_4}^2}$
$\mathcal{Q}_{qe}$	$\frac{g_Y^4}{4320\pi^2 m_{\chi_4}^2}$
$\mathcal{Q}_{quqd}^{(1)}$	$\frac{3y_{\chi_4}^{(i)} y_{\chi_4}^{(ii)}}{2m_{\chi_4}^2} + \frac{3\lambda_{\chi_4} y_{\chi_4}^{(i)} y_{\chi_4}^{(ii)}}{8\pi^2 m_{\chi_4}^2}$
$\mathcal{Q}_{uu}$	$-\frac{g_Y^4}{3240\pi^2 m_{\chi_4}^2}$
$\mathcal{Q}_{ee}$	$-\frac{g_Y^4}{1440\pi^2 m_{\chi_4}^2}$
$\mathcal{Q}_{lq}^{(1)}$	$\frac{g_Y^4}{8640\pi^2 m_{\chi_4}^2}$
$\mathcal{Q}_{qd}^{(1)}$	$\frac{g_Y^4}{12960\pi^2 m_{\chi_4}^2}$
$\mathcal{Q}_{qq}^{(1)}$	$-\frac{g_Y^4}{51840\pi^2 m_{\chi_4}^2} + \frac{3y_{\chi_4}^{(ii)2}}{2m_{\chi_4}^2} + \frac{3\lambda_{\chi_4} y_{\chi_4}^{(ii)2}}{8\pi^2 m_{\chi_4}^2}$
$\mathcal{Q}_{qu}^{(1)}$	$-\frac{g_Y^4}{6480\pi^2 m_{\chi_4}^2}$
$\mathcal{Q}_{ud}^{(1)}$	$\frac{g_Y^4}{3240\pi^2 m_{\chi_4}^2} + \frac{3y_{\chi_4}^{(i)2}}{2m_{\chi_4}^2} + \frac{3\lambda_{\chi_4} y_{\chi_4}^{(i)2}}{8\pi^2 m_{\chi_4}^2}$
$\mathcal{Q}_{dd}$	$-\frac{g_Y^4}{12960\pi^2 m_{\chi_4}^2}$
$\mathcal{Q}_{ed}$	$-\frac{g_Y^4}{2160\pi^2 m_{\chi_4}^2}$
$\mathcal{Q}_{eu}$	$\frac{g_Y^4}{1080\pi^2 m_{\chi_4}^2}$
$\mathcal{Q}_{ud}^{(8)}$	$-\frac{g_S^4}{480\pi^2 m_{\chi_4}^2} + \frac{y_{\chi_4}^{(i)2}}{2m_{\chi_4}^2} + \frac{\lambda_{\chi_4} y_{\chi_4}^{(i)2}}{8\pi^2 m_{\chi_4}^2}$
$\mathcal{Q}_{qu}^{(8)}$	$-\frac{g_S^4}{480\pi^2 m_{\chi_4}^2}$
$\mathcal{Q}_{qd}^{(8)}$	$-\frac{g_S^4}{480\pi^2 m_{\chi_4}^2}$
$\mathcal{Q}_{quqd}^{(8)}$	$\frac{y_{\chi_4}^{(i)} y_{\chi_4}^{(ii)}}{2m_{\chi_4}^2} + \frac{\lambda_{\chi_4} y_{\chi_4}^{(i)} y_{\chi_4}^{(ii)}}{8\pi^2 m_{\chi_4}^2}$

$$\begin{aligned}\mathcal{L}_{\chi_4} = \mathcal{L}_{\rm SM}^{d\le 4} &+ (D_\mu \chi_4)^\dagger (D^\mu \chi_4) - m_{\chi_4}^2 \chi_4^\dagger \chi_4 \\ &- \eta_{\chi_4} H^\dagger H \chi_4^\dagger \chi_4 - \lambda_{\chi_4} (\chi_4^\dagger \chi_4)^2 \\ &- \{ y_{\chi_4}^{(i)} (u_R^{\{A|})^T (\chi_4^{AB})^\dagger d_R^{|B\}} \\ &+ y_{\chi_4}^{(ii)} (q_L^{\{A|})^T C (\chi_4^{AB})^\dagger i\sigma^2 q_L^{|B\}} + \text{H.c.}\}. \end{aligned} \tag{B16}$$

Here m_{χ_4} is the mass of the heavy field. This model contains four BSM parameters (η_{χ_4}, λ_{χ_4}, $y_{\chi_4}^{(i)}$, $y_{\chi_4}^{(ii)}$) and the WCs are functions of these parameters along with the SM ones; see Table XXIII.

APPENDIX C: MORE INFORMATION ON MODEL-INDEPENDENT BAYESIAN ANALYSIS

1. Priors used

In this work, for most of the WCs, the uniform priors have the range $\{-10, 10\}$. Here we list only those WCs that have different ranges:

(1) For single WC fits:
   (a) For the fit titled "This Analysis," the prior range for $\mathcal{C}_H$ is $\{-40, 40\}$.
   (b) With "2020 Data," the WCs $\mathcal{C}_H$, $\mathcal{C}_{H\Box}$, $\mathcal{C}_{tH}$, and $\mathcal{C}_G$ have prior ranges $\{-100, 100\}$, $\{-70, 70\}$, $\{-50, 50\}$, and $\{-50, 50\}$ respectively.

(2) For global fits:
   (a) The "This Analysis" fit takes priors for $\mathcal{C}_H$, $\mathcal{C}_{H\Box}$, $\mathcal{C}_{tH}$, and $\mathcal{C}_G$, each with the range $\{-40, 40\}$.
   (b) In the "2020 Data" fit, the WCs with distinct priors are $\mathcal{C}_H$, $\mathcal{C}_{H\Box}$, $\mathcal{C}_{tH}$, and $\mathcal{C}_G$ with ranges $\{-100, 100\}$, $\{-70, 70\}$, $\{-50, 50\}$, and $\{-50, 50\}$, respectively.
   (c) In the case of the "W/O *ggF* STXS" fit, priors with the range $\{-40, 40\}$ are taken for $\mathcal{C}_H$, $\mathcal{C}_{H\Box}$, $\mathcal{C}_{tH}$, and $\mathcal{C}_G$ each.
   (d) For the "W/O *Vh* STXS" fit, priors with the range $\{-40, 40\}$ are taken for $\mathcal{C}_H$, $\mathcal{C}_{H\Box}$, $\mathcal{C}_{tH}$, and $\mathcal{C}_G$ each.
   (e) For the "W/O *WBF* STXS" measurements, $\mathcal{C}_H$, $\mathcal{C}_{cH}$, $\mathcal{C}_{H\Box}$, $\mathcal{C}_{tH}$ and $\mathcal{C}_G$ have the ranges $\{-100, 100\}$, $\{-50, 50\}$, $\{-200, 200\}$, $\{-40, 40\}$, and $\{-40, 40\}$, respectively.
   (f) For the "W/O *ggF*, $t\bar{t}h$ & *th* STXS" measurements, the accepted priors of $\mathcal{C}_H$, $\mathcal{C}_{H\Box}$, $\mathcal{C}_{tH}$, $\mathcal{C}_G$, $\mathcal{C}_{HG}$ and $\mathcal{C}_{tG}$ have the ranges $\{-200, 200\}$, $\{-40, 40\}$, $\{-1500, 1500\}$, $\{-2000, 2000\}$, $\{-100, 100\}$, and $\{-150, 150\}$, respectively.

2. Fit results and correlation matrix

TABLE XXIV. 95% credible intervals (CI) for one-parameter WC fits and for a global analysis of 23 WCs. The cutoff scale Λ is set to 1 TeV.

WCs	95% CI individual limits	95% CI global limits
$\mathcal{C}_{HWB}$	$[-0.0035, 0.0028]$	$[-0.19, 0.15]$
$\mathcal{C}_{HD}$	$[-0.022, 0.0042]$	$[-0.40, 0.39]$
$\mathcal{C}_{ll}$	$[-0.006, 0.016]$	$[-0.10, 0.00]$
$\mathcal{C}_{Hl}^{(1)}$	$[-0.005, 0.012]$	$[-0.08, 0.12]$
$\mathcal{C}_{Hl}^{(3)}$	$[-0.010, 0.003]$	$[-0.054, 0.063]$
$\mathcal{C}_{He}$	$[-0.013, 0.008]$	$[-0.20, 0.19]$
$\mathcal{C}_{Hq}^{(1)}$	$[-0.023, 0.047]$	$[-0.057, 0.096]$
$\mathcal{C}_{Hq}^{(3)}$	$[-0.008, 0.016]$	$[-0.033, 0.063]$
$\mathcal{C}_{Hd}$	$[-0.15, 0.04]$	$[-0.29, 0.11]$
$\mathcal{C}_{Hu}$	$[-0.056, 0.081]$	$[-0.13, 0.25]$
$\mathcal{C}_{H}$	$[-9.6, 6.9]$	$[-11., 7.0]$
$\mathcal{C}_{H\Box}$	$[-0.96, -0.13]$	$[-1.6, 5.6]$
$\mathcal{C}_{HG}$	$[-0.0038, -0.0002]$	$[-0.013, 0.010]$
$\mathcal{C}_{HW}$	$[-0.010, 0.005]$	$[-0.28, 0.12]$
$\mathcal{C}_{HB}$	$[-0.0031, 0.0016]$	$[-0.050, 0.061]$
$\mathcal{C}_{W}$	$[-0.17, 0.34]$	$[-0.18, 0.33]$
$\mathcal{C}_{G}$	$[-0.8, 1.2]$	$[-1.1, 1.3]$
$\mathcal{C}_{\mu H}$	$[-0.0042, 0.0027]$	$[-0.0045, 0.0025]$
$\mathcal{C}_{\tau H}$	$[-0.0040, 0.028]$	$[-0.009, 0.029]$
$\mathcal{C}_{bH}$	$[-0.036, 0.004]$	$[-0.029, 0.069]$
$\mathcal{C}_{cH}$	$[-0.15, -0.01]$	$[-1.1, 0.20]$
$\mathcal{C}_{tH}$	[0.02, 1.2]	$[-2.6, 2.6]$
$\mathcal{C}_{tG}$	$[-0.11, -0.01]$	$[-0.28, 0.21]$

TABLE XXV. Correlations among the 23 WCs with the fit results shown in the third column of Table XXIV.

	Correlations																						
WCs	$\mathcal{C}_{HWB}$	$\mathcal{C}_{HD}$	$\mathcal{C}_{ll}$	$\mathcal{C}_{Hl}^{(1)}$	$\mathcal{C}_{Hl}^{(3)}$	$\mathcal{C}_{He}$	$\mathcal{C}_{Hq}^{(1)}$	$\mathcal{C}_{Hq}^{(3)}$	$\mathcal{C}_{Hd}$	$\mathcal{C}_{Hu}$	$\mathcal{C}_{H}$	$\mathcal{C}_{H\Box}$	$\mathcal{C}_{HG}$	$\mathcal{C}_{HW}$	$\mathcal{C}_{HB}$	$\mathcal{C}_{W}$	$\mathcal{C}_{G}$	$\mathcal{C}_{\mu H}$	$\mathcal{C}_{\tau H}$	$\mathcal{C}_{bH}$	$\mathcal{C}_{cH}$	$\mathcal{C}_{tH}$	$\mathcal{C}_{tG}$
$\mathcal{C}_{HWB}$	1																						
$\mathcal{C}_{HD}$	−0.98	1																					
$\mathcal{C}_{ll}$	−0.03	0.06	1																				
$\mathcal{C}_{Hl}^{(1)}$	0.96	−0.98	−0.22	1																			
$\mathcal{C}_{Hl}^{(3)}$	0.09	−0.24	0.31	0.17	1																		
$\mathcal{C}_{He}$	0.98	−1.00	−0.07	0.98	0.24	1																	
$\mathcal{C}_{Hq}^{(1)}$	−0.41	0.34	−0.13	−0.31	0.20	−0.35	1																
$\mathcal{C}_{Hq}^{(3)}$	−0.24	0.13	0.02	−0.13	0.54	−0.13	−0.06	1															
$\mathcal{C}_{Hd}$	−0.01	0.02	−0.05	−0.02	−0.08	−0.02	0.37	0.09	1														
$\mathcal{C}_{Hu}$	−0.31	0.25	−0.15	−0.22	0.16	−0.25	0.59	−0.29	0.26	1													
$\mathcal{C}_{H}$	−0.10	0.09	−0.02	−0.09	0.01	−0.10	0.08	−0.01	0.03	0.12	1												
$\mathcal{C}_{H\Box}$	−0.60	0.58	−0.03	−0.56	0	−0.58	0.43	−0.02	0.12	0.55	0.23	1											
$\mathcal{C}_{HG}$	0.07	−0.05	0.02	0.04	−0.13	0.05	−0.06	−0.13	−0.03	−0.10	−0.28	−0.12	1										
$\mathcal{C}_{HW}$	0.88	−0.85	−0.02	0.83	0.02	0.85	−0.38	−0.24	−0.03	−0.33	−0.11	−0.62	0.07	1									
$\mathcal{C}_{HB}$	0.87	−0.86	−0.03	0.85	0.14	0.86	−0.35	−0.13	0	−0.26	−0.09	−0.54	0.07	0.53	1								
$\mathcal{C}_{W}$	0.15	−0.15	0.02	0.14	0.07	0.15	−0.02	−0.03	0.01	0	−0.01	−0.07	0	0.12	0.13	1							
$\mathcal{C}_{G}$	−0.05	0.06	0	−0.06	−0.04	−0.06	0.03	−0.03	0	0.03	0.01	0.02	−0.11	−0.03	−0.07	−0.01	1						
$\mathcal{C}_{\mu H}$	0	0	−0.01	0	0	0	0.01	−0.02	0.01	0.02	−0.01	0.02	0	0	0	0	0.04	1					
$\mathcal{C}_{\tau H}$	0	0	−0.01	0	−0.01	0	0.03	−0.05	0.01	0.05	−0.04	0.01	−0.16	0.01	0.01	0	0.05	0.07	1				
$\mathcal{C}_{bH}$	0.04	−0.11	−0.05	0.11	0.37	0.11	0.01	0.35	0.03	0.09	0.01	0.05	−0.40	0.07	0	0.02	−0.01	0.05	0.28	1			
$\mathcal{C}_{cH}$	0.51	−0.48	0.04	0.45	−0.08	0.48	−0.37	−0.06	−0.12	−0.51	−0.22	−0.95	0.15	0.52	0.48	0.06	0	0	0.08	−0.15	1		
$\mathcal{C}_{tH}$	−0.21	0.22	0	−0.21	−0.07	−0.22	0.15	−0.08	0.03	0.15	−0.19	0.21	0.37	−0.24	−0.14	−0.03	−0.39	−0.02	0.09	−0.01	−0.08	1	
$\mathcal{C}_{tG}$	−0.04	0.02	−0.01	−0.02	0.11	−0.02	0.04	0.10	0.02	0.08	0.16	0.09	−0.78	−0.06	−0.03	0	−0.17	−0.05	0.05	0.27	−0.12	0.14	1

APPENDIX D: DI-HIGGS DATA

TABLE XXVI. Considered signal strength measurements for di-Higgs production [23–28].

channel	ATLAS	CMS
$b\bar{b}b\bar{b}$	-12.7 ± 12.8	-3.9 ± 3.8
$b\bar{b}\gamma\gamma$	$-6.3^{+9.9}_{-7.5}$	2.5 ± 2.6
$b\bar{b}\tau\tau$	-4.1 ± 8.4	-5 ± 15

APPENDIX E: RELEVANT DIMENSION-SIX SMEFT OPERATORS

TABLE XXVII. These dimension-six effective operators (Warsaw basis) contribute to the observables. Here the σ's are Pauli matrices and the λ's are the Gell-Mann matrices.

Q_H	$(H^\dagger H)^3$	Q_{HG}	$(H^\dagger H)G_{\mu\nu}{}^a G^{a,\mu\nu}$	Q_{He}	$(H^\dagger i\overleftrightarrow{\mathcal{D}}_\mu H)(\bar{e}_R\gamma^\mu e_R)$
$Q_{H\Box}$	$(H^\dagger H)\Box(H^\dagger H)$	$Q^{(1)}_{Hl}$	$(H^\dagger i\overleftrightarrow{\mathcal{D}}_\mu H)(\bar{l}_L\gamma^\mu l_L)$	Q_{Hu}	$(H^\dagger i\overleftrightarrow{\mathcal{D}}_\mu H)(\bar{u}_R\gamma^\mu u_R)$
Q_{HD}	$(H^\dagger\mathcal{D}_\mu H)^*(H^\dagger\mathcal{D}^\mu H)$	$Q^{(3)}_{Hl}$	$(H^\dagger i\sigma^I\overleftrightarrow{\mathcal{D}}_\mu H)(\bar{l}_L\sigma^I\gamma^\mu l_L)$	Q_{Hd}	$(H^\dagger i\overleftrightarrow{\mathcal{D}}_\mu H)(\bar{d}_R\gamma^\mu d_R)$
Q_{HB}	$(H^\dagger H)B_{\mu\nu}B^{\mu\nu}$	$Q^{(1)}_{Hq}$	$(H^\dagger i\overleftrightarrow{\mathcal{D}}_\mu H)(\bar{q}_L\gamma^\mu q_L)$	$Q_{\tau H}$	$(H^\dagger H)(\bar{l}_L\,\tau_R\,H)+\text{H.c.}$
Q_{HW}	$(H^\dagger H)W_{\mu\nu}{}^I W^{I,\mu\nu}$	$Q^{(3)}_{Hq}$	$(H^\dagger i\sigma^I\overleftrightarrow{\mathcal{D}}_\mu H)(\bar{q}_L\sigma^I\gamma^\mu q_L)$	Q_{tH}	$(H^\dagger H)(\bar{q}_L\,t_R\,\tilde{H})+\text{H.c.}$
Q_{HWB}	$(H^\dagger\sigma^I H)W_{\mu\nu}{}^I B^{\mu\nu}$	Q_{ll}	$(\bar{l}_L\gamma_\mu l_L)(\bar{l}_L\gamma^\mu l_L)$	Q_{bH}	$(H^\dagger H)(\bar{q}_L\,b_R\,H)+\text{H.c.}$
Q_W	$\epsilon^{IJK}W_\rho{}^{I,\mu}W_\mu{}^{J,\nu}W_\nu{}^{K,\rho}$	Q_{tG}	$(\bar{q}_L\sigma^{\mu\nu}\frac{\lambda^a}{2}t_R)\tilde{H}G_{\mu\nu}{}^a$	$Q_{\mu H}$	$(H^\dagger H)(\bar{l}_L\,\mu_R\,H)+\text{H.c.}$
Q_G	$f^{abc}G_\rho{}^{a,\mu}G_\mu{}^{b,\nu}G_\nu{}^{c,\rho}$			Q_{cH}	$(H^\dagger H)(\bar{q}_L\,c_R\,\tilde{H})+\text{H.c.}$

[1] S. Schael *et al.* (ALEPH, DELPHI, L3, OPAL, SLD, LEP Electroweak Working Group, SLD Electroweak Group, SLD Heavy Flavour Group Collaborations), Precision electroweak measurements on the Z resonance, Phys. Rep. **427**, 257 (2006).

[2] L. Berthier, M. Bjørn, and M. Trott, Incorporating doubly resonant $W^\pm$ data in a global fit of SMEFT parameters to lift flat directions, J. High Energy Phys. 09 (2016) 157.

[3] G. Aad *et al.* (ATLAS, CMS Collaborations), Measurements of the Higgs boson production and decay rates and constraints on its couplings from a combined ATLAS and CMS analysis of the LHC pp collision data at $\sqrt{s} = 7$ and 8 TeV, J. High Energy Phys. 08 (2016) 045.

[4] G. Aad *et al.* (ATLAS Collaboration), Measurements of the Higgs boson production and decay rates and coupling strengths using pp collision data at $\sqrt{s} = 7$ and 8 TeV in the ATLAS experiment, Eur. Phys. J. C **76**, 6 (2016).

[5] G. Aad *et al.* (ATLAS Collaboration), A search for the $Z\gamma$ decay mode of the Higgs boson in pp collisions at $\sqrt{s} = 13$ TeV with the ATLAS detector, Phys. Lett. B **809**, 135754 (2020).

[6] G. Aad *et al.* (ATLAS Collaboration), A search for the dimuon decay of the Standard Model Higgs boson with the ATLAS detector, Phys. Lett. B **812**, 135980 (2021).

[7] ATLAS Collaboration, Measurements of Higgs boson production cross-sections in the $H \to \tau^+\tau^-$ decay channel in pp collisions at $\sqrt{s} = 13$ TeV with the ATLAS detector, Technical Report, CERN, Geneva, 2021. All figures including auxiliary figures are available at https://atlas.web.cern.ch/Atlas/GROUPS/PHYSICS/CONFNOTES/ATLAS-CONF-2021-044.

[8] G. Aad *et al.* (ATLAS Collaboration), Measurements of Higgs bosons decaying to bottom quarks from vector boson fusion production with the ATLAS experiment at $\sqrt{s} = 13$ TeV, Eur. Phys. J. C **81**, 537 (2021).

[9] ATLAS Collaboration, Measurement of the Higgs boson decaying to b-quarks produced in association with a top-quark pair in pp collisions at $\sqrt{s} = 13$ TeV with the

ATLAS detector, Report No. ATLAS-CONF-2020-058, 2020.
[10] ATLAS Collaboration, Interpretations of the combined measurement of Higgs boson production and decay, Report No. ATLAS-CONF-2020-053, 2020.
[11] ATLAS Collaboration, Measurements of gluon fusion and vector-boson-fusion production of the Higgs boson in $H \to WW^* \to e\nu\mu\nu$ decays using pp collisions at $\sqrt{s} =$ 13 TeV with the ATLAS detector, Report No. ATLAS-CONF-2021-014, 2021.
[12] CMS Collaboration, Combined Higgs boson production and decay measurements with up to 137 fb-1 of proton-proton collision data at sqrts = 13 TeV, Report No. CMS-PAS-HIG-19-005, 2020.
[13] A. M. Sirunyan *et al.* (CMS Collaboration), Measurement of the inclusive and differential Higgs boson production cross sections in the leptonic WW decay mode at $\sqrt{s} = 13$ TeV, J. High Energy Phys. 03 (2021) 003.
[14] A. M. Sirunyan *et al.* (CMS Collaboration), Evidence for Higgs boson decay to a pair of muons, J. High Energy Phys. 01 (2021) 148.
[15] A. M. Sirunyan *et al.* (CMS Collaboration), Measurement of the Higgs boson production rate in association with top quarks in final states with electrons, muons, and hadronically decaying tau leptons at $\sqrt{s} = 13$ TeV, Eur. Phys. J. C **81**, 378 (2021).
[16] CMS Collaboration, Measurement of Higgs boson production in association with a W or Z boson in the H → WW decay channel, Report No. CMS-PAS-HIG-19-017, 2021.
[17] CMS Collaboration, Measurement of Higgs boson production in the decay channel with a pair of τ leptons, Report No. CMS-PAS-HIG-19-010, 2020.
[18] A. M. Sirunyan *et al.* (CMS Collaboration), Measurements of Higgs boson production cross sections and couplings in the diphoton decay channel at $\sqrt{s} = 13$ TeV, J. High Energy Phys. 07 (2021) 027.
[19] A. M. Sirunyan *et al.* (CMS Collaboration), Measurements of production cross sections of the Higgs boson in the four-lepton final state in proton–proton collisions at $\sqrt{s} = 13$ TeV, Eur. Phys. J. C **81**, 488 (2021).
[20] M. Aaboud *et al.* (ATLAS Collaboration), Measurement of $W^{\pm}Z$ production cross sections and gauge boson polarisation in pp collisions at $\sqrt{s} = 13$ TeV with the ATLAS detector, Eur. Phys. J. C **79**, 535 (2019).
[21] G. Aad *et al.* (ATLAS Collaboration), Differential cross-section measurements for the electroweak production of dijets in association with a Z boson in proton–proton collisions at ATLAS, Eur. Phys. J. C **81**, 163 (2021).
[22] M. Aaboud *et al.* (ATLAS Collaboration), Measurement of fiducial and differential W^+W^- production cross-sections at $\sqrt{s} = 13$ TeV with the ATLAS detector, Eur. Phys. J. C **79**, 884 (2019).
[23] M. Aaboud *et al.* (ATLAS Collaboration), Search for Higgs boson pair production in the $\gamma\gamma b\bar{b}$ final state with 13 TeV pp collision data collected by the ATLAS experiment, J. High Energy Phys. 11 (2018) 040.
[24] M. Aaboud *et al.* (ATLAS Collaboration), Search for pair production of Higgs bosons in the $b\bar{b}b\bar{b}$ final state using proton-proton collisions at $\sqrt{s} = 13$ TeV with the ATLAS detector, J. High Energy Phys. 01 (2019) 030.
[25] M. Aaboud *et al.* (ATLAS Collaboration), Search for resonant and non-resonant Higgs boson pair production in the $b\bar{b}\tau^+\tau^-$ decay channel in pp collisions at $\sqrt{s} =$ 13 TeV with the ATLAS detector, Phys. Rev. Lett. **121**, 191801 (2018); **122**, 089901(E) (2019).
[26] A. M. Sirunyan *et al.* (CMS Collaboration), Search for nonresonant Higgs boson pair production in final states with two bottom quarks and two photons in proton-proton collisions at $\sqrt{s} = 13$ TeV, J. High Energy Phys. 03 (2021) 257.
[27] CMS Collaboration, Search for Higgs boson pair production in the four b quark final state, Report No. CMS-PAS-HIG-20-005, 2021.
[28] A. M. Sirunyan *et al.* (CMS Collaboration), Search for Higgs boson pair production in events with two bottom quarks and two tau leptons in proton–proton collisions at $\sqrt{s} = 13$ TeV, Phys. Lett. B **778**, 101 (2018).
[29] W. Buchmuller and D. Wyler, Effective Lagrangian analysis of new interactions and flavor conservation, Nucl. Phys. **B268**, 621 (1986).
[30] G. Giudice, C. Grojean, A. Pomarol, and R. Rattazzi, The strongly-interacting light Higgs, J. High Energy Phys. 06 (2007) 045.
[31] B. Grzadkowski, M. Iskrzynski, M. Misiak, and J. Rosiek, Dimension-six terms in the standard model Lagrangian, J. High Energy Phys. 10 (2010) 085.
[32] R. S. Gupta, Probing quartic neutral gauge boson couplings using diffractive photon fusion at the LHC, Phys. Rev. D **85**, 014006 (2012).
[33] R. S. Gupta, H. Rzehak, and J. D. Wells, How well do we need to measure Higgs boson couplings?, Phys. Rev. D **86**, 095001 (2012).
[34] S. Banerjee, S. Mukhopadhyay, and B. Mukhopadhyaya, New Higgs interactions and recent data from the LHC and the Tevatron, J. High Energy Phys. 10 (2012) 062.
[35] R. S. Gupta, M. Montull, and F. Riva, SUSY faces its Higgs couplings, J. High Energy Phys. 04 (2013) 132.
[36] S. Banerjee, S. Mukhopadhyay, and B. Mukhopadhyaya, Higher dimensional operators and the LHC Higgs data: The role of modified kinematics, Phys. Rev. D **89**, 053010 (2014).
[37] R. S. Gupta, H. Rzehak, and J. D. Wells, How well do we need to measure the Higgs boson mass and self-coupling?, Phys. Rev. D **88** (2013) 055024,
[38] J. Elias-Miró, C. Grojean, R. S. Gupta, and D. Marzocca, Scaling and tuning of EW and Higgs observables, J. High Energy Phys. 05 (2014) 019.
[39] R. Contino, M. Ghezzi, C. Grojean, M. Muhlleitner, and M. Spira, Effective Lagrangian for a light Higgs-like scalar, J. High Energy Phys. 07 (2013) 035.
[40] A. Falkowski and F. Riva, Model-independent precision constraints on dimension-6 operators, J. High Energy Phys. 02 (2015) 039.
[41] C. Englert and M. Spannowsky, Effective theories and measurements at colliders, Phys. Lett. B **740**, 8 (2015).
[42] R. S. Gupta, A. Pomarol, and F. Riva, BSM primary effects, Phys. Rev. D **91**, 035001 (2015).

[43] G. Amar, S. Banerjee, S. von Buddenbrock, A. S. Cornell, T. Mandal, B. Mellado, and B. Mukhopadhyaya, Exploration of the tensor structure of the Higgs boson coupling to weak bosons in e^+ e collisions, J. High Energy Phys. 02 (2015) 128.

[44] M. Buschmann, D. Goncalves, S. Kuttimalai, M. Schonherr, F. Krauss, and T. Plehn, Mass effects in the Higgs-gluon coupling: Boosted vs off-shell production, J. High Energy Phys. 02 (**2015**) 038.

[45] N. Craig, M. Farina, M. McCullough, and M. Perelstein, Precision Higgsstrahlung as a probe of new physics, J. High Energy Phys. 03 (**2015**) 146.

[46] J. Ellis, V. Sanz, and T. You, Complete Higgs sector constraints on dimension-6 operators, J. High Energy Phys. 07 (2014) 036.

[47] J. Ellis, V. Sanz, and T. You, The effective standard model after LHC run I, J. High Energy Phys. 03 (2015) 157.

[48] S. Banerjee, T. Mandal, B. Mellado, and B. Mukhopadhyaya, Cornering dimension-6HVV interactions at high luminosity LHC: The role of event ratios, J. High Energy Phys. 09 (2015) 057.

[49] C. Englert, R. Kogler, H. Schulz, and M. Spannowsky, Higgs coupling measurements at the LHC, Eur. Phys. J. C **76**, 393 (2016).

[50] D. Ghosh, R. S. Gupta, and G. Perez, Is the Higgs mechanism of fermion mass generation a fact? A Yukawa-less first-two-generation model, Phys. Lett. B **755**, 504 (2016).

[51] C. Degrande, B. Fuks, K. Mawatari, K. Mimasu, and V. Sanz, Electroweak Higgs boson production in the standard model effective field theory beyond leading order in QCD, Eur. Phys. J. C **77**, 262 (2017).

[52] J. Cohen, S. Bar-Shalom, and G. Eilam, Contact interactions in Higgs-vector boson associated production at the ILC, Phys. Rev. D **94**, 035030 (2016).

[53] S.-F. Ge, H.-J. He, and R.-Q. Xiao, Probing new physics scales from Higgs and electroweak observables at e^+ e Higgs factory, J. High Energy Phys. 10 (2016) 007.

[54] R. Contino, A. Falkowski, F. Goertz, C. Grojean, and F. Riva, On the validity of the effective field theory approach to SM precision tests, J. High Energy Phys. 07 (2016) 144.

[55] A. Biekötter, J. Brehmer, and T. Plehn, Extending the limits of Higgs effective theory, Phys. Rev. D **94**, 055032 (2016).

[56] J. de Blas, M. Ciuchini, E. Franco, S. Mishima, M. Pierini, L. Reina, and L. Silvestrini, Electroweak precision observables and Higgs-boson signal strengths in the Standard Model and beyond: Present and future, J. High Energy Phys. 12 (2016) 135.

[57] H. Denizli and A. Senol, Constraints on Higgs effective couplings in $H\nu\bar{\nu}$ production of CLIC at 380 GeV, Adv. High Energy Phys. **2018**, 1627051 (2018).

[58] T. Barklow, K. Fujii, S. Jung, R. Karl, J. List, T. Ogawa, M. E. Peskin, and J. Tian, Improved formalism for precision Higgs coupling fits, Phys. Rev. D **97**, 053003 (2018).

[59] I. Brivio and M. Trott, The Standard Model as an effective field theory, Phys. Rep. **793**, 1 (2019).

[60] T. Barklow, K. Fujii, S. Jung, M. E. Peskin, and J. Tian, Model-independent determination of the Triple Higgs coupling at e^+e^- colliders, Phys. Rev. D **97**, 053004 (2018).

[61] H. Khanpour and M. Mohammadi Najafabadi, Constraining Higgs boson effective couplings at electron-positron colliders, Phys. Rev. D **95**, 055026 (2017).

[62] C. Englert, R. Kogler, H. Schulz, and M. Spannowsky, Higgs characterisation in the presence of theoretical uncertainties and invisible decays, Eur. Phys. J. C **77**, 789 (2017).

[63] G. Panico, F. Riva, and A. Wulzer, Diboson interference resurrection, Phys. Lett. B **776**, 473 (2018).

[64] R. Franceschini, G. Panico, A. Pomarol, F. Riva, and A. Wulzer, Electroweak precision tests in high-energy Diboson processes, J. High Energy Phys. 02 (2018) 111.

[65] S. Banerjee, C. Englert, R. S. Gupta, and M. Spannowsky, Probing electroweak precision physics via boosted Higgs-strahlung at the LHC, Phys. Rev. D **98**, 095012 (2018).

[66] C. Grojean, M. Montull, and M. Riembau, Diboson at the LHC vs LEP, J. High Energy Phys. 03 (2019) 020.

[67] A. Biekoetter, T. Corbett, and T. Plehn, The Gauge-Higgs legacy of the LHC run II, SciPost Phys. **6**, 064 (2019).

[68] D. Goncalves and J. Nakamura, Boosting the $H \to$ invisibles searches with Z boson polarization, Phys. Rev. D **99**, 055021 (2019).

[69] R. Gomez-Ambrosio, Studies of dimension-six EFT effects in vector boson scattering, Eur. Phys. J. C **79**, 389 (2019).

[70] F. F. Freitas, C. K. Khosa, and V. Sanz, Exploring SMEFT in VH with machine learning, Phys. Rev. D **100**, 035040 (2019).

[71] S. Banerjee, R. S. Gupta, J. Y. Reiness, and M. Spannowsky, Resolving the tensor structure of the Higgs coupling to Z-bosons via Higgs-strahlung, Phys. Rev. D **100**, 115004 (2019).

[72] S. Banerjee, R. S. Gupta, J. Y. Reiness, S. Seth, and M. Spannowsky, Towards the ultimate differential SMEFT analysis, J. High Energy Phys. 09 (2020) 170.

[73] A. Biekötter, R. Gomez-Ambrosio, P. Gregg, F. Krauss, and M. Schönherr, Constraining SMEFT operators with associated $h\gamma$ production in weak boson fusion, Phys. Lett. B **814**, 136079 (2021).

[74] J. Y. Araz, S. Banerjee, R. S. Gupta, and M. Spannowsky, Precision SMEFT bounds from the VBF Higgs at high transverse momentum, J. High Energy Phys. 04 (2021) 125.

[75] J. Ellis, M. Madigan, K. Mimasu, V. Sanz, and T. You, Top, Higgs, Diboson and electroweak fit to the standard model effective field theory, J. High Energy Phys. 04 (2021) 279.

[76] S. Banerjee, R. S. Gupta, O. Ochoa-Valeriano, M. Spannowsky, and E. Venturini, A fully differential SMEFT analysis of the golden channel using the method of moments, J. High Energy Phys. 06 (2021) 031.

[77] E. d. S. Almeida, A. Alves, O. J. P. Éboli, and M. C. Gonzalez-Garcia, Electroweak legacy of the LHC Run II, Phys. Rev. D **105**, 013006 (2022).

[78] S. Chatterjee, N. Frohner, L. Lechner, R. Schöfbeck, and D. Schwarz, Tree boosting for learning EFT parameters, Comput. Phys. Commun. **277**, 108385 (2022).

[79] I. Brivio and M. Trott, The standard model as an effective field theory, Phys. Rep. **793**, 1 (2019).

[80] J. Elias-Miro, J. R. Espinosa, E. Masso, and A. Pomarol, Higgs windows to new physics through d = 6 operators: Constraints and one-loop anomalous dimensions, J. High Energy Phys. 11 (2013) 066.
[81] Z. Han and W. Skiba, Effective theory analysis of precision electroweak data, Phys. Rev. D **71**, 075009 (2005).
[82] T. Corbett, O. J. P. Eboli, J. Gonzalez-Fraile, and M. C. Gonzalez-Garcia, Robust determination of the Higgs couplings: Power to the data, Phys. Rev. D **87**, 015022 (2013).
[83] B. Dumont, S. Fichet, and G. von Gersdorff, A Bayesian view of the Higgs sector with higher dimensional operators, J. High Energy Phys. 07 (2013) 065.
[84] T. Corbett, O. J. P. Éboli, J. Gonzalez-Fraile, and M. C. Gonzalez-Garcia, Determining Triple Gauge Boson Couplings from Higgs Data, Phys. Rev. Lett. **111**, 011801 (2013).
[85] W.-F. Chang, W.-P. Pan, and F. Xu, Effective gauge-Higgs operators analysis of new physics associated with the Higgs boson, Phys. Rev. D **88**, 033004 (2013).
[86] E. Boos, V. Bunichev, M. Dubinin, and Y. Kurihara, Higgs boson signal at complete tree level in the SM extension by dimension-six operators, Phys. Rev. D **89**, 035001 (2014).
[87] J. Baglio, S. Dawson, and I. M. Lewis, NLO effects in EFT fits to W^+W^- production at the LHC, Phys. Rev. D **99**, 035029 (2019).
[88] J. Baglio, S. Dawson, and S. Homiller, QCD corrections in Standard Model EFT fits to WZ and WW production, Phys. Rev. D **100**, 113010 (2019).
[89] A. Azatov, D. Barducci, and E. Venturini, Precision diboson measurements at hadron colliders, J. High Energy Phys. 04 (2019) 075.
[90] A. Buckley, C. Englert, J. Ferrando, D. J. Miller, L. Moore, M. Russell, and C. D. White, Constraining top quark effective theory in the LHC Run II era, J. High Energy Phys. 04 (2016) 015.
[91] I. Brivio, S. Bruggisser, F. Maltoni, R. Moutafis, T. Plehn, E. Vryonidou, S. Westhoff, and C. Zhang, O new physics, where art thou? A global search in the top sector, J. High Energy Phys. 02 (2020) 131.
[92] S. Bißmann, J. Erdmann, C. Grunwald, G. Hiller, and K. Kröninger, Constraining top-quark couplings combining top-quark and **B** decay observables, Eur. Phys. J. C **80**, 136 (2020).
[93] N. P. Hartland, F. Maltoni, E. R. Nocera, J. Rojo, E. Slade, E. Vryonidou, and C. Zhang, A Monte Carlo global analysis of the Standard Model Effective Field Theory: The top quark sector, J. High Energy Phys. 04 (2019) 100.
[94] G. Durieux, A. Irles, V. Miralles, A. Peñuelas, R. Pöschl, M. Perelló, and M. Vos, The electro-weak couplings of the top and bottom quarks—Global fit and future prospects, J. High Energy Phys. 12 (**2019**) 098; 01 (2021) 195(E).
[95] S. van Beek, E. R. Nocera, J. Rojo, and E. Slade, Constraining the SMEFT with Bayesian reweighting, SciPost Phys. **7**, 070 (2019).
[96] CMS Collaboration, Using associated top quark production to probe for new physics within the framework of effective field theory.
[97] A. Butter, O. J. P. Éboli, J. Gonzalez-Fraile, M. Gonzalez-Garcia, T. Plehn, and M. Rauch, The Gauge-Higgs legacy of the LHC run I, J. High Energy Phys. 07 (2016) 152.
[98] A. Biektter, T. Corbett, and T. Plehn, The Gauge-Higgs legacy of the LHC run II, SciPost Phys. **6**, 064 (2019).
[99] J. Ellis, C. W. Murphy, V. Sanz, and T. You, Updated global SMEFT fit to Higgs, Diboson and electroweak data, J. High Energy Phys. 06 (2018) 146.
[100] Anisha, S. Das Bakshi, J. Chakrabortty, and S. K. Patra, A step toward model comparison: Connecting electroweak-scale observables to BSM through EFT and Bayesian statistics, Phys. Rev. D **103**, 076007 (2021).
[101] S. Dawson, S. Homiller, and S. D. Lane, Putting standard model EFT fits to work, Phys. Rev. D **102**, 055012 (2020).
[102] J. J. Ethier, G. Magni, F. Maltoni, L. Mantani, E. R. Nocera, J. Rojo, E. Slade, E. Vryonidou, and C. Zhang, Combined SMEFT interpretation of Higgs, diboson, and top quark data from the LHC, J. High Energy Phys. 11 (2021) 089.
[103] B. Henning, X. Lu, and H. Murayama, How to use the Standard Model effective field theory, J. High Energy Phys. 01 (2016) 023.
[104] A. Drozd, J. Ellis, J. Quevillon, and T. You, The universal one-loop effective action, J. High Energy Phys. 03 (2016) 180.
[105] B. Henning, X. Lu, and H. Murayama, One-loop matching and running with covariant derivative expansion, J. High Energy Phys. 01 (2018) 123.
[106] S. A. R. Ellis, J. Quevillon, T. You, and Z. Zhang, Mixed heavylight matching in the universal one-loop effactive action, Phys. Lett. B **762**, 166 (2016).
[107] J. Fuentes-Martin, J. Portoles, and P. Ruiz-Femenia, Integrating out heavy particles with functional methods: A simplified framework, J. High Energy Phys. 09 (2016) 156.
[108] Z. Zhang, Covariant diagrams for one-loop matching, J. High Energy Phys. 05 (**2017**) 152.
[109] S. A. R. Ellis, J. Quevillon, T. You, and Z. Zhang, Extending the universal one-loop effective action: Heavy-light coefficients, J. High Energy Phys. 08 (2017) 054.
[110] J. de Blas, J. C. Criado, M. Prez-Victoria, and J. Santiago, Effective description of general extensions of the standard model: The complete tree-level dictionary, J. High Energy Phys. 03 (2018) 109 .
[111] S. Das Bakshi, J. Chakrabortty, and S. K. Patra, CoDEx: Wilson coefficient calculator connecting SMEFT to UV theory, Eur. Phys. J. C **79**, 21 (2019).
[112] M. Krmer, B. Summ, and A. Voigt, Completing the scalar and fermionic universal one-loop effective action, J. High Energy Phys. 01 (2020) 079.
[113] S. Das Bakshi, J. Chakrabortty, C. Englert, M. Spannowsky, and P. Stylianou, ATLAS violating CP effectively, Phys. Rev. D **103**, 055008 (2021).
[114] S. Das Bakshi, J. Chakrabortty, and M. Spannowsky, Classifying standard model extensions effectively with precision observables, Phys. Rev. D **103**, 056019 (2021).
[115] U. Haisch, M. Ruhdorfer, E. Salvioni, E. Venturini, and A. Weiler, Singlet night in Feynman-ville: one-loop matching of a real scalar, J. High Energy Phys. 04 (2020) 164.
[116] S. Dawson, P. P. Giardino, and S. Homiller, Uncovering the high scale Higgs singlet model, Phys. Rev. D **103**, 075016 (2021).

[117] S. Dittmaier, S. Schuhmacher, and M. Stahlhofen, Integrating out heavy fields in the path integral using the background-field method: General formalism, Eur. Phys. J. C **81**, 826 (2021).

[118] I. Brivio, S. Bruggisser, E. Geoffray, W. Kilian, M. Krämer, M. Luchmann, T. Plehn, and B. Summ, From models to SMEFT and back?, SciPost Phys. **12**, 036 (2022).

[119] A. Dedes and K. Mantzaropoulos, Universal scalar leptoquark action for matching, J. High Energy Phys. 11 (2021) 166.

[120] S. Das Bakshi, J. Chakrabortty, S. Prakash, S. U. Rahaman, and M. Spannowsky, EFT diagrammatica: UV roots of the *CP*-conserving SMEFT, J. High Energy Phys. 06 (2021) 033.

[121] S. Patra, sunandopatra/optex-1.0.0: Wo documentation, 10.5281/zenodo.3404311 (2019).

[122] U. K. Dey and S. Mohanty, Constraints on leptoquark models from IceCube data, J. High Energy Phys. 04 (2016) 187.

[123] A. Pilaftsis and C. E. Wagner, Higgs bosons in the minimal supersymmetric standard model with explicit *CP* violation, Nucl. Phys. **B553**, 3 (1999).

[124] A. Arhrib, R. Benbrik, M. Chabab, G. Moultaka, M. Peyranere, L. Rahili, and J. Ramadan, The Higgs potential in the Type II Seesaw Model, Phys. Rev. D **84**, 095005 (2011).

[125] K. S. Babu, S. Nandi, and Z. Tavartkiladze, New mechanism for neutrino mass generation and triply charged Higgs bosons at the LHC, Phys. Rev. D **80**, 071702 (2009).

[126] G. Bambhaniya, J. Chakrabortty, S. Goswami, and P. Konar, Generation of neutrino mass from new physics at TeV scale and multilepton signatures at the LHC, Phys. Rev. D **88**, 075006 (2013).

[127] W. Buchmuller, R. Ruckl, and D. Wyler, Leptoquarks in lepton—Quark collisions, Phys. Lett. B **191**, 442 (1987); **448**, 320(E) (1999).

[128] J. M. Arnold, B. Fornal, and M. B. Wise, Phenomenology of scalar leptoquarks, Phys. Rev. D **88**, 035009 (2013).

[129] M. Bauer and M. Neubert, Minimal Leptoquark Explanation for the $R_{D^{(*)}}$, R_K, and $(g-2)_g$ Anomalies, Phys. Rev. Lett. **116**, 141802 (2016).

[130] P. Bandyopadhyay and R. Mandal, Vacuum stability in an extended standard model with a leptoquark, Phys. Rev. D **95**, 035007 (2017).

[131] S. Davidson and S. Descotes-Genon, Minimal flavour violation for leptoquarks, J. High Energy Phys. 11 (2010) 073.

[132] C.-R. Chen, W. Klemm, V. Rentala, and K. Wang, Color sextet scalars at the CERN Large Hadron Collider, Phys. Rev. D **79**, 054002 (2009).

[133] U. Banerjee, J. Chakrabortty, S. Prakash, and S. U. Rahaman, Characters and group invariant polynomials of (Super)fields: Road to "Lagrangian", Eur. Phys. J. C **80**, 938 (2020).

[134] G. D'Ambrosio, G. F. Giudice, G. Isidori, and A. Strumia, Minimal flavor violation: An effective field theory approach, Nucl. Phys. **B645**, 155 (2002).

[135] G. Perez, Y. Soreq, E. Stamou, and K. Tobioka, Constraining the charm Yukawa and Higgs-quark coupling universality, Phys. Rev. D **92**, 033016 (2015).

[136] A. Falkowski, S. Ganguly, P. Gras, J. M. No, K. Tobioka, N. Vignaroli, and T. You, Light quark Yukawas in triboson final states, J. High Energy Phys. 04 (2021) 023.

[137] A. Efrati, A. Falkowski, and Y. Soreq, Electroweak constraints on flavorful effective theories, J. High Energy Phys. 07 (2015) 018.

[138] I. Brivio, Y. Jiang, and M. Trott, The SMEFTsim package, theory and tools, J. High Energy Phys. 12 (2017) 070.

[139] J. Alwall, R. Frederix, S. Frixione, V. Hirschi, F. Maltoni, O. Mattelaer, H. S. Shao, T. Stelzer, P. Torrielli, and M. Zaro, The automated computation of tree-level and next-to-leading order differential cross sections, and their matching to parton shower simulations, J. High Energy Phys. 07 (2014) 079.

[140] NNPDF Collaboration, R. D. Ball, V. Bertone, S. Carrazza, L. Del Debbio, S. Forte, A. Guffanti, N. P. Hartland, and J. Rojo, Parton distributions with QED corrections, Nucl. Phys. **B877**, 290 (2013).

[141] C. Degrande, G. Durieux, F. Maltoni, K. Mimasu, E. Vryonidou, and C. Zhang, Automated one-loop computations in the standard model effective field theory, Phys. Rev. D **103**, 096024 (2021).

[142] G. Degrassi, P. P. Giardino, F. Maltoni, and D. Pagani, Probing the Higgs self coupling via single Higgs production at the LHC, J. High Energy Phys. 12 (2016) 080.

[143] G. Degrassi and M. Vitti, The effect of an anomalous Higgs trilinear self-coupling on the $h \to \gamma Z$ decay, Eur. Phys. J. C **80**, 307 (2020).

[144] G. Heinrich, S. P. Jones, M. Kerner, and L. Scyboz, A nonlinear EFT description of $gg \to HH$ at NLO interfaced to POWHEG, J. High Energy Phys. 10 (2020) 021.

[145] P. Nason, A new method for combining NLO QCD with shower Monte Carlo algorithms, J. High Energy Phys. 11 (2004) 040.

[146] S. Frixione, P. Nason, and C. Oleari, Matching NLO QCD computations with Parton Shower simulations: The POWHEG method, J. High Energy Phys. 11 (2007) 070.

[147] S. Alioli, P. Nason, C. Oleari, and E. Re, A general framework for implementing NLO calculations in shower Monte Carlo programs: The POWHEG BOX, J. High Energy Phys. 06 (2010) 043.

[148] A. Falkowski. https://cds.cern.ch/record/2001958/files/LHCHXSWG-INT-2015-001-2.pdf (2017).

[149] L. J. Dixon, Z. Kunszt, and A. Signer, Vector boson pair production in hadronic collisions at order α_s: Lepton correlations and anomalous couplings, Phys. Rev. D **60**, 114037 (1999).

[150] U. Baur, T. Han, and J. Ohnemus, WZ production at hadron colliders: Effects of nonstandard WWZ couplings and QCD corrections, Phys. Rev. D **51**, 3381 (1995).

[151] T. Sjstrand, S. Ask, J. R. Christiansen, R. Corke, N. Desai, P. Ilten, S. Mrenna, S. Prestel, C. O. Rasmussen, and P. Z. Skands, An Introduction to PYTHIA 8.2, Comput. Phys. Commun. **191** (2015) 159,

[152] M. Aaboud *et al.* (ATLAS Collaboration), Measurement of $W^{\pm}Z$ production cross sections and gauge boson polarisation in pp collisions at $\sqrt{s} = 13$ TeV with the ATLAS detector, Eur. Phys. J. C **79**, 535 (2019).

[153] A. Buckley, J. Butterworth, D. Grellscheid, H. Hoeth, L. Lonnblad, J. Monk, H. Schulz, and F. Siegert, Rivet user manual, Comput. Phys. Commun. **184**, 2803 (2013).
[154] L. Berthier and M. Trott, Towards consistent Electroweak Precision Data constraints in the SMEFT, J. High Energy Phys. 05 (2015) 024.
[155] S. Dawson and P. P. Giardino, Electroweak and QCD corrections to Z and W pole observables in the standard model EFT, Phys. Rev. D **101**, 013001 (2020).
[156] Particle Data GroupReview of Particle Physics, Prog. Theor. Exp. Phys. **2020**, 083C01 (2020).
[157] G. Degrassi, B. Di Micco, P. P. Giardino, and E. Rossi, Higgs boson self-coupling constraints from single Higgs, double Higgs and Electroweak measurements, Phys. Lett. B **817**, 136307 (2021).
[158] S. Schael *et al.* (ALEPH, DELPHI, L3, OPAL, LEP Electroweak Collaborations), Electroweak measurements in electron-positron collisions at W-boson-pair energies at LEP, Phys. Rep. **532**, 119 (2013).
[159] CDF, D0 Collaborations, T. E. W. Group, 2012 update of the combination of CDF and D0 results for the mass of the W boson, arXiv:1204.0042.
[160] M. Aaboud *et al.* (ATLAS Collaboration), Measurement of the W-boson mass in pp collisions at $\sqrt{s} = 7$ TeV with the ATLAS detector, Eur. Phys. J. C **78**, 110 (2018); **78**, 898 (E) (2018).
[161] P. Zyla *et al.* (Particle Data Group), Review of particle physics, Prog. Theor. Exp. Phys. **2020**, 083C01 (2020).
[162] T. A. Aaltonen *et al.* (CDF, D0 Collaboration), Tevatron Run II combination of the effective leptonic electroweak mixing angle, Phys. Rev. D **97**, 112007 (2018).
[163] E. Maguire, L. Heinrich, and G. Watt, HEPData: A repository for high energy physics data, J. Phys. Conf. Ser. **898**, 102006 (2017).
[164] P. Achard *et al.* (L3 Collaboration), Measurement of the cross section of W-boson pair production at LEP, Phys. Lett. B **600**, 22 (2004).
[165] G. Abbiendi *et al.* (OPAL Collaboration), Measurement of the $e^+e^- \to W^+W^-$ cross section and W decay branching fractions at LEP, Eur. Phys. J. C **52**, 767 (2007).
[166] A. Heister *et al.* (ALEPH Collaboration), Measurement of W-pair production in e^+e^- collisions at centre-of-mass energies from 183-GeV to 209-GeV, Eur. Phys. J. C **38**, 147 (2004).
[167] J. Haller, A. Hoecker, R. Kogler, K. Mnig, T. Peiffer, and J. Stelzer, Update of the global electroweak fit and constraints on two-Higgs-doublet models, Eur. Phys. J. C **78**, 675 (2018).
[168] G. Aad *et al.* (ATLAS Collaboration), Combined measurements of Higgs boson production and decay using up to 80 fb^{-1} of proton-proton collision data at $\sqrt{s} = 13$ TeV collected with the ATLAS experiment, Phys. Rev. D **101**, 012002 (2020).
[169] W. K. Hastings, Monte carlo sampling methods using markov chains and their applications, Biometrika **57**, 97 (1970).
[170] A. E. Raftery and S. M. Lewis, [practical Markov chain Monte Carlo]: Comment: One long run with diagnostics: Implementation strategies for markov Chain Monte Carlo, Stat. Sci. **7**, 493 (1992).
[171] F. del Aguila, Z. Kunszt, and J. Santiago, One-loop effective Lagrangians after matching, Eur. Phys. J. C **76**, 244 (2016).
[172] Anisha, S. D Bakshi, S. Banerjee, A. Biekötter, J. Chakrabortty, S. K. Patra, and M. Spannowsky, CoDEx implementation codes for 16 models and EFT constrained model parameter bounds, https://github.com/effExTeam/Precision-Observables-and-Higgs-Signals-Effective-passageto-select-BSM.
[173] U. Haisch, M. Ruhdorfer, E. Salvioni, E. Venturini, and A. Weiler, Singlet night in Feynman-ville: One-loop matching of a real scalar, J. High Energy Phys. 04 (2020) 164.
[174] M. Jiang, N. Craig, Y.-Y. Li, and D. Sutherland, Complete one-loop matching for a singlet scalar in the standard model EFT, J. High Energy Phys. 02 (2019) 031.
[175] T. Cohen, X. Lu, and Z. Zhang, Functional prescription for EFT matching, J. High Energy Phys. 02 (2021) 228.
[176] V. Gherardi, D. Marzocca, and E. Venturini, Low-energy phenomenology of scalar leptoquarks at one-loop accuracy, J. High Energy Phys. 01 (2021) 138.
[177] J. de Blas, J. Criado, M. Perez-Victoria, and J. Santiago, Effective description of general extensions of the Standard Model: The complete tree-level dictionary, J. High Energy Phys. 03 (2018) 109.
[178] N. G. Deshpande and E. Ma, Pattern of symmetry breaking with two Higgs doublets, Phys. Rev. D **18**, 2574 (1978).
[179] S. Nie and M. Sher, Vacuum stability bounds in the two-Higgs doublet model, Phys. Lett. B **449**, 89 (1999).
[180] V. Branchina, F. Contino, and P. Ferreira, Electroweak vacuum lifetime in two Higgs doublet models, J. High Energy Phys. 11 (2018) 107.
[181] J. F. Gunion and H. E. Haber, The CP conserving two Higgs doublet model: The approach to the decoupling limit, Phys. Rev. D **67** (2003) 075019,
[182] A. Falkowski, M. González-Alonso, and K. Mimouni, Compilation of low-energy constraints on 4-fermion operators in the SMEFT, J. High Energy Phys. 08 (2017) 123.
[183] W. Dekens, J. de Vries, M. Jung, and K. K. Vos, The phenomenology of electric dipole moments in models of scalar leptoquarks, J. High Energy Phys. 01 (2019) 069.
[184] E. E. Jenkins, A. V. Manohar, and M. Trott, Renormalization Group evolution of the standard model dimension six operators II: Yukawa dependence, J. High Energy Phys. 01 (2014) 035.
[185] E. E. Jenkins, A. V. Manohar, and M. Trott, Renormalization group evolution of the standard model dimension six operators I: Formalism and lambda dependence, J. High Energy Phys. 10 (2013) 087.
[186] R. Alonso, E. E. Jenkins, A. V. Manohar, and M. Trott, Renormalization group evolution of the standard model dimension six operators III: Gauge coupling dependence and phenomenology, J. High Energy Phys. 04 (2014) 159.
[187] See Supplemental Material at http://link.aps.org/supplemental/10.1103/PhysRevD.107.055028 for effective limits on single scalar extensions in the light of recent LHC data.
[188] M. Schmaltz and Y.-M. Zhong, The leptoquark Hunter's guide: Large coupling, J. High Energy Phys. 01 (2019) 132.

[189] J. Fuentes-Martin, M. König, J. Pagès, A. E. Thomsen, and F. Wilsch, SuperTracer: A calculator of functional supertraces for one-loop EFT matching, J. High Energy Phys. 04 (2021) 281.

[190] T. Cohen, X. Lu, and Z. Zhang, STrEAMlining EFT matching, SciPost Phys. **10**, 098 (2021).

[191] S. Dawson and C. W. Murphy, Standard model EFT and extended scalar sectors, Phys. Rev. D **96**, 015041 (2017).

[192] M. S. Bilenky and A. Santamaria, One loop effective Lagrangian for a standard model with a heavy charged scalar singlet, Nucl. Phys. **B420**, 47 (1994).

[193] M. S. Bilenky and A. Santamaria, Beyond the standard model with effective Lagrangians, in *28th International Symposium on Particle Theory* (1994), 8, arXiv:hep-ph/9503257.

[194] J. de Blas, M. Chala, M. Perez-Victoria, and J. Santiago, Observable effects of general new scalar particles, J. High Energy Phys. 04 (2015) 078.